UC San Diego
UC San Diego Electronic Theses and Dissertations

Title
Earthquake cycle study with geodetic tools

Permalink
https://escholarship.org/uc/item/6gg9r2r0

Author
Xu, Xiaohua

Publication Date
2017

Peer reviewed|Thesis/dissertation

UNIVERSITY OF CALIFORNIA, SAN DIEGO

Earthquake Cycle Study with Geodetic Tools

A dissertation submitted in partial satisfaction of the
requirements for the degree
Doctor of Philosophy

in

Earth Sciences

by

Xiaohua Xu

Committee in charge:

David T. Sandwell, Chair
Duncan C. Agnew
C. David Chadwell
Yuri Fialko
Tara C. Hutchinson
Peter M. Shearer

2017

The dissertation of Xiaohua Xu is approved, and it is acceptable in quality and form for publication on microfilm and electronically:

_____

_____

_____

_____

_____

Chair

University of California, San Diego

2017

DEDICATION

To my advisor David for his enlightenment on both my life and research.

To my parents Yunhong and Minglun for their love and support ever since I was born.

To my wife Rui for bring cheer and joy to my life.

EPIGRAPH

<div style="text-align: center">

子曰：“学而不思则罔，思而不学则殆。”

The Master said,

"If you study but don't reflect, you'll get confused.

If you reflect but don't study you'll get into trouble."

子曰：“由，诲女知之乎！知之为知之，不知为不知，是知也。”

The Master said,

"Yóu (name), shall I teach you about knowledge?

If you know, recognize that you know.

If you don't, realize that you don't.

That is knowledge."

子在川上曰：“逝者如斯夫,不舍昼夜。”

The Master stood on the banks of the river, said,

"How it flows on, never creasing, day and night! "

—The Analects of Confucius

</div>

TABLE OF CONTENTS

vii

LIST OF FIGURES

LIST OF TABLES

ACKNOWLEDGEMENTS

Five years of PhD life passed so quickly that I feel my arrival at San Diego was like yesterday. I could still remember my first impression here on the sunshine, the beach and the palm trees that welcomed me to Scripps. I think I am fortunate to have the opportunity to pursue a PhD degree in IGPP at Scripps, not only because of the scenic view right outside my office, but also the people I met here.

First and foremost, I want to thank my advisor David Sandwell, who accepted me to his group and introduced me to geodesy. I benefit so much from his enthusiasm and passion both in life and in research. During the past 5 years, I wrote 1,118 emails to David and received 985 emails from him even though our offices were just next to each other. His door was always open and he was always responsive to my questions. His cheering illustration and intriguing ideas enlightened me and always directed me to the correct path. I would also like to thank all me thesis committee members, who supported and encouraged me over the years. Professor Yuri Fialko helped me on better understanding InSAR and crustal deformation. Professor Duncan Agnew taught me signal processing and had a strong influence on me with his rigorous attitude toward research. Professor Peter Shearer taught me seismology and provided me with different views on my research. Dr. David Chadwell offered me a perspective from seafloor geodesy. Professor Tara Hutchinson helped understand the relation between my research and civil engineering. Besides, I actually want thank all the professors and research scientists in IGPP. I think all of you are setting excellent examples for students to know what a good professor or a good research scientist should look like. I think I am lucky to learn this at my early career.

I would like to thank David Jackson for patiently instructing me over the CSST program during summer 2012 at UCLA and binging me to SCEC where I found my

PhD advisor. I would like to thank my cohort group, Zhao Chen, Yuxiang Zhang, Katia Tymofyeyeva, Bill Savran, Dallas Sherman and James Holmes, for the friendship between us and the happy times we spent at Keller. My special thank goes to Katia and Dallas for talking to me and constantly correcting my terrible English when I first got here. I want to thank all my collaborators, Xiaopeng Tong, Diego Melgar, Christopher Milliner, Eric Lindsey, Dan Bassett, Katia Tymofyeyeva, etc, for their help on my research and writing. I would also like to thank Professor Paul Wessel for his help on GMT, Xiaopeng Tong for his help on running inversion with geodetic data and Kang Wang for all the discussions on InSAR. I also want to thank everyone in the Sandwell group, John Desanto, Soli Garcia, Xiaopeng Tong, Matt Wei, Karen Luttrell, Bridget Smith-Konter, JJ Becker, etc., for forming such a bound and passing on the fun working environment. Also I would like to thank Susan Sandwell for inviting me to dinner every Thanksgiving and making me feel at home. The food was delicious.

I would also like to thank Zhao Chen, Wei Wang, Kang Wang, Chu Yu, Yuxiang Zhang, Yongfei Wang, Shiying Nie, Wenyuan Fan, Qian Yao, Zhongwen Zhan, Qiong Zhang, Junle Jiang and Shawn Wei. My life became much more interesting with you guys. I want to thank my parents for their support and love every since I was born. Finally, I want to sincerely thank my best friend, wife and true love, Rui Hua. Thank you for showing up in my life, kind of late though, and bringing beauty, joy and wonderful memories to me. I love you until the entropy of the whole universe is maximized.

Chapter 2, in full, is a reprint of the material as it appears in Geophysical Journal International: Xu, X., Tong, X., Sandwell, D.T., Milliner, C.W., Dolan, J.F., Hollingsworth, J., Leprince, S. and Ayoub, F., 2016, "Refining the shallow slip deficit", *Geophysical Journal International*, 204(3), pp.1867-1886. The dissertation author is the

primary investigator and author of this paper.

Chapter 3, in full, is a reprint of the material as it appears in Geophysical Journal International: Xu, X., Sandwell, D.T. and Bassett, D., 2017, "A Spectral Expansion Approach for Geodetic Slip Inversion: Implications for the Down-dip Rupture Limits of Oceanic and Continental Megathrust Earthquakes", *Geophysical Journal International*, p.ggx408. The dissertation author is the primary investigator and author of this paper.

Chapter 4, in full, is a reprint of the material as it appears in Transactions on Geoscience and Remote Sensing: Xu, X., Sandwell, D.T., Tymofyeyeva, E., González-Ortega, A. and Tong, X., 2017, "Tectonic and Anthropogenic Deformation at the Cerro Prieto Geothermal Step-Over Revealed by Sentinel-1A InSAR", *IEEE Transactions on Geoscience and Remote Sensing.* The dissertation author was the primary investigator and author of the paper.

Chapter 5, in full, is currently being prepared for publication as Xu, X. Sandwell, D.T., "Line-of-Sight Deformation along the San Andreas Fault revealed by Sentinel-1 InSAR". The dissertation author was the primary investigator and author of the paper.

VITA

Nov 26, 1989	Born, Dongying, Shandong, China
2008-2012	Bachelor of Science in Geophysics, University of Science and Technology of China, Hefei, China
2012	Cross-disciplinary Scholars in Science and Technology program, University of California, Los Angeles, U.S.A.
2012-2017	Graduate Student Researcher, Scripps Institution of Oceanography, University of California, San Diego, U.S.A.
2017	Doctor of Philosophy in Earth Sciences, Scripps Institution of Oceanography, University of California, San Diego, U.S.A.

PUBLICATIONS

Xu, X. and Sandwell, D.T., "Line-of-Sight Deformation along the San Andreas Fault revealed by Sentinel-1 InSAR", *in prep*

Wang, K., **Xu, X.** and Fialko, Y., "Improving burst alignment in TOPS Interferometry with Bivariate Enhanced Spectral Diversity (BESD)", *IEEE Geoscience and Remote Sensing Letters*, 2017.

Xu, X., Sandwell, D.T. and Bassett, D., "A Spectral Expansion Approach for Geodetic Slip Inversion: Implications for the Down-dip Rupture Limits of Oceanic and Continental Megathrust Earthquakes", *Geophysical Journal International*, p.ggx408, 2017.

Xu, X., Sandwell, D.T., Tymofyeyeva, E., González-Ortega, A. and Tong, X., "Tectonic and Anthropogenic Deformation at the Cerro Prieto Geothermal Step-Over Revealed by Sentinel-1A InSAR", *IEEE Transactions on Geoscience and Remote Sensing*, 2017.

Melgar, D., Riquelme, S., **Xu, X.**, Baez, J.C., Geng, J. and Moreno, M., "The first since 1960: A large event in the Valdivia segment of the Chilean Subduction Zone, the 2016 M7. 6 Melinka earthquake". *Earth and Planetary Science Letters*, 474, pp.68-75, 2017.

Feng, W., Lindsey, E., Barbot, S., Samsonov, S., Dai, K., Li, P., Li, Z., Almeida, R., Chen, J. and **Xu, X.**, "Source characteristics of the 2015 MW 7.8 Gorkha (Nepal) earthquake and its MW 7.2 aftershock from space geodesy", *Tectonophysics*, 712, pp.747-758, 2017.

Sandwell, D.T., Zeng, Y., Shen, Z.K., Crowell, B., Murray, J., McCaffrey, R. and **Xu, X.**, The SCEC Community Geodetic Model V1: Horizontal Velocity Grid. *In SCEC Annu. Meeting*, 2016.

Xu, X., Tong, X., Sandwell, D.T., Milliner, C.W., Dolan, J.F., Hollingsworth, J., Leprince, S. and Ayoub, F., "Refining the shallow slip deficit", *Geophysical Journal International*, 204(3), pp.1867-1886, 2016.

Galetzka, J., Melgar, D., Genrich, J.F., Geng, J., Owen, S., Lindsey, E.O., **Xu, X.**, Bock, Y., Avouac, J.P., Adhikari, L.B. and Upreti, B.N...., "Slip pulse and resonance of the Kathmandu basin during the 2015 Gorkha earthquake, Nepal", *Science*, 349(6252), pp.1091-1095, 2015.

Lindsey, E.O., Natsuaki, R., **Xu, X.**, Shimada, M., Hashimoto, M., Melgar, D. and Sandwell, D.T., "Line of sight displacement from ALOS-2 interferometry: Mw 7.8 Gorkha Earthquake and Mw 7.3 aftershock", *Geophysical Research Letters*, 42(16), pp.6655-6661, 2015.

ABSTRACT OF THE DISSERTATION

Earthquake Cycle Study with Geodetic Tools

by

Xiaohua Xu

Doctor of Philosophy in Earth Sciences

University of California, San Diego, 2017

David T. Sandwell, Chair

In this dissertation, I use space-based geodetic data to study the ground deformation caused by the earthquake cycle processes. Chapter 1 is an introduction to the data I used and the motivation on each of the following chapters. Chapter 2 focuses on investigating a controversial problem brought up by several co-seismic inversions using geodetic data, which is called the shallow slip deficit. I explored whether this problem is largely an artifact of inversion due to incomplete data and refined the magnitude of this deficit. Chapter 3, develops a new data-driven spectral expansion approach for co-seismic slip inversion using geodetic data. Compared to traditional method, it isolates the unstable part of the model and only solves for the well-determined part. Meanwhile

we also developed a 1-D thermal model to understand the different down-dip rupture limits of continental-continental and continental-oceanic megathrust events. Chapter 4 aims at understanding the new TOPS mode data from Sentinel-1 satellites and fully testing the capability of this dataset. A subsidence of about 160 mm/yr at the Cerro Prieto Geothermal Field is recovered together with a 40 mm/yr tectonic fault parallel motion at the nearby region. Chapter 5 further develops the processing algorithm used in Chapter 4 and uses Sentinel-1 data to reveal both tectonic and anthropogenic deformation along the San Andreas Fault System.

Chapter 1

Introduction

It has been more than 100 years since Reid [1910] proposed his elastic rebound hypothesis after the investigation of the 1906 San Francisco earthquake. However, it was not until the development of plate tectonic theory in the 1960's that the forces driving the earthquake cycle were well understood. Most of the plate motion is accommodated along relatively narrow boundaries where the slow accumulation of interseismic elastic energy is suddenly released in earthquakes. Small earthquakes occur much more often than large ones, but it is the large earthquakes that are responsible for most of the seismic moment release. Monitoring the interseismic strain accumulation and accurately estimating the co-seismic strain release is crucial toward understanding the earthquake cycle process and evaluating the seismic hazard. Though the general characteristics of the elastic rebound theory have been understood for decades using ground-based geodetic tools such as theodolites and leveling, it was not until the dawn of space geodesy in the 1960's when it became possible to observe and monitor the crustal deformation on the scale of hundreds or thousands of kilometers. The accuracy and utility of the space geodetic tools accelerated in the 1980's with the development of the Global Positioning System (GPS) and in the 1990's with the development of the Interferometric Synthetic Aperture Radar

(InSAR).

1.1 GPS and InSAR

Global Positioning System is a satellite-based radio navigation system where its satellites transmit radio signals encoding an accurate time. A receiver on the ground computes the time difference between its local clock with the time the signal was emitted from the GPS satellite to determine the range to the satellite. Many ground receivers, with known positions, can accurately track the satellites as they orbit the Earth. This network of known positions in space provide a reference frame for accurately locating receivers having uncertain positions. The ground receiver must acquire signals from at least 4 GPS satellites to determine a 3-D position as well as to correct its internal clock. GPS is subject to many error sources, such as multi-path effects, satellite orbit perturbations, path delays caused by ionospheric and tropospheric effects, and satellite/receiver clock errors. Most of the errors are well studied and are modeled or corrected during the processing. By the early 1990's the GPS data were accurate enough to measure vector ground displacement at millimeter accuracy. Over the past two decades the scientific community has perfected and standardized the GPS processing. The tectonic applications include: determining global plate motions [DeMets et al. 1994], constructing horizontal velocity field and strain rate maps [Frank 1966; Shen, Jackson, and Ge 1996], deriving fault slip rates using block models or visoco-elastic modeling [McCaffrey 2005; Meade and Hager 2005; Smith-Konter and Sandwell 2009; Tong, Smith-Konter, and Sandwell 2014], etc. The deployment of continuous GPS network made it possible to monitor time dependent effects such as strain transients associated with episodic tremor and slip [Rogers and Dragert 2003]. The on-going effort also includes creating early-warning

system with continuous GPS [Bock, Melgar, and Crowell 2011; Goldberg and Bock 2017], taking the advantage that GPS stations can provide displacement thus a faster and more accurate moment estimate of the events can be achieved.

Interferometric Synthetic Aperture Radar, was not routinely used for monitoring surface deformation until the mid 1990's and has had a rather slow development because much of the data and software were proprietary. However over the past 4 years the development has accelerated because of a dramatic increase in the number, quality, and coverage of the InSAR satellites (Figure 1.1) [Elliott, Walters, and Wright 2016]. Moreover, the European missions now have a completely open data policy. Compared to GPS, InSAR has a much lower temporal sampling rate (12 days versus 1 second) but a much higher spatial resolution (50 m versus 20 km in California). There are a variety of InSAR applications including: construction of Digital Elevation Models (DEM) from the Shuttle Radar Topographic Mission (SRTM) [Jarvis et al. 2008] and TanDEM-X mission [Krieger et al. 2007]; responding to large earthquakes like the 2010 Maule Chile earthquake [Tong, Sandwell, and Fialko 2010], the 2015 Gorkha Nepal earthquake [Lindsey et al. 2015], etc.; mapping disasters such as forest fires [Balzter 2001] and landslides [Yin et al. 2010]; analyzing interseismic velocity and strain accumulation [Tong, Sandwell, and Smith-Konter 2013; Ryder and Bürgmann 2008]; mapping triggered fault creep [Wei, Sandwell, and Fialko 2009]; monitoring postseismic deformation due to poro-elastic [Fialko 2004], visco-elastic [Pollitz, Wicks, and Thatcher 2001] and after-slip [Wang and Fialko 2014]; monitoring volcanic deformation [Hooper et al. 2004] and more recently monitoring hydrological effects [Xu et al. 2017].

Despite the wide usage of InSAR, its full potential has not yet been reached. The processing of InSAR data varies from group to group, not only because of the
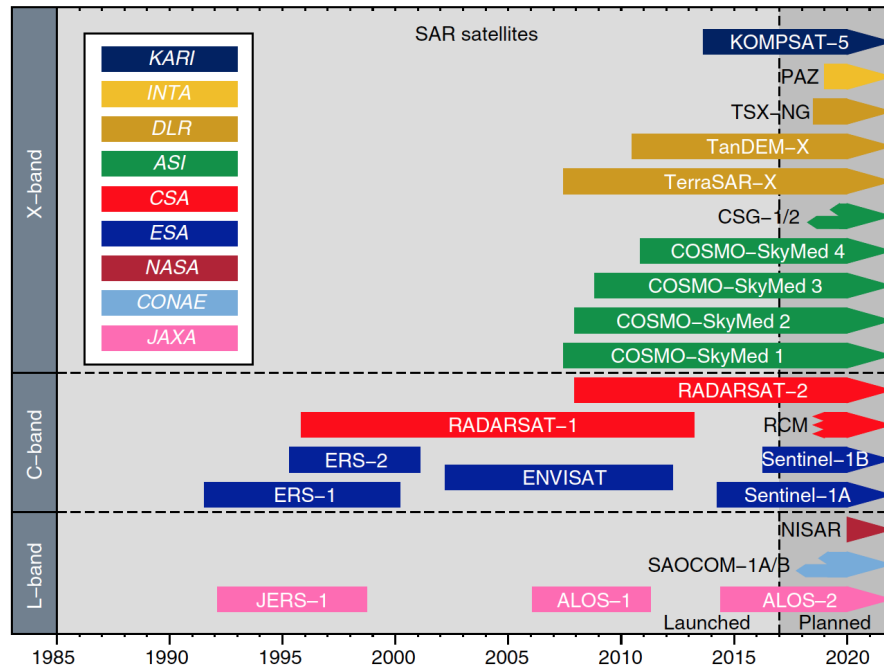
Figure 1.1: **Synthetic Aperture Radar (SAR) that have acquired images on a global basis as of late 2016** [Elliott, Walters, and Wright 2016].

complexity of the datasets and on-going development of processing techniques, but also there are a wide variety of radar sensors, with multiple bands, and multiple acquisition modes. The three most common bands are X-band (3 cm), C-band (6 cm) and L-band (24 cm). The longer wavelength L-band waves can penetrate through vegetation and are less susceptible to temporal decorrelation due to changing ground reflectors over farms and forests although they are more effected by propagation delays through the ionosphere. In contrast, the shorter wavelength X-band radars are largely unaffected by the ionosphere but signals are rapidly decorrelated over natural surfaces so they are mainly used in areas with persistent ground reflectors such as buildings or roads. The intermediate wavelength C-band radars have decorrelation times and ionospheric delays between X-band and L-band. Beyond that, InSAR satellites also have multiple acquisition modes, including stripmap mode, spotlight mode, ScanSAR mode and TOPS mode. The stripmap mode is the least complex and was used on all the early SAR satellites; the radar

illuminates a single swath ~ 80 km across track and uses synthetic aperture processing to achieve high spatial resolution in the flight direction. For the spotlight mode the radar uses beamforming to steer the illumination to particular target as it flies overhead; this provides a longer aperture to achieve higher along-track resolution than stripmap mode. Stripmap mode is more commonly used for scientific applications where continuous coverage is needed while spotlight mode is more commonly used by the military where high resolution is needed over particular targets. The ScanSAR mode was developed to provide wide-area coverage with lower spatial resolution than stripmap. It illuminates several subswaths, each ~ 70 km across to achieve a total swath ~ 300 km across. This enables full global coverage at shorter revisit times (e.g. 35 days for stripmap and 12 days for ScanSAR mode). It works as a time-division multiplexing system where the satellite separates the antenna scanning into a few sections over different sub-swaths. ScanSAR performs well on phase measurement but the amplitude of the image scallops along azimuth. Also the interference between multiple observing periods inside each sub-swath will create multiple scatters. These defects led to the design of a new burst acquisition mode, the Terrain Observation by Progressive Scans, i.e. TOPS mode. Similar to ScanSAR, it divides the observation into multiple sub-swaths. The major difference is that, during the observation inside each sub-swath, the antenna steers while it scans from backward to forward, thus creating a consistent scan with much less amplitude scalloping and no artificial scatters. The later chapters of my thesis are focussed on the development of processing methods for this new TOPS mode data being provided by the two new SAR satellites from the European Space Agency (Seintinal-1A and 1B).

1.2 Introduction to each chapter

In this dissertation, I use space space-based geodetic tools including GPS, InSAR as well as aerial/satellite photos, to study on correctly inverting the coseismic slip using geodetic dataset (Chapter 2 and Chapter 3) and robustly constructing interseismic deformation time-series along the San Andreas Fault System (Chapter 4 and Chapter 5).

1.2.1 The shallow slip deficit

The theory of plate tectonics tells us that most of the surface deformation occurs at plate boundaries while inside each plate the deformation is minimal. At these plate boundaries, larger earthquakes occur much less frequently than smaller earthquakes but they release most of the seismic moment (i.e., slip). Coseismic slip inversions of a number of recent large strike-slip earthquakes show that, the slip commonly peaks at a depth of 4-6 km with a 15% to 60% reduction at near surface. This reduced slip at shallow depth is termed as the Shallow Slip Deficit (SSD). If the shallow slip deficit is real, then there is a dilemma relating the geodetically inferred slip to the long-term geological observations. As noted by [Fialko et al. 2005], "either the elastic dislocation models are inadequate for interpretation of the coseismic deformation data, or much of the stress release in the shallow crust occurs aseismically". Geological studies show that over many earthquake cycles slip is uniform from the surface to the base of the seismogenic zone. The reduction of the coseismic slip toward deeper depths is accommodated by postseismic and interseismic deformation. However, significant shallow aseismic slip is often not observed. Both aftershock sequence [Scholz 1998; Wei et al. 2011] and postseismic relaxation [Fialko 2004; Jacobs et al. 2002] show that most of the later signals come from deeper crust. If we attribute the missing shallow slip to inelastic coseismic deformation, field work [Shelef and Oskin 2010] and dynamic simulation [Kaneko and

Fialko 2011] provide similar conclusions that this deficit should be 10% to 15%. If this non-compensated shallow slip deficit goes with long-term earthquake cycles, there is no doubt that the shallow crust will accumulate non-realistic large strain. This lead to my first study on examining whether the SSD is largely an artifact due to incomplete data coverage and re-investigating some of the large strike-slip events to refine the magnitude of this deficit (Chapter 2).

1.2.2 A spectral expansion approach for geodetic slip inversion

The inversion technique used in Chapter 2 is the traditional method, where one constructs elastic models that relate slip at depth to surface deformation by discretizing this fault into small patches before estimating the slip on each patch. The approach is straightforward but solving for the slip on each discretized patch is highly non-unique. When the Green's functions relating slip at depth to surface deformation are examined in the wavenumber domain, they contain functions having exponential attenuation with depth called upward continuation kernels. These upward continuation kernels cause the inverse problem to be ill-posed; without regularizing the Green's matrix, the solutions will have wild oscillations in slip over the fault plane. Even with careful handling of the regularization term, the solution is still path-dependent, as small changes in parameters will lead to dramatically different solutions. Moreover, the uncertainty estimate of the model will be biased by the prescribed regularization. Given these issues, we decided to explore a true inverse theory approach to slip inversion using geodetic data (Chapter 3). We adopted the spectral expansion method from linear inverse theory [Parker 1977] where instead of using regularization to suppress model instabilities, we isolate them and only solve for the parts that are well determined. Also, instead of highlighting a single model, we invert for a series of models where their uncertainty increases with

increasing model resolution. This approach helps us to understand the fundamental limitations for of given dataset. After synthetic tests, we applied this approach to the 2010 Chile earthquake (continental-oceanic) and the 2015 Nepal earthquake (continental-continental), to fully understand the down-dip resolution capabilities of these inversions. The analysis confirms that these two earthquakes from different tectonic settings have remarkably different down-dip rupture limits; ~ 20 km for the Nepal earthquake and ~ 40 km for the Chile earthquake. To better understand this difference we developed a 1-D thermal model and explored the influence from some key factors on the temperature profile (e.g. radiogenic heating, erosion/accretion rate, etc). We found that an erosion rate of 1 mm/yr has a profound effect on the geotherm which can explain the factor of 2 difference in rupture depth of these two earthquakes.

1.2.3 Exploring the usage of Sentinel-1 TOPS data

The Sentinel-1A satellite was lunched on April 3rd, 2014 and started its routine acquisition in October the same year. The satellite is a C-band radar primarily operating at TOPS mode. It is capable of revisiting the ground every 12 days although over most of Western North America, the data are collected on a 24-day cadence. The Cerro Prieto geothermal area in Baja Mexico has 12-day repeats so we have examined that area first. Processing TOPS-mode data for interferometry is very different from previous InSAR satellites because the images must be aligned to an accuracy of better than 1/200 of a pixel. This cannot be accomplished with standard image cross correlation methods which are usually accurate to 1/10 of a pixel. Other groups showed 1/200 pixel could be accomplished with purely geometric alignment using the precise orbit information. In this chapter we develop the methodology and computer codes to achieve this accuracy and thus can explore the capability of this satellite. There are significant advantages to

pure geometric alignment. The first is that using this new approach, the master and slave images can be precisely aligned even in cases where they are completely decorrelated. Because all images are aligned to a single master, the sum of interferograms around all closed loops is essentially zero with a 2Npi ambiguity. This enables phase connection between the first and last SAR image in the stack. (In Chapter 5 we show how to solve for the integer ambiguity.) We applied this algorithm together with coherence-based Small Baseline Subset (SBAS) method [Tong and Schmidt 2016] and atmospheric phase correction by common-scene stacking [Tymofyeyeva and Fialko 2015], to construct deformation time-series at the Cerro Prieto Geothermal Field (CPGF). We deliberately selected this area for several reasons. First, this is an area with known subsidence signal larger than 10 cm/yr, which can be easily captured by satellite acquisitions. Second, along with the signal from the geothermal field, this is also a tectonically active region where ~40 mm/yr deformation is distributed across the Imperial fault, the Cerro Prieto fault and the Indiviso fault, which is ideal for testing on recovering tectonic deformation. Third, this area has strong decorrelation for C-band radar images due to extensive agricultural activities. With it being an high priority zone for the Sentinel-1A mission (12-day repeat), the test on constructing long time-series with short time-span interferograms is quite suitable and the decorrelation problem will be mitigated. Fourth, this area has sparse GPS coverage, which is insufficient for building models to correct InSAR time-series. With this study, we can also examine whether the Sentinel-1 TOPS dataset can provide independent deformation measurement. Later on April 22nd, 2016, the Sentinel-1B satellite joined the Sentinel-1A in the same orbit with a 6-day separation and started to provide routine acquisitions around August. This advance further shortens the revisit time, which will facilitate the conclusions from our study.

1.2.4 Tectonic and anthropogenic deformation along the San Andreas Fault revealed by GPS and the Sentinel-1 Satellites

The San Andreas Fault System (SAFS) is one of the best studied transform fault system in the world. Over historical time it has generated several magnitude 7+ strike-slip earthquakes [Wallace 1970]. The SAFS passes through one of the most highly populated and economically developed region in the world so the next major earthquake along the SAF will have significant impacts on population and property. Moreover, the southern section of the SAR has not had a major event in the past 327 years so it is capable of generating a magnitude 7.8 earthquake [Jones et al. 2008] (i.e., The Big One). Given these facts, is it important to: monitor the slow interseismic ground deformation of this fault system; estimate the moment accumulation rate on individual fault segments; and assess the seismic hazard throughout the region. There have been many studies to measure the secular tectonic and anthropogenic deformation along this system using both GPS and InSAR data. GPS data provide important time series of deformation at widely-spaced sites ($\sim$20 km). InSAR time series have also been constructed in selected areas although the irregular cadence of the older InSAR measurements as well is the sometimes poor baseline control have provided significant challenges. The new data from the Sentinel-1 A and B satellites now have the attributes that are needed for accurate InSAR time series of the SAFS having 3 month temporal resolution. In this chapter we develop best practices for merging InSAR and GPS along the entire SAFS. Three years of InSAR data is insufficient to accurately recover the seasonal and secular signals so the analysis in this chapter is important for developing the methods to use over the next two decades of planned Sentinel-1 acquisitions. One important result from this chapter is the development of a method to invert for the integer phase ambiguity in each interferogram. This extends the analysis from Chapter 4 to provide an absolute phase

connection between the first and last SAR image in the stack.

1.3   GMTSAR

During my PhD, I also worked as a developer on an open source InSAR processing software GMTSAR [Sandwell et al. 2011] together with my advisor and others. The aim of our development is to lower the prerequisite for users to correctly and efficiently process InSAR data. The software divides the processing into pre-processing, generating interferogram and post-processing. The pre-processing step converts the InSAR data to a format that can be read by the software and perform image co-registration. The generation of interferogram includes generating topographic phase, and performing interferometry. The post-processing step mainly deals with phase unwrapping and geocoding. These steps are the same for different satellites except pre-processing, mainly because they have different data format and different processing level. During my PhD, I wrote pre-processors for a number of satellites, including TerraSAR-X, RADARSAT-2, COSMO-SkyMed, Sentinel-1 stripmap and Sentinel-1 TOPS, all of which are now available in GMTSAR. Guided by my advisor, I also implemented a full processing chain, including data manipulation, batch processing, time-series analysis, etc., for TOPS data.

References

Balzter, H. (2001). "Forest mapping and monitoring with interferometric synthetic aperture radar (InSAR)". In: *Progress in physical geography* 25.2, pp. 159–177.

Bock, Y., Melgar, D., and Crowell, B. W. (2011). "Real-time strong-motion broadband displacements from collocated GPS and accelerometers". In: *Bulletin of the Seismological Society of America* 101.6, pp. 2904–2925.

DeMets, C., Gordon, R. G., Argus, D. F., and Stein, S. (1994). "Effect of recent revisions to the geomagnetic reversal time scale on estimates of current plate motions". In: *Geophysical research letters* 21.20, pp. 2191–2194.

Elliott, J., Walters, R., and Wright, T. (2016). "The role of space-based observation in understanding and responding to active tectonics and earthquakes". In: *Nature communications* 7, p. 13844.

Fialko, Y. (2004). "Evidence of fluid-filled upper crust from observations of postseismic deformation due to the 1992 Mw7. 3 Landers earthquake". In: *Journal of Geophysical Research: Solid Earth* 109.B8.

Fialko, Y., Sandwell, D., Simons, M., and Rosen, P. (2005). "Three-dimensional deformation caused by the Bam, Iran, earthquake and the origin of shallow slip deficit". In: *Nature* 435.7040, pp. 295–299.

Frank, F. (1966). "Deduction of earth strains from survey data". In: *Bulletin of the Seismological Society of America* 56.1, pp. 35–42.

Goldberg, D. and Bock, Y (2017). "Self-contained local broadband seismogeodetic early warning system: Detection and location". In: *Journal of Geophysical Research: Solid Earth* 122.4, pp. 3197–3220.

Hooper, A., Zebker, H., Segall, P., and Kampes, B. (2004). "A new method for measuring deformation on volcanoes and other natural terrains using InSAR persistent scatterers". In: *Geophysical research letters* 31.23.

Jacobs, A., Sandwell, D., Fialko, Y., and Sichoix, L. (2002). "The 1999 (Mw 7.1) Hector Mine, California, earthquake: Near-field postseismic deformation from ERS interferometry". In: *Bulletin of the Seismological Society of America* 92.4, pp. 1433–1442.

Jarvis, A., Reuter, H. I., Nelson, A., and Guevara, E. (2008). "Hole-filled SRTM for the globe Version 4". In: *available from the CGIAR-CSI SRTM 90m Database (http://srtm. csi. cgiar. org)*.

Jones, L. M., Bernknopf, R., Cox, D., Goltz, J., Hudnut, K., Mileti, D., Perry, S., Ponti, D., Porter, K., Reichle, M., Seligson, H., Shoaf, K., Treiman, J., and Wein, A. (2008). "The shakeout scenario". In: *US Geological Survey Open-File Report* 1150, p. 308.

Kaneko, Y and Fialko, Y. (2011). "Shallow slip deficit due to large strike-slip earthquakes in dynamic rupture simulations with elasto-plastic off-fault response". In: *Geophysical Journal International* 186.3, pp. 1389–1403.

Krieger, G., Moreira, A., Fiedler, H., Hajnsek, I., Werner, M., Younis, M., and Zink, M. (2007). "TanDEM-X: A satellite formation for high-resolution SAR interferometry". In: *IEEE Transactions on Geoscience and Remote Sensing* 45.11, pp. 3317–3341.

Lindsey, E. O., Natsuaki, R., Xu, X., Shimada, M., Hashimoto, M., Melgar, D., and Sandwell, D. T. (2015). "Line-of-sight displacement from ALOS-2 interferometry: Mw 7.8 Gorkha Earthquake and Mw 7.3 aftershock". In: *Geophysical Research Letters* 42.16, pp. 6655–6661.

McCaffrey, R. (2005). "Block kinematics of the Pacific–North America plate boundary in the southwestern United States from inversion of GPS, seismological, and geologic data". In: *Journal of Geophysical Research: Solid Earth* 110.B7.

Meade, B. J. and Hager, B. H. (2005). "Block models of crustal motion in southern California constrained by GPS measurements". In: *Journal of Geophysical Research: Solid Earth* 110.B3.

Parker, R. L. (1977). "Understanding inverse theory". In: *Annual Review of Earth and Planetary Sciences* 5.1, pp. 35–64.

Pollitz, F. F., Wicks, C., and Thatcher, W. (2001). "Mantle flow beneath a continental strike-slip fault: Postseismic deformation after the 1999 Hector Mine earthquake". In: *Science* 293.5536, pp. 1814–1818.

Reid, H. F. (1910). *The mechanics of the earthquake*. Vol. 2. Carnegie institution of Washington.

Rogers, G. and Dragert, H. (2003). "Episodic tremor and slip on the Cascadia subduction zone: The chatter of silent slip". In: *Science* 300.5627, pp. 1942–1943.

Ryder, I. and Bürgmann, R. (2008). "Spatial variations in slip deficit on the central San Andreas fault from InSAR". In: *Geophysical Journal International* 175.3, pp. 837–852.

Sandwell, D., Mellors, R., Tong, X., Wei, M., and Wessel, P. (2011). "Open radar interferometry software for mapping surface deformation". In: *Eos, Transactions American Geophysical Union* 92.28, pp. 234–234.

Scholz, C. H. (1998). "Earthquakes and friction laws". In: *Nature* 391.6662, pp. 37–42.

Shelef, E. and Oskin, M. (2010). "Deformation processes adjacent to active faults: Examples from eastern California". In: *Journal of Geophysical Research: Solid Earth* 115.B5.

Shen, Z.-K., Jackson, D. D., and Ge, B. X. (1996). "Crustal deformation across and beyond the Los Angeles basin from geodetic measurements". In: *Journal of Geophysical Research: Solid Earth* 101.B12, pp. 27957–27980.

Smith-Konter, B. and Sandwell, D. (2009). "Stress evolution of the San Andreas fault system: Recurrence interval versus locking depth". In: *Geophysical Research Letters* 36.13.

Tong, X, Sandwell, D., and Smith-Konter, B (2013). "High-resolution interseismic velocity data along the San Andreas fault from GPS and InSAR". In: *Journal of Geophysical Research: Solid Earth* 118.1, pp. 369–389.

Tong, X., Sandwell, D. T., and Fialko, Y. (2010). "Coseismic slip model of the 2008 Wenchuan earthquake derived from joint inversion of interferometric synthetic aperture radar, GPS, and field data". In: *Journal of Geophysical Research: Solid Earth (1978–2012)* 115.B4.

Tong, X. and Schmidt, D. (2016). "Active movement of the Cascade landslide complex in Washington from a coherence-based InSAR time series method". In: *Remote Sensing of Environment* 186, pp. 405–415.

Tong, X., Smith-Konter, B., and Sandwell, D. T. (2014). "Is there a discrepancy between geological and geodetic slip rates along the San Andreas Fault system?" In: *Journal of Geophysical Research: Solid Earth* 119.3, pp. 2518–2538.

Tymofyeyeva, E. and Fialko, Y. (2015). "Mitigation of atmospheric phase delays in InSAR data, with application to the eastern California shear zone". In: *Journal of Geophysical Research: Solid Earth* 120.8, pp. 5952–5963.

Wallace, R. E. (1970). "Earthquake recurrence intervals on the San Andreas fault". In: *Geological Society of America Bulletin* 81.10, pp. 2875–2890.

Wang, K. and Fialko, Y. (2014). "Space geodetic observations and models of postseismic deformation due to the 2005 M7. 6 Kashmir (Pakistan) earthquake". In: *Journal of Geophysical Research: Solid Earth* 119.9, pp. 7306–7318.

Wei, M., Sandwell, D., and Fialko, Y. (2009). "A silent Mw 4.7 slip event of October 2006 on the Superstition Hills fault, southern California". In: *Journal of Geophysical Research: Solid Earth* 114.B7.

Wei, S., Fielding, E., Leprince, S., Sladen, A., Avouac, J.-P., Helmberger, D., Hauksson, E., Chu, R., Simons, M., Hudnut, K., Herring, T., and Briggs, R. (2011). "Superficial simplicity of the 2010 El Mayor–Cucapah earthquake of Baja California in Mexico". In: *Nature geoscience* 4.9, pp. 615–618.

Xu, X., Sandwell, D. T., Tymofyeyeva, E., González-Ortega, A., and Tong, X. (2017). "Tectonic and Anthropogenic Deformation at the Cerro Prieto Geothermal Step-Over Revealed by Sentinel-1A InSAR". In: *IEEE Transactions on Geoscience and Remote Sensing*.

Yin, Y., Zheng, W., Liu, Y., Zhang, J., and Li, X. (2010). "Integration of GPS with InSAR to monitoring of the Jiaju landslide in Sichuan, China". In: *Landslides* 7.3, pp. 359–365.

Chapter 2

Refining the Shallow Slip Deficit

Geodetic slip inversions for three major ($Mw > 7$) strike-slip earthquakes (1992 Landers, 1999 Hector Mine, and 2010 El Mayor-Cucapah) show a 15% to 60% reduction in slip near the surface (depth < 2 km) relative to the slip at deeper depths (4 to 6 km) [Fialko et al. 2005; Fialko et al. 2010]. This significant difference between surface coseismic slip and slip at depth has been termed the shallow slip deficit (SSD). The large magnitude of this deficit has been an enigma since it cannot be explained by shallow creep during the interseismic period or by triggered slip from nearby earthquakes. One potential explanation for the SSD is that the previous geodetic inversions lack data coverage close to surface rupture such that the shallow portions of the slip models are poorly resolved and generally underestimated. In this study, we improve the static coseismic slip inversion for these three earthquakes, especially at shallow depths, by: 1) including data capturing the near-fault deformation from optical imagery and SAR azimuth offsets; 2) refining the InSAR processing with non-boxcar phase filtering, model-dependent range corrections, more complete phase unwrapping by SNAPHU(Statistical Non-linear Approach for Phase Unwrapping) assuming a maximum discontinuity and an on-fault correlation mask; 3) using more detailed, geologically constrained fault geometries; and 4) incorporating

additional campaign GPS data. The refined slip models result in much smaller SSDs of 3% to 19%. We suspect that the remaining minor SSD for these earthquakes likely reflects a combination of our elastic model's inability to fully account for near-surface deformation, which will render our estimates of shallow slip minima, and potentially small amounts of interseismic fault creep or triggered slip, which could "make up" a small percentages of the coseismic SSD during the interseismic period. Our results indicate that it is imperative that slip inversions include accurate measurements of near-fault surface deformation to reliably constrain spatial patterns of slip during major strike-slip earthquakes.

2.1 Introduction

Maps of relative, line-of-sight, surface deformation from interferometric synthetic aperture radar (InSAR) combined with absolute vector measurements from point GPS data have enabled the mapping of the 3-D surface displacement for many large earthquakes [Fialko, Simons, and Agnew 2001]. If the fault plane is well defined by geological field mapping and aftershocks, then elastic models can be used to invert for the spatial variations of slip at depth. The equations relating slip at depth to surface deformation include an upward continuation term that dramatically attenuates the rupture signal at wavelengths smaller than the depth, so model resolution generally decreases exponentially with increasing depth (Figure S2.5). Thus, slip at shallow depths is well resolved whereas the spatial variations in deeper slip are poorly resolved. This poor resolution, combined with a smoothness constraint, results in a spatially smooth slip model at the base of the seismogenic zone [Tong, Sandwell, and Fialko 2010]. By using combined InSAR and GPS data, detailed slip inversions have been performed for several large strike-slip earthquakes in southern and Baja California, including the

M_w7.3 Landers, M_w7.1 Hector Mine and the M_w7.2 El Mayor Cucapah. The previous slip models for these earthquakes share a common attribute, in that their cumulative along-strike slip is largest between 2-6 km depth, with a 15% to 60% reduction in slip at shallower depth [Fialko et al. 2005; Fialko et al. 2010] (Figure 2.1). This feature is called the shallow slip deficit. When averaged over many earthquake cycles, the slip on a major fault should be uniform with depth and equal to the sum of the co-, post-, and interseismic slip [Reid and Lawson 1910; Tse and Rice 1986]. The reduction in coseismic slip at the base of the seismogenic zone is explained by post- and inter-seismic slip. Near the surface, however, there is not enough steady interseismic creep or triggered slip to account for the observed SSD [Wei, Sandwell, and Fialko 2009; Kaneko et al. 2015]. The assessment and understanding of this SSD is important for paleoearthquake magnitude estimation, geologists' mapping of surface coseismic slip after earthquakes and understanding the relation between surface rupture and slip at depth [Dolan and Haravitch 2014]. It is also crucial in predicting strong ground motion and is thus critically important for accurate seismic hazard evaluation [Pitarka et al. 2009].

Previous studies have investigated physical processes to explain the SSD, but can only account for about a 15% reduction in shallow slip by distributed deformation of the uppermost few kilometers surrounding the fault [Kaneko and Fialko 2011]. Seismic imaging and geologic mapping show the uppermost few kilometers of the crust above a strike-slip fault has "V-shaped damage zone" having a locally reduced seismic velocity [Zhang, Thurber, and Bedrosian 2009]. In addition, thick sediments (greater than 2 km) promote velocity strengthening behavior, which has been proposed to result in shallow creep [Rice and Tse 1986]. These processes suggest that inelastic off-fault deformation could explain a maximum coseismic slip deficit of about 15%. However, compared to the observed 46% surface silip deficit in Landers earthquake and 60% in El Mayor-Cucapah

earthquake [Fialko et al. 2005; Fialko et al. 2010], this small amount is insufficient to explain the entire SSD.

Here we investigate whether the SSD is largely an artifact due to incomplete data coverage close to the rupture zone for 1992 Landers, 1999 Hector Mine and 2010 El-Mayor Cucapah earthquakes, all of which share similar tectonic settings (Figure 2.2). These major ruptures, each of which exhibited a large SSD, also had large near-fault ground motions and accelerations that caused strong decorrelation of the radar interferograms, making the exact near-fault measurement of surface deformation impossible. We first use inversions of synthetic InSAR data, with a variety of near-fault data gaps, to show that poor coverage of the near-fault surface deformation pattern can explain a significant part of the observed SSD. We then assemble additional near fault deformation data from optical image analysis, better geological mapping of the fault trace, more refined InSAR data processing, and more complete GPS data coverage for all three of these major strike-slip ruptures and invert for the slip at depth. We show that much smaller SSDs are consistent with all the observations and discuss possible explanations for the remaining minor SSDs.

2.2   Synthetic Test

To understand how a lack of near-fault data coverage could result in an underestimation of the shallow slip, we performed two synthetic tests. We constructed an uniform elastic half-space model that consists of a 30-km-long and 20-km-wide fault placed at a $150°$ strike and $65°$ dip (Figure 2.3a). The slip along the fault varies as a Gaussian function tapering to zero toward the ends of the fault trace. The cumulative slip along strike is 60 m·km for each layer down to a depth of 8.2 km where the slip goes to

zero (9km width on the fault plane). From the forward model we generated the surface displacement field, and added Gaussian noise that is 2% of the local signal amplitude. We then performed two inversions with two different-sized data gaps around the fault - a small 2-km-wide, 32-km-long elliptical gap and a larger 10-km-wide and 32-km-long elliptical gap (Figure 2.3b). Inversions were carried out using the exact fault geometry, a non-negative strike-slip constraint, and a gradient smoothing constraint. In both cases, the lower part of the model (Figure 2.3c, 2.3d) had a more gradual reduction in slip than the near-step input. In addition they both showed an overestimate of slip at intermediate depth (3-5 km). The case with the small data gap, showed a reduction of surface slip with respect to the peak slip of 5% while the case with the large data gap had a 18% reduction of surface slip with respect to the peak (Figure 2.3e, 2.3f). Interestingly, for the model with the wide gap, most of this apparent SSD is not due to a slip mismatch at the surface, but due to an overestimate of slip at 4 km. An additional test with full data coverage was done (Figure S2.4), but no significant difference was found in the inverted slip compared to the 2-km gapped case. This experiment demonstrates that the missing near-fault data, combined with a smoothed, non-negative inversion, may result in a lower surface slip relative to the slip in the center of the seismogenic zone. These synthetic tests demonstrate that near-fault data are necessary in order to reliably quantify near-surface slip.

2.3   Data Preparation

Our re-analysis of the SSD is based on improved data coverage as well as improved analysis methods for the three large strike-slip earthquakes in southern and Baja California ($M_w = 7.3$ Landers, $M_w = 7.1$ Hector Mine, and the $M_w = 7.2$ El Mayor Cucapah). We begin by assembling near-fault optical imagery data of repeated images from

aircraft (1 m ground resolution) as well as the SPOT satellite (10 m ground resolution). We then reanalyze all the interferometry from these three earthquakes using improved non-boxcar (i.e., non-multilook) filters and better phase unwrapping close to the rupture by explicitly allowing for a phase discontinuity [Chen and Zebker 2001]. Finally, we use all available continuous and campaign vector GPS data to better constrain the slip in the deeper parts of the ruptures.

2.3.1   Optical Imagery Data

We assembled near-fault optical imagery data of repeated images from aircraft as well as the SPOT satellite [Hollingsworth AGU 2012]. We assembled high-resolution, National Aerial Photography Program photographs (1 m ground resolution, compared to 4 m for InSAR, purchased from the USGS (http://earthexplorer.usgs.gov) to provide better constraints on surface deformation patterns close to the fault [Milliner et al. 2015]. Images acquired prior to the earthquakes were correlated with images acquired after the earthquakes using the COSI-Corr software [Leprince et al. 2007]. To produce correlation maps that accurately constrain the ground deformation pattern, the input aerial photographs must be precisely ortho-rectified and co-registered before correlation. The COSI-Corr procedure allows for accurate ortho-rectification of images by taking into account the topography using a 10 m, national elevation dataset (NED), digital elevation model (DEM), the internal camera geometry using a camera calibration report, and the exterior orientation (look angle and altitude) determined from ground control points (GCPs) [Ayoub, Leprince, and Avouac 2009]. The pre-and post-event photographs were co-registered by constructing a relative mapping between image pairs using tie points that relate common features that were observable in both the pre- and post-earthquake images. To correlate the images we used a multi-scale sliding window size (64 and

32 pixels) with a 6-pixel step, which from multiple tests were found to be the optimal correlation parameters [Milliner et al. 2015]. This process yields two displacement maps, representing pixel motion in the east-west and north-south horizontal directions (Figure 2.4). This methodology allows for detection of pixel shifts down to an accuracy of 1/10th the size of the input image pixel dimension, which is related to the image texture and degree of temporal decorrelation [Michel and Avouac 2006; Leprince et al. 2007; Ayoub, Leprince, and Avouac 2009].

To measure the total surface displacement across the entire width of surface deformation we used stacked profiles orientated perpendicular to the fault strike [Milliner et al. 2015]. Specifically, we used profiles that ranged from 1-2 km in length (perpendicular to fault) that were stacked over a 138-m, along-strike length (i.e., fault-parallel), which allows for suppression of noise. We applied a linear regression to the observed deformation signal on either side of the fault and the relative offset of the regressions defines the total displacement accommodated across the entire fault-zone. Thus, the COSI-Corr displacement value includes both the localized, on-fault displacement that occurs on the primary fault strand, as well as any off-fault, distributed inelastic shear accommodated via a range of physical processes [Milliner et al. 2015] (Figure 2.5). Our surface offset estimates for these earthquakes are derived from the COSI-Corr analysis of aerial images for the Landers earthquake and of SPOT images for the Hector Mine and the El-Mayor Cucapah earthquakes. Subsampling and projection were made to for these data subjecting to our models' traces, in order to assemble across-fault offset data set for inversions. (Figure 2.5, 2.6, and 2.7).

2.3.2   InSAR Data

Repeat-pass interferometry spanning an earthquake provides very high spatial resolution coverage for the line of sight displacement between any two points in the interferogram [Massonnet et al. 1993; Massonnet et al. 1994; Zebker et al. 1994]. There are two main error sources in the analyses of these data. First, the large spatial scale motion (> 40 km) can be contaminated by orbital trends and large-scale atmospheric and ionospheric phase delays. We dealt this during the inversion by including mean and trend parameters in the inversion to absorb the error [Simons, Fialko, and Rivera 2002]. The second error source is related to phase unwrapping, especially close to the rupture where phase gradients are large and the InSAR coherence is low due to surface disruption from the strong ground accelerations. We increased the accuracy and coverage of the phase unwrapping close to the fault by two improvements in the processing. The first is related to the filtering of the interferogram. Previous studies have used a multi-look filter (i.e. a boxcar average) [Simons and Rosen 2007] to suppress phase noise. However, in regions where the phase gradient approaches 2π per pixel, the spectral leakage of this filter will increase the phase noise. We have replaced the boxcar with a narrow Gaussian filter to recovered more phase data in the high gradient regions [Huang and Van Genderen 1997; Sandwell and Price 1998]. The optimal cutoff wavelength of the low-pass filter depends on the coherence of the interferogram. For the higher quality interferograms (e.g., Hector Mine descending pair with average correlation being 0.69) we used a filter with a 0.5 gain at a half-wavelength of 50 m while for other, more poorly correlated interferograms (e.g., Landers descending pair with average correlation being 0.22), a wider filter was used (0.5 gain at a half-wavelength of 100 m).

The second main improvement in our near-fault InSAR analysis is related to recent improvements in phase unwrapping methods. Chen and Zebker [2001] developed

a method using Statistical-cost Network-flow Algorithm for Phase Unwrapping (SNA-PHU), which constructs a generalized cost function solving for a maximum a posterior probability estimation that approximates a L_0 solution for minimizing the phase gradient differences between wrapped and unwrapped phase. This L_0 norm solution is in accordance with the assumption that the total length of the discontinuity in the deformation field should be as short as possible. Besides, the algorithm also explicitly includes a maximum phase discontinuity parameter that allows for a sharp phase change across the discontinuity.

We optimized and tested the ability of this unwrapping algorithm to accurately recover phase near the fault by varying the discontinuity parameter (DEFOMAX) and also constructing a near fault decorrelation mask (Figure S2.3). The decorrelation mask provided information on the region where a phase discontinuity should exist and the discontinuity parameter specifies the maximum size of the phase discontinuity across the rupture. We systematically increased the assumed discontinuity value from zero to 100 cycles of radians (i.e. a large enough value for significant rupture, approximately 89 cm for C band and 376 cm for L band). In addition, we carefully perturbed the width of the masked area. The optimal discontinuity value and fault mask width were established for each interferogram through visual inspection, and the most unstable part of the interferogram were masked. Typically the mask width is about 0.5 km for a well correlated interferogram and 1.5 km for a poorly correlated interferogram and the assumed maximum discontinuity varies depending on the look angle and the magnitude of the rupture.

To assess the accuracy of the new unwrapping method, we performed a more detailed evaluation for the Landers rupture area. We compared the line of sight defor-

mation field on three profiles along with the prediction from a previous model [Fialko 2004] and the fault offset estimation from high-resolution optical image pixel tracking (Figure 2.8). The results show a good agreement between the new unwrapped phase (red dots) and the COSI-Corr estimates (magenta vertical lines), whereas the previous model's prediction shows a significant discrepancy near the fault. This improvement in rear-fault phase unwrapping combined with the COSI-corr measurements of the surface deformation pattern yields much improved estimates of total slip. The inclusion of such information about near-fault surface deformation is of critical importance for estimating coseismic shallow in the uppermost few kilometers of seismic ruptures.

The new filtering and phase unwrapping was performed on the following interferograms spanning the three major earthquakes: 1) Landers 1992/06/24 - C-band ERS1 data, 2) Hector Mine 1999/10/16 - C-band ERS2 data. 3) El Major-Cucapah 2010/04/04 - Both C-band ENVISAT data and L-band ALOS data were used. (Table 2.1, Figure 2.9, 2.10, 2.11). These data sets are sub-sampled according to the curvature of the displacement field and different weights are pre-assigned before they are applied to our inversion, according to the sampling area [Simons, Fialko, and Rivera 2002].

2.3.3 GPS data

Unlike InSAR data which sometimes have significant orbital errors and are subject to atmospheric noise, the GPS data are usually more accurate, especially over wavelengths greater than 40 km. These less-dense but more accurate data help to constrain the slip on the deeper parts of the model. Moreover, since the 1992 Landers and 1999 Hector Mine earthquakes, additional campaign GPS data have been collected, which improves spatial coverage with respect to the data coverage used in the original slip-model

publications. We used data from 82 GPS stations for the 1992 Landers earthquake [Bock et al. 1993](Figure 2.12), and 77 GPS stations for the 1999 Hector Mine earthquake [Agnew et al. 2002](Figure 2.13). For the 2010 El-Mayor Cucapah earthquake, we used observations of 158 GPS stations from both the Plate Boundary Observatory(PBO) and the Centro de Investigacion Cientifica y de Educacion Superior de Ensenada (CICESE) network (Figure 2.14). Even though the near field measurements for the El Mayor-Cucapah earthquake are concentrated on one side of the fault, they provide an important constraint on the coseismic slip pattern. The weights for the inversion are pre-assigned according to the uncertainty in each observation.

2.4   Inversion

For each of the three earthquakes, we performed joint inversions using the available geodetic data (Table 2.1) with an uniform elastic half-space model [Simons, Fialko, and Rivera 2002; Tong, Sandwell, and Fialko 2010]. The InSAR data provide much of the information for the joint inversions. For each earthquake, we used the best quality data from both ascending and descending look directions. In addition, we used the best-correlated azimuth offsets for each earthquake (Figures 2.9g, 2.10g and 2.11p). These data provide 3-D coverage except close to the fault, where the InSAR correlation is sometimes poor. In these near-fault areas the optical imagery data provide much of the information for the inversions. We began the modeling by using the fault geometry of published fault models [Fialko 2004; Simons, Fialko, and Rivera 2002; Fialko et al. 2010]. However, the surface fault traces from these models sometimes conflicted with the more accurate and detailed trace from USGS fault maps. In these cases we refined the positions of our models' traces following the fault maps. Green's functions, which relate fault slip on a single patch at depth to movement of the ground surface, are computed

using an Okada solution [Okada 1992]. We assign individual weights for each data set and put them along with the dip angle for each fault segment as non-linear parameters to be inverted for. An optimal solution is given when the parameter search gives less than 0.1% increment in the fitting. The plots of intersections in our model space, along the weights, show the competence between these datasets (Figure S2.1). A proper set of weights are given when these datasets are fitted almost equally well. Here we used the percentage of fitting reduction p instead of absolute RMS misfit as a criteria since these data sets have different noise levels and cannot be treated as equally reliable. For example, the azimuth offset data are noisier than the LOS data, so they were down-weighted in the inversion. The formula of p is given as

$$p = [1 - \frac{(Gm-d)^2}{d^2}] \times 100\% \tag{2.1}$$

where G is the Green's matrix, m is our model and d is our observation. The inversion solved for the right-lateral strike slip and dip slip for each segment. A first derivative smoothing operator was applied in order to prevent the model from over-fitting. No extra smoothness along dip was added to keep the fault strike-slip and no bottom or edge damp constraints were set. It is well known that a small change in smoothness factor may cause a large magnitude difference in the slip distribution, as smaller smoothing factor usually gives spiky solution and a larger one may smear this out. Varying this parameter has a strong influence on the estimation of shallow slip deficit. As is shown in the previous section, our results potentially will give a reduction in the shallow deficit, and in order not to underestimate this deficit (or over reduce it), we try to give less smoothness and do not introduce any other constraints. Again, we used the percentage of reduction as the parameter for selection, because the "L-curve" method, i.e. finding the balanced position between data misfit and model roughness, depends strongly on

the scale of plotting, for example, part of the "L-curve" is still an "L-curve", but the position of inflection is different. We chose the smoothing factor that correspond to the start of decrease in fitting on an absolute scale (Figure S2.2, dash-line). By doing this, the reduction of the shallow deficit in our analysis can be considered as the minimum.

From these results, we conclude that incorporating the near-fault offset measurements results in better resolution in the shallower part of the inversion model. Interestingly, for this weighted least-square process, the weight of the COSI-Corr, near-fault data set showed an independence from other data sets, which means a reasonable weight decrease or increase (before this causes numerical instability) on this data set does not significantly sacrifice the fitting of other data sets (Figure S2.1). This unexpected independence not only proves the importance of including near-fault displacement measurements, but also highlights the possible uncertainties in previous inversion studies that lack this type of near-fault surface deformation constraint.

Our reanalysis shown in Figures 2.15, 2.16 and 2.17,, also provides refined equivalent moment-magnitude estimates of 7.3 for the Landers earthquake, 7.1 for the Hector Mine earthquake and 7.2 for the El Mayor-Cucapah earthquake, assuming a typical value for the shear modulus of the Earth's crust (30GPa). These results agree well with the seismological GCMT [Dziewonski, Chou, and Woodhouse 1981] solution. The main new features of our reanalyzed models provided more accurate shallow slip estimates due to the addition of the near-fault data. When we integrated along-strike, the new cumulative strike-slip versus depth (Figure 2.18) shows shallow slip deficits ranging from 3% to 18%, which are much smaller than previous studies. Nevertheless, in all three cases the near-fault data require the surface slip to be lower than the modeled slip in the 4-6 km depth range. As discussed below, however, we suspect that much, or even

all, of these remaining small shallow slip deficits may be more likely to be artifacts of inversion.

2.5   Discussion

Previous models of three large-magnitude strike-slip earthquakes based on high-quality geodetic data all yielded a deficit of coseismic slip on the uppermost few kilometers of the fault; this was attributed to a velocity strengthening behavior in the shallowest part of the crust. The discrepancy in slip at the surface compared to that at depth suggested by the earlier models ranged up to several meters, which is much larger than could be compensated for by other seismic or aseismic mechanisms [Fialko et al. 2005]. This result not only brought challenges to theoretically explaining the earthquake cycle process but also introduced concerns that surface slip measurement might not be representative of slip at seismogenic depths. If true, this would suggest the underestimation of fault slip rate, with commensurate underestimation of probabilistic seismic hazard [Brune and Anooshehpoor 1998; Hollingsworth et al. 2012; King and Wesnousky 2007]. Kenako and Fialko [2011] demonstrated from dynamic rupture simulations that inelastic off-fault deformation could, at most, account for a 15% shallow deficit. Moreover, they showed that, because using purely elastic models may underestimate the true near-surface slip by an additional 10%, consideration of both factors could explain SSDs of as much as 25%. Although this can explain much of the observed SSDs, the artifacts arising from these factors, by themselves, are not sufficient for explaining the very large shallow slip deficits observed for the Landers and the El Mayor-Cucapah earthquakes. Here, by introducing detailed near-fault surface deformation data and more accurate representations of the fault surface geometries, we generated more robust estimation of coseismic slip inversions, as well as refined estimates of the magnitude of the surface slip deficits. Specifically, we

found a significant reduction of the discrepancy between slip at the surface and that at depth for all three large strike-slip earthquakes that we studied, with the shallow deficit for Landers Earthquake being reduced from 46% to 18%, Hector Mine from 18% to 3%, and El Mayor-Cucapah from 60% to 11%. These results are consistent with our synthetic tests, which showed that the increased data coverage would lead to a more accurate fault slip model.

Some previous studies of major earthquakes showed only minor residuals after inversion [Jónsson et al. 2002; Simons, Fialko, and Rivera 2002; Fialko 2004]. In contrast, our study shows that, after performing the inversion, large residuals still exist around the immediate vicinity of the fault. Part of the reason is that we used more near-fault data that has larger error. Also, we need to note the fact that a simplified fault geometry, as used in most inversions, is unable to represent a complicated surface rupture, we believe these large residuals mostly come from near-fault inelastic deformation, even though it could be argued that they may be associated with unwrapping errors. The good correspondence between our unwrapped phase and the fault offset estimates, however, gives us more confidence in the phase unwrapping results. An additional consideration in documenting the SSD is that elastic models may overestimate slip at about 4km depth, if the true condition is elasto-plastic [Kaneko and Fialko 2011]. Thus, our estimates of SSD ranging from 3% - 18% may still overestimate the deficits in these earthquakes, suggesting that the true deficits may be even smaller, or close to zero.

Field surveys of large-magnitude surface ruptures commonly show wide variability in structural style and the variability of on-fault versus off-fault deformation. For example, along many surface ruptures, particularly those on faults with small cumulative displacements (i.e., structurally immature faults) and at major structural complexities

along more-mature faults, it is revealed that some fault sections exhibit zones of widely

distributed surface deformation that encompass numerous small secondary structures

(e.g., minor fault strands and distributed cracking), as well as truly distributed deforma-

tion, such as folding, waping [Dolan and Haravitch 2014; Treiman et al. 2002; Rockwell

et al. 2002]. Collectively, these structures accommodate distributed inelastic deformation

in the near surface region around the main fault rupture. The style, magnitude, and width

of these zones of inelastic damage vary from rupture to rupture, likely in response to

numerous factors, including the structural maturity of the fault, the detailed structural

geometry of the surface rupture, and the type and thickness of near-surface geological

materials through which the ruptures propagates [Dolan and Haravitch 2014]. In the

1999 Hector Mine earthquake, for example, the sections of the rupture that extended

the surface in bedrock [Treiman et al. 2002] exhibited a relatively small discrepancy

between geological surface displacements and estimates of slip at depth from geodetically

constrained inversions [Jónsson et al. 2002; Simons, Fialko, and Rivera 2002], indicating

relatively minor amounts of near-fault inelastic deformation. Conversely, sections of

the rupture that extended to the surface through thick sediments showed a much larger

discrepancy between on-fault surface displacements and slip at depth from the inversions

[Dolan and Haravitch 2014]. These very different surface deformation patterns along

different parts of the Hector Mine rupture are consistent with the fact that the section of

the surface rupture that ruptured through bedrock exhibited only a small decorrelated area

near the fault, despite the large magnitude of the earthquake, and the interferogram for

this event is usually considered to be the best earthquake interferogram yet determined for

a major earthquake. In marked contrast, the 2010 Mw = 7.1 Darfield earthquake exhibited

almost no discrete faulting as part of the surface rupture, despite overall displacements at

the surface reaching 5 m [Van Dissen et al. 2011]. Rather, the surface deformation was

expressed as 30- to 300-m-wide zones of distributed faulting, likely as a result of the

fact that the rupture extended upward through very thick, undeformaed glacial outwash gravels [Van Dissen et al. 2011]. Dolan and Haravitch [2014] systematically analyzed the discrepancy between geological surface displacements and estimates of slip from geodetic slip inversion for six large (M_w = 7.1 to 7.9) strike-slip earthquakes and argued that patterns of near-surface inelastic off-fault deformation are controlled to a large degree by the structural maturity of the fault. They found that ruptures on structurally immature faults are characterized by large SSDs, whereas ruptures along structurally mature faults exhibited much small discrepancies between surface fault slip and slip at depth. As discussed above, we can explain most, and perhaps all, of the apparent shallow slip deficits for the three earthquakes we studied through a combination of three factors: (1) failure to include constraints on near-fault surface deformation patterns in the inversions; (2) failure to incorporate measurements of distributed (i.e., "off-fault") inelastic near-surface deformation in the inversions; and (3) the use of elastic models, which will underestimate near-surface slip. The three earthquakes we study were all generated by structurally immature faults, and thus exhibited large amounts of near-surface inelastic deformation, and commensurately large apparent SSDs. Earthquakes generated by more structurally mature faults exhibit much smaller apparent SSDs [Dolan and Haravitch 2014], and we think that the factors mentioned above will likely be able to account for all of the measured SSDs, although this remains an area that needs to be documented more thoroughly. In summary, based on these various factor, we think that most, and perhaps all, of the shallow slip deficits that have been inferred in the past can be explained by coseismic inelastic behaviors and will be easily compensated interseismically, if there is any.

2.6   Conclusions

We investigated the shallow slip deficit (SSD) of three $M_w > 7$ strike-slip earthquakes using GPS and InSAR observations and optical image correlation of aerial photography and SPOT satellite data. Our synthetic test demonstrated that failure to include data on surface deformation around fault may introduce an artificial shallow slip deficit to elastic half-space models. By exploring the optimal set of the phase unwrapping parameters inside the SNAPHU algorithm, we were able to recover deformation signals that were previously buried in the decorrelated sections of interferograms in the high-deformation zones surrounding the faults. Combining this deformation with additional GPS coverage and near-fault measurements of surface deformation patterns from analysis of optical imagery, we provided a spatially complete constraint on the slip v.s depth patterns. The resulting inversions reveal relatively small apparent shallow slip deficits ranging from 3% to 18%. Although these deficits are much smaller than previous estimates, the left discrepancies need to be explained. We suggest that there are three complementary possible explanations, which are, sample of earthquakes being not large enough, interseismic slip or triggered slip compensation and possibly the artifact from using purely elastic models. The shallow slip deficits that have been apparent in previous comparisons of on-fault geologic are at least partially, and perhaps almost entirely, artifacts of the earlier analyses. Failure to incorporate near-fault surface deformation patterns as a constraint in geodetic inversions, together with a smoothness regularization, can lead to artificial shallow slip deficits that obscure the fact that essentially all slip at depth in large earthquakes likely extends to the surface as a combination of on-fault slip and off-fault distributed deformation.

Appendix

Here we provide the inversion procedure used to estimate slip at depth from a variety of surface observations. The overall approach is to minimize the misfit between the observations and the model subject to positivity and smoothness constraints. The minimization is

$$\min(||Am - b||^2 + \lambda^2||Sm||^2) \tag{2.2}$$

where λ is the smoothness factor that represent how rough the slip distribution is. $Am = b$ together with $Sm = 0$, can be expanded as following

$$\begin{bmatrix} W_pG_p & W_pW_rR_p \\ W_aG_a & W_aW_rR_a \\ W_gG_g & 0 \\ W_oG_o & 0 \\ \lambda S & 0 \end{bmatrix} \begin{bmatrix} m_u \\ m_r \end{bmatrix} = \begin{bmatrix} W_pd_p \\ W_ad_a \\ W_gd_g \\ W_od_o \\ 0 \end{bmatrix} \tag{2.3}$$

Where G are the Green's functions calculated according to [Okada 1992], with 3-components being projected to observation directions for InSAR and GPS data, and to the fault azimuth for optical imagery data. d represent observations, W represent weighs (here are diagonal matrices), R represent orbital error absorbing components, S represent smoothness regularization and m is the model. Subscripts p, a, g and o refer to InSAR phase, InSAR azimuth offset, GPS and optical imagery data, respectively. Subscript r refers to ramp absorbing component and u refers to modeled slip. Other non-linear parameters such as dipping angles are included in the computation of Green's function [Okada 1992].

For the weighs of each dataset, they are the multiplication of two parts, the pre-asigned weigh w_{pre} and the weigh relative to InSAR phase data w_{post}. For InSAR data, w_{pre} is proportional to the square root of the number of points inside a subsampled section (n_i) [Simons, Fialko, and Rivera 2002], which is

$$w^i_{pre} = \frac{n_i^{1/2}}{\sum_{j=1}^{N} n_j^{1/2}} \tag{2.4}$$

where N is the total number of points in each dataset. For GPS and optical imagery data, w_{pre} is inversely proportional to the uncertainty (σ_i) [Simons, Fialko, and Rivera 2002], which is

$$w^i_{pre} = \frac{\sigma_i^{-1}}{\sum_{j=1}^{M} \sigma_j^{-1}} \tag{2.5}$$

where M is the total number of observations in each dataset. The weighs relative to InSAR phase data w_{post} are part of the non-linear parameters we established a comprehensive search for (solutions shown in Figure S2.1).

The orbital ramp components are composed of columns of x, y positions and ones

for representing individual planar ramps for each InSAR acquisition as following.

$$
\begin{bmatrix} R_p \\ R_a \end{bmatrix} =
\begin{bmatrix}
x_1^1 & y_1^1 & 1 & 0 & 0 & 0 & 0 & 0 & 0 & \dots \\
x_2^1 & y_2^1 & 1 & 0 & 0 & 0 & 0 & 0 & 0 & \dots \\
\dots & \dots & \dots & \dots & \dots & \dots & \dots & \dots & \dots & \dots \\
0 & 0 & 0 & x_1^2 & y_1^2 & 1 & 0 & 0 & 0 & \dots \\
0 & 0 & 0 & x_2^2 & y_2^2 & 1 & 0 & 0 & 0 & \dots \\
\dots & \dots & \dots & \dots & \dots & \dots & \dots & \dots & \dots & \dots \\
0 & 0 & 0 & 0 & 0 & 0 & x_1^3 & y_1^3 & 1 & \dots \\
0 & 0 & 0 & 0 & 0 & 0 & x_2^3 & y_2^3 & 1 & \dots \\
\dots & \dots & \dots & \dots & \dots & \dots & \dots & \dots & \dots & \dots
\end{bmatrix}
\qquad (2.6)
$$

where x and y represent east position and north position. In x_j^i, i and j refer jth point in ith acquisition. After the inversion, each ramp signal can be estimated as $r_j^i = a_i x_j^i + b_i y^i + c_i$, where a_i, b_i and c_i are parameters in m_r. Also, in order to get a robust solution for both the ramp and the slip model, we began the inversion with a relatively high ramp weigh (W_r). After removing this initial ramp from the data, we assign a smaller weigh (W_r) so as to remove any remaining residual ramp while not affecting the solution of the slip.

Since we assumed the faults having both strike and dip slip during the earthquakes, the model is represented as

$$
\begin{bmatrix} m_u \\ m_r \end{bmatrix} = \left(s_1^s, s_1^d, s_2^s, s_2^d, \dots \dots s_N^s, s_N^d, \ a_1, b_1, c_1, \dots \dots a_M, b_M, c_M \right)^T
\qquad (2.7)
$$

where s_i^s and s_i^d represent strike and dip slip for the ith patch, and a_i, b_i and c_i are ramp

parameters for the *i*th InSAR acquisition. *N* is the total number of patches in a model, and *M* is the total number of InSAR acquisitions used in the inversion.

The first difference smoothness matrix is given by

$$
S = \begin{bmatrix}
\cdots & \cdots & \cdots & \cdots & \cdots & \cdots \\
\cdots & -1/r_{ij} & \cdots & 1/r_{ij} & \cdots & \cdots \\
\cdots & \cdots & -1/r_{ij} & \cdots & 1/r_{ij} & \cdots \\
\cdots & \cdots & \cdots & \cdots & \cdots & \cdots
\end{bmatrix}
\tag{2.8}
$$

where *i* and *j* are indexes of two adjacent patches and *r* represent the distance between the two patches. Note that the smoothness are the same for dip and strike slip.

The optimization for non-linear parameters is done by systematically searching the parameter space with one parameter at time. The search exits when no parameter change can provide a 0.1% smaller overall least-square residual between the model and the data. A series of large-scale initial states are tested in order to avoid the solution from falling into local minima. The Green's functions are re-computed when the fault geometry changes.

Acknowledgements

Chapter 2, in full, is a reprint of the material as it appears in Geophysical Journal International: Xu, X., Tong, X., Sandwell, D.T., Milliner, C.W., Dolan, J.F., Hollingsworth, J., Leprince, S. and Ayoub, F., 2016, "Refining the shallow slip deficit", *Geophysical Journal International*, 204(3), pp.1867-1886. The dissertation author is the primary investigator and author of this paper.

References

Agnew, D. C., Owen, S., Shen, Z.-K., Anderson, G., Svarc, J., Johnson, H., Austin, K. E., and Reilinger, R. (2002). "Coseismic displacements from the Hector Mine, California, earthquake: Results from survey-mode Global Positioning System measurements". In: *Bulletin of the Seismological Society of America* 92.4, pp. 1355–1364.

Ayoub, F., Leprince, S., and Avouac, J.-P. (2009). "Co-registration and correlation of aerial photographs for ground deformation measurements". In: *ISPRS Journal of Photogrammetry and Remote Sensing* 64.6, pp. 551–560.

Bock, Y., Agnew, D. C., Fang, P., Genrich, J. F., Hager, B. H., Herring, T. A., Hudnut, K. W., King, R. W., Larsen, S., Minster, J.-B., Stark, K., Wdowinski, S., and Wyatt, F. (1993). "Detection of crustal deformation from the Landers earthquake sequence using continuous geodetic measurements". In: *Nature* 361.6410, pp. 337–340.

Brune, J. N. and Anooshehpoor, A. (1998). "A physical model of the effect of a shallow weak layer on strong ground motion for strike-slip ruptures". In: *Bulletin of the Seismological Society of America* 88.4, pp. 1070–1078.

Chen, C. W. and Zebker, H. A. (2001). "Two-dimensional phase unwrapping with use of statistical models for cost functions in nonlinear optimization". In: *JOSA A* 18.2, pp. 338–351.

Dolan, J. F. and Haravitch, B. D. (2014). "How well do surface slip measurements track slip at depth in large strike-slip earthquakes? The importance of fault structural maturity in controlling on-fault slip versus off-fault surface deformation". In: *Earth and Planetary Science Letters* 388, pp. 38–47.

Dziewonski, A., Chou, T.-A., and Woodhouse, J. (1981). "Determination of earthquake source parameters from waveform data for studies of global and regional seismicity". In: *Journal of Geophysical Research: Solid Earth* 86.B4, pp. 2825–2852.

Fialko, Y. (2004). "Probing the mechanical properties of seismically active crust with space geodesy: Study of the coseismic deformation due to the 1992 Mw7. 3 Landers (southern California) earthquake". In: *Journal of Geophysical Research: Solid Earth (1978–2012)* 109.B3.

Fialko, Y., Simons, M., and Agnew, D. (2001). "The complete (3-D) surface displacement field in the epicentral area of the 1999 Mw7. 1 Hector Mine earthquake, California, from space geodetic observations". In: *Geophysical Research Letters* 28.16, pp. 3063–3066.

Fialko, Y., Sandwell, D., Simons, M., and Rosen, P. (2005). "Three-dimensional deformation caused by the Bam, Iran, earthquake and the origin of shallow slip deficit". In: *Nature* 435.7040, pp. 295–299.

Fialko, Y., A., G., Sylvain, G.-G.J.J. B., Leprince, S., Sandwell, D. T., and Agnew, D. C. (2010). "Static Rupture Model of the 2010 M7.2 El Mayor-Cucapah Earthquake from ALOS, ENVISAT, SPOT and GPS Data". In: *AGU Fall Meeting*.

Hollingsworth, J, Dolan, J., Milliner, C., Leprince, S, Ayoub, F, and Avouac, J (2012). "Analysis of the shallow slip deficit using sub-pixel image correlation: implications for fault slip rates, and seismic hazards". In: *AGU Fall Meeting Abstracts*. Vol. 1, p. 02.

Huang, Y. and Van Genderen, J. (1997). "Comparison of several multi-look processing procedures in INSAR processing for ERS-1&2 tandem mode". In: *ERS SAR Interferometry*. Vol. 406, p. 215.

Jónsson, S., Zebker, H., Segall, P., and Amelung, F. (2002). "Fault slip distribution of the 1999 Mw 7.1 Hector Mine, California, earthquake, estimated from satellite radar and GPS measurements". In: *Bulletin of the Seismological Society of America* 92.4, pp. 1377–1389.

Kaneko, Y and Fialko, Y. (2011). "Shallow slip deficit due to large strike-slip earthquakes in dynamic rupture simulations with elasto-plastic off-fault response". In: *Geophysical Journal International* 186.3, pp. 1389–1403.

Kaneko, Y, Hamling, I., Van Dissen, R., Motagh, M, and Samsonov, S. (2015). "InSAR imaging of displacement on flexural-slip faults triggered by the 2013 Mw 6.6 Lake Grassmere earthquake, central New Zealand". In: *Geophysical Research Letters* 42.3, pp. 781–788.

King, G. C. and Wesnousky, S. G. (2007). "Scaling of fault parameters for continental strike-slip earthquakes". In: *Bulletin of the Seismological Society of America* 97.6, pp. 1833–1840.

Leprince, S., Barbot, S., Ayoub, F., and Avouac, J.-P. (2007). "Automatic and precise orthorectification, coregistration, and subpixel correlation of satellite images, application to ground deformation measurements". In: *Geoscience and Remote Sensing, IEEE Transactions on* 45.6, pp. 1529–1558.

Massonnet, D., Rossi, M., Carmona, C., Adragna, F., Peltzer, G., Feigl, K., and Rabaute, T. (1993). "The displacement field of the Landers earthquake mapped by radar interferometry". In: *Nature* 364.6433, pp. 138–142.

Massonnet, D., Feigl, K., Rossi, M., and Adragna, F. (1994). "Radar interferometric mapping of deformation in the year after the Landers earthquake". In: *Nature* 369.6477, pp. 227–230.

Michel, R. and Avouac, J.-P. (2006). "Coseismic surface deformation from air photos: The Kickapoo step over in the 1992 Landers rupture". In: *Journal of Geophysical Research: Solid Earth (1978–2012)* 111.B3.

Milliner, C. W., Dolan, J. F., Hollingsworth, J., Leprince, S., Ayoub, F., and Sammis, C. (2015). "Quantifying near-field and off-fault deformation patterns of the 1992 Mw 7.3 Landers earthquake". In: *Geochemistry, Geophysics, Geosystems*.

Okada, Y. (1992). "Internal deformation due to shear and tensile faults in a half-space". In: *Bulletin of the Seismological Society of America* 82.2, pp. 1018–1040.

Pitarka, A., Dalguer, L. A., Day, S. M., Somerville, P. G., and Dan, K. (2009). "Numerical study of ground-motion differences between buried-rupturing and surface-rupturing earthquakes". In: *Bulletin of the Seismological Society of America* 99.3, pp. 1521–1537.

Reid, H. F. and Lawson, A. C. (1910). *The California Earthquake of April 18, 1906: Report of the State Earthquake Investigation Commission; in Two Volumes and Atlas. The Mechanics of the Earthquake*. Carnegie Institute of Washington.

Rice, J. R. and Tse, S. T. (1986). "Dynamic motion of a single degree of freedom system following a rate and state dependent friction law". In: *Journal of Geophysical Research: Solid Earth (1978–2012)* 91.B1, pp. 521–530.

Rockwell, T. K., Lindvall, S., Dawson, T., Langridge, R., Lettis, W., and Klinger, Y. (2002). "Lateral offsets on surveyed cultural features resulting from the 1999 Izmit and Düzce earthquakes, Turkey". In: *Bulletin of the Seismological Society of America* 92.1, pp. 79–94.

Sandwell, D. T. and Price, E. J. (1998). "Phase gradient approach to stacking interferograms". In: *Journal of Geophysical Research: Solid Earth (1978–2012)* 103.B12, pp. 30183–30204.

Simons, M and Rosen, P. (2007). "Interferometric synthetic aperture radar geodesy". In: *Treatise on Geophysics*.

Simons, M., Fialko, Y., and Rivera, L. (2002). "Coseismic deformation from the 1999 Mw 7.1 Hector Mine, California, earthquake as inferred from InSAR and GPS observations". In: *Bulletin of the Seismological Society of America* 92.4, pp. 1390–1402.

Tong, X., Sandwell, D. T., and Fialko, Y. (2010). "Coseismic slip model of the 2008 Wenchuan earthquake derived from joint inversion of interferometric synthetic aperture radar, GPS, and field data". In: *Journal of Geophysical Research: Solid Earth (1978–2012)* 115.B4.

Treiman, J. A., Kendrick, K. J., Bryant, W. A., Rockwell, T. K., and McGill, S. F. (2002). "Primary surface rupture associated with the mw 7.1 16 october 1999 hector mine earthquake, san bernardino county, california". In: *Bulletin of the Seismological Society of America* 92.4, pp. 1171–1191.

Tse, S. T. and Rice, J. R. (1986). "Crustal earthquake instability in relation to the depth variation of frictional slip properties". In: *Journal of Geophysical Research: Solid Earth (1978–2012)* 91.B9, pp. 9452–9472.

Van Dissen, R, Barrell, D, Litchfield, N, Villamor, P, Quigley, M, King, A, Furlong, K, Begg, J, Townsend, D, Mackenzie, H, Stahl, T, Noble, D, Duffy, B, Bilderback, E, Claridge, J, Klahn, A, Jongens, R, Cox, S, Langridge, R, Ries, W, Dhakal, R, Smith, A, Horblow, S, Nicol, R, Pedley, K, Henham, H, Hunter, R, Zajac, A, and Mote, T. (2011). "Surface rupture displacement on the Greendale Fault during the Mw 7.1 Darfield (Canterbury) earthquake, New Zealand, and its impact on manmadestructures." In: *Journal of Geophysical Research: Solid Earth (1978–2012)*.

Wei, M., Sandwell, D., and Fialko, Y. (2009). "A silent Mw 4.7 slip event of October 2006 on the Superstition Hills fault, southern California". In: *Journal of Geophysical Research: Solid Earth* 114.B7.

Zebker, H. A., Rosen, P. A., Goldstein, R. M., Gabriel, A., and Werner, C. L. (1994). "On the derivation of coseismic displacement fields using differential radar interfer-

ometry: The Landers earthquake". In: *Journal of Geophysical Research: Solid Earth (1978–2012)* 99.B10, pp. 19617–19634.

Zhang, H., Thurber, C., and Bedrosian, P. (2009). "Joint inversion for vp, vs, and vp/vs at SAFOD, Parkfield, California". In: *Geochemistry, Geophysics, Geosystems* 10.11.

Tables and Figures

Table 2.1: **InSAR data acquisitions used for 3 major strike-slip earthquakes in Baja-California.**

Earthquake	Satellite	Track	Master Acquisition Date	Repeat Acquisition Date	B_P (m)
Landers 1992/06/24	ERS1	399 D	1992/04/24	1992/07/03	-344.63
		349 A	1992/05/26	1992/06/30	356.90
Hector Mine 1999/10/16	ERS2	127 D	1998/09/15	1998/10/20	-16.05
		77 A	1999/11/12	1999/11/21	59.88
El-Mayor Cucapah 2010/04/04	ENVISAT	77 A	2010/02/21	2010/03/28	-75.12
		306 A	2010/03/09	2010/04/13	244.39
		84 D	2010/03/28	2010/05/02	-87.98
	ALOS	211 A	2010/01/15	2010/04/17	617.13
		212 A	2009/12/17	2010/05/04	909.90
		532 D	2008/02/08	2010/05/16	-205.87
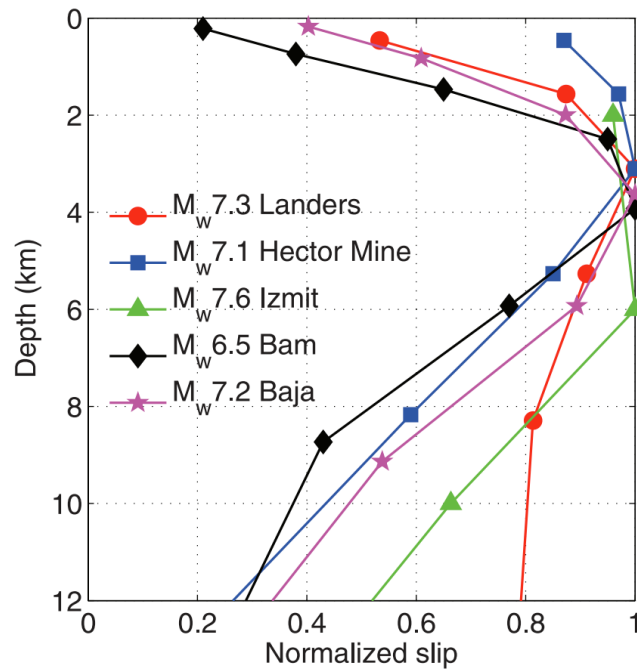
Figure 2.1: **Distribution of cumulative coseismic slip for several large** ($M_w > 7$) **strike slip earthquakes** [Fialko 2004; Kaneko and Fialko 2011]. The cumulative coseismic slip is computed by integrating the strike slip along strike. Horizontal axis represents normalized cumulative strike slip.
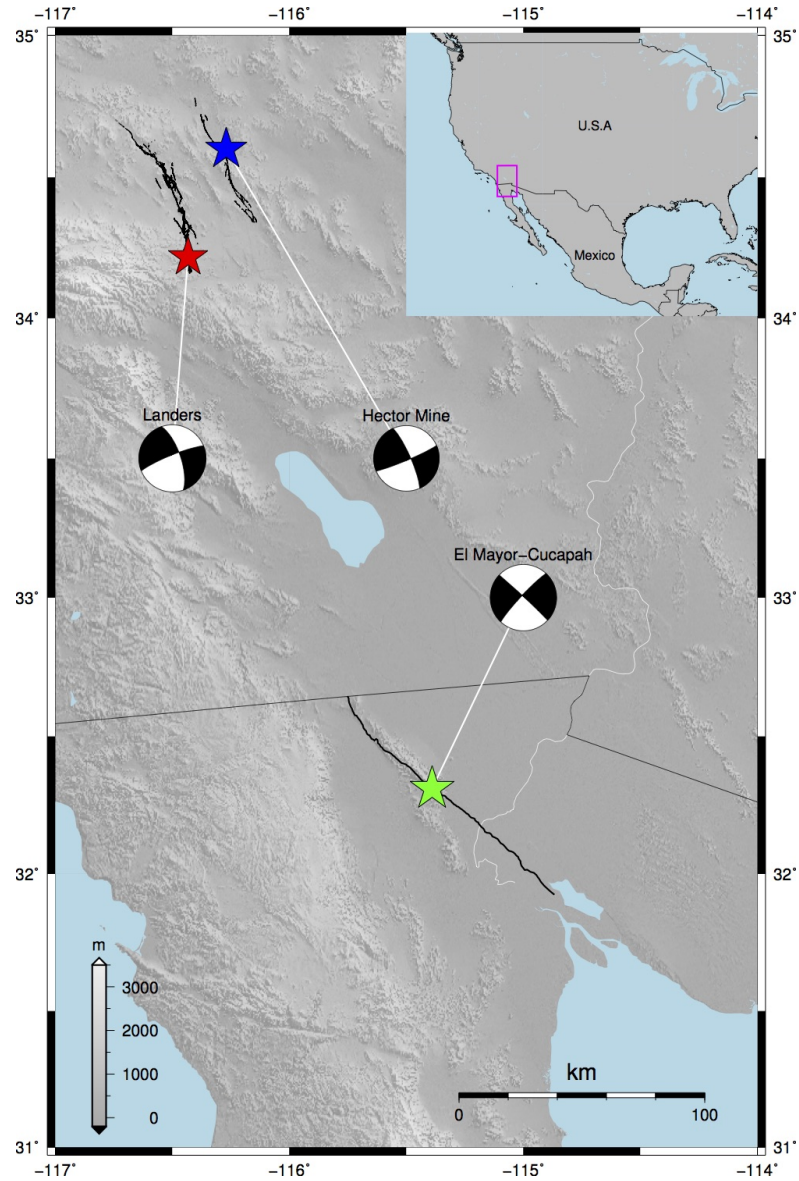
Figure 2.2: **Tectonic setting of the three major strike-slip earthquakes in southern California and Baja-California.** Stars represent epicenters of earthquakes, with beach balls denote the centroid moment tensor solutions (http://www.globalcmt.org).

(a)

(b)

(c)

(d)

(e)

(f)
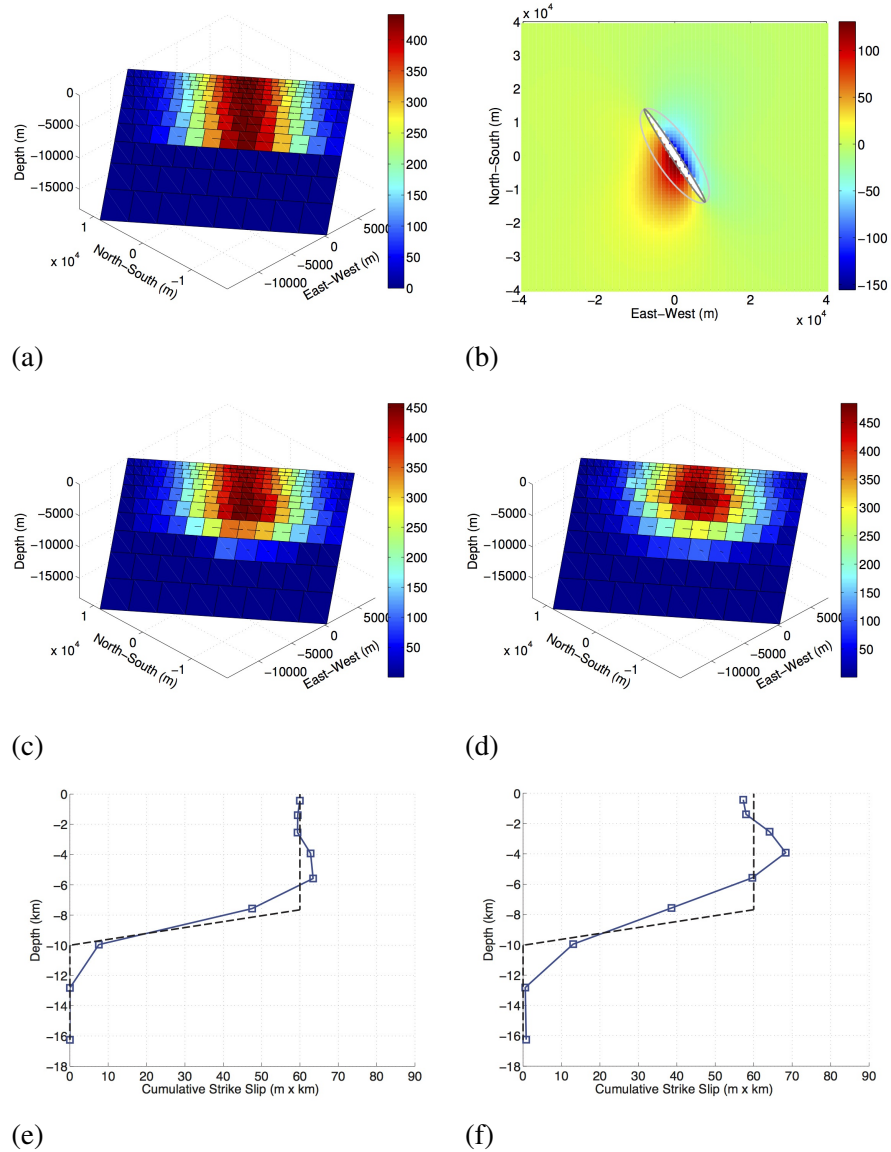
Figure 2.3: **Synthetic test showing shallow slip deficit caused by missing near-fault data**. a) is the input model and b) is the surface observations along North-South direction (part of the synthetic data used) generated from input slip model with different amount of missing data close to fault. Dark grey ellipse represents the thin mask used and light grey ellipse represents the wide mask used. c) and d) are inversion results from data in b) with 2% local noise being added; c) corresponds to inversion with thin data mask while d) corresponds to wide data mask. The color represents strike slip and the arrows represent total slip for each patch. e) and f) are cumulative strike slip v.s. depth for model c) and d), and the dash line represents the cumulative strike slip v.s. depth for the input model.
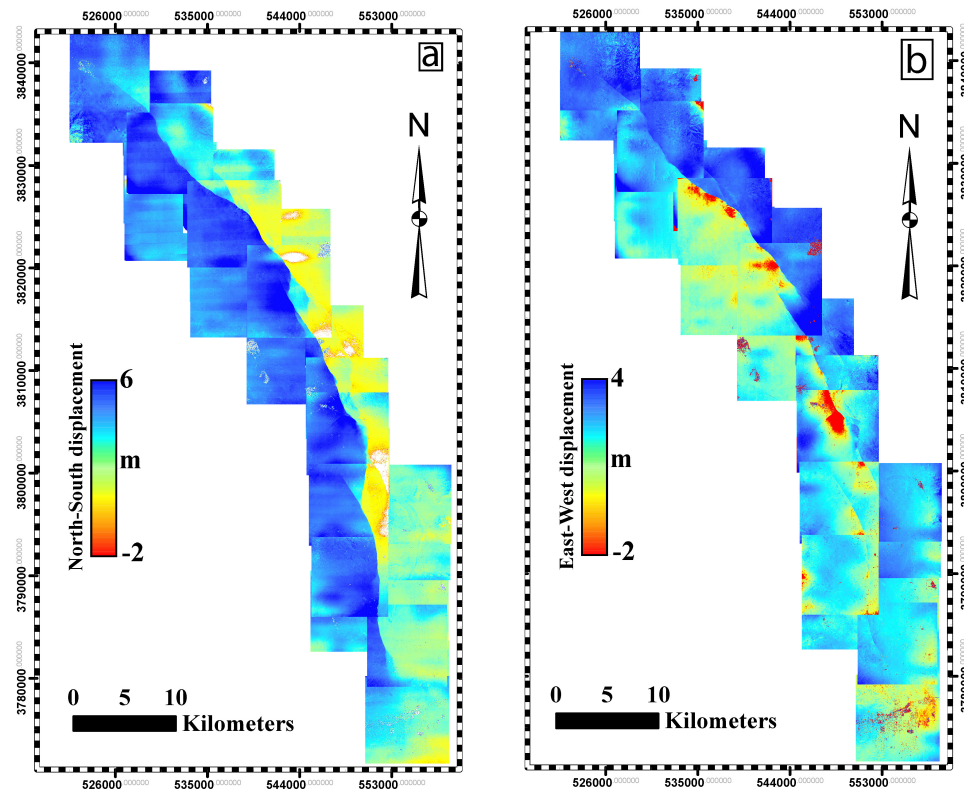
Figure 2.4: **COSI-Corr processed aerial image from National Aerial Photography Program (NAPP) of the 1992 Landers rupture**. On the left is the North-South component of the surface deformation and on the right is the East-West component.

(a)   (b)
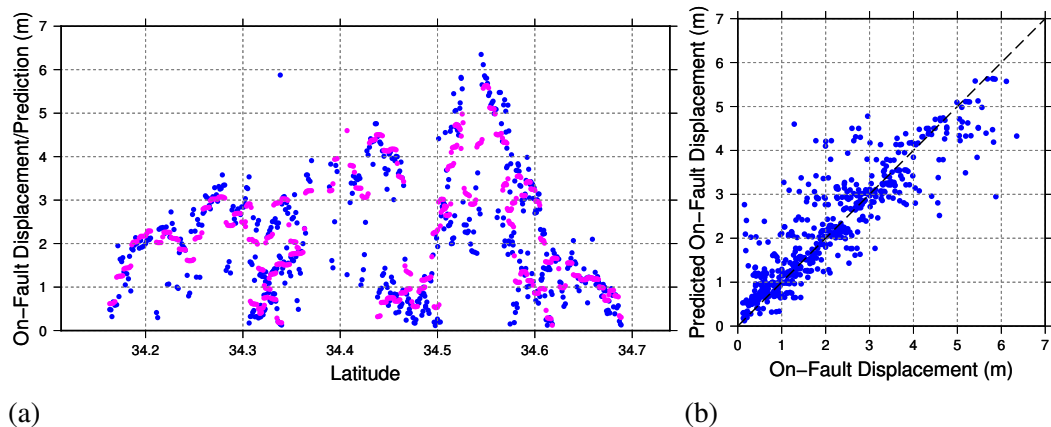
Figure 2.5: **Fault offset from NAPP image COSI-corr and prediction from our model for the 1992 Landers earthquake**. a) Blue dots being estimation from NAPP image, magenta dots are predicted offset at the same position on fault from our best-fitting model. b) Comparison between fault offset and model prediction.
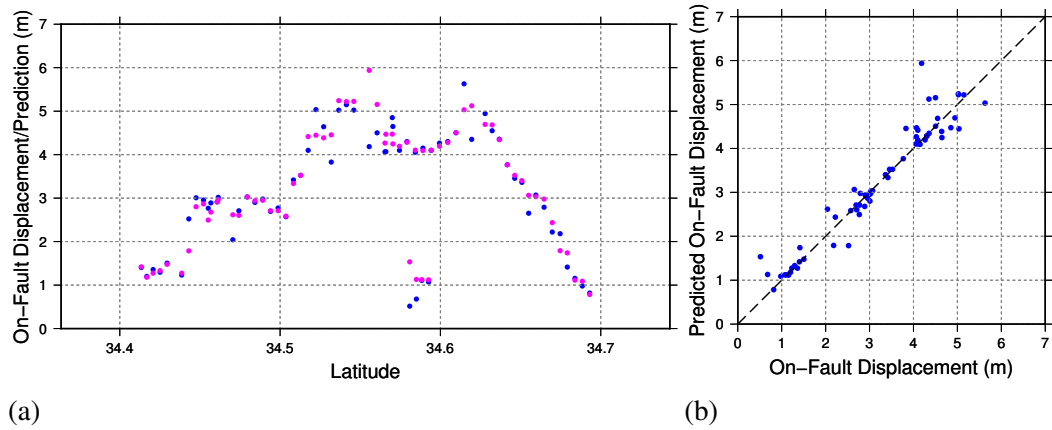
Figure 2.6: **Fault offset from NAPP image COSI-corr and prediction from our model for the 1999 Hector Mine earthquake**. a) Blue dots being estimation from NAPP image, magenta dots are predicted fault offset at the same position on fault from our best-fitting model. b) Comparison between fault offset and model prediction.
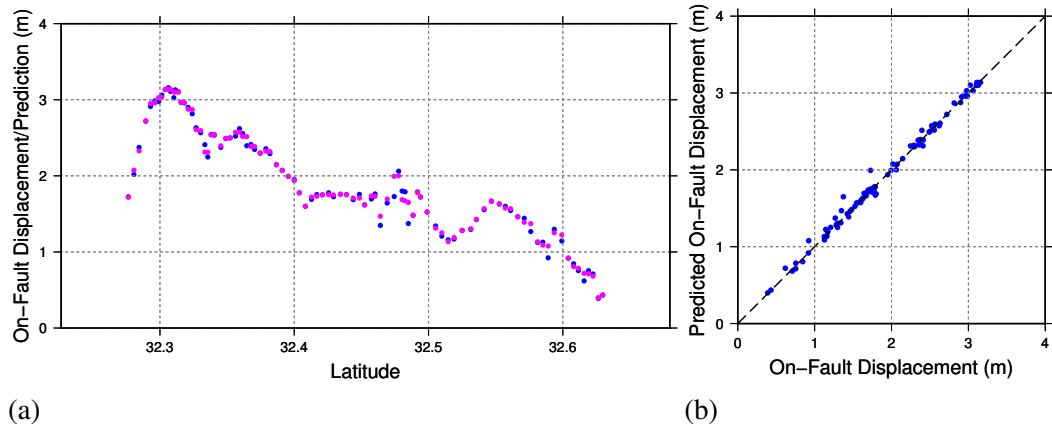
Figure 2.7: **Fault offset from SPOT image COSI-corr and prediction from our model for the 2010 El Mayor-Cucapah earthquake**. a) Blue dots being estimation from SOPT image, magenta dots are predicted fault offset at the same position on fault from our best-fitting model. b) Comparison between fault offset and model prediction.

(a)

(b)

(c)
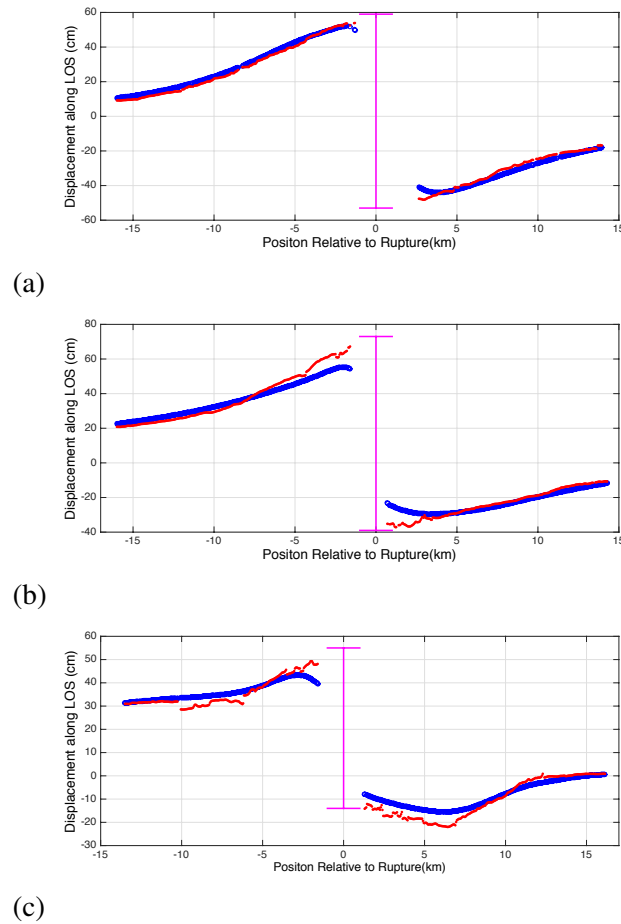
Figure 2.8: **Comparison between previous model [Fialko 2004] prediction and our new unwrapped LOS displacement for the 1992 Landers earthquake**. The blue circles are model prediction from previous study, and the red dots are new unwrapped displacement field. The vertical magenta line is the estimated fault offset being placed at the fault position. The gap in between are segments being masked due to its low unwrapping reliability.
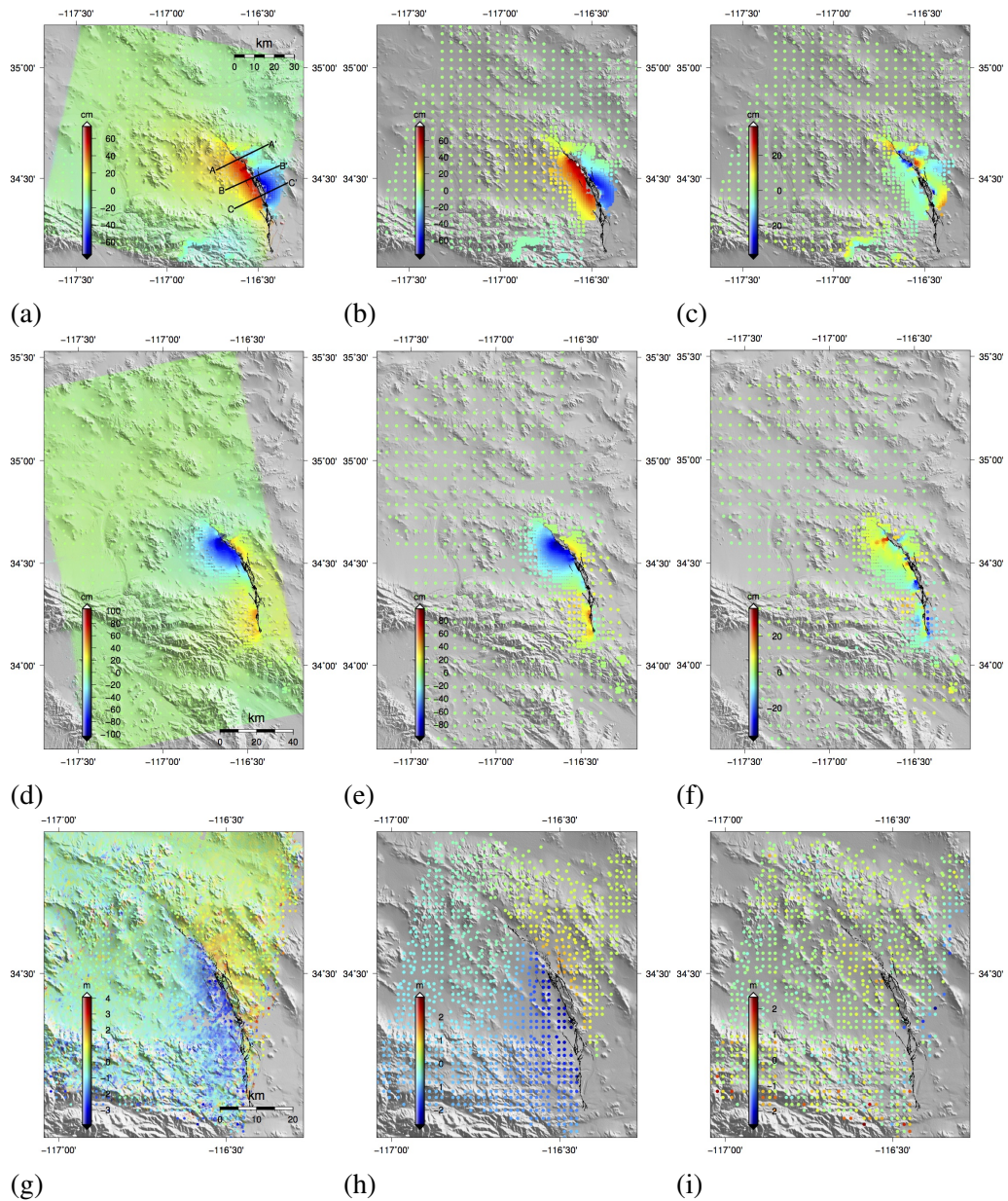
Figure 2.9: **Processed InSAR data, our model prediction and the residual after moving model from data for the 1992 Landers earthquake**. a), d) and g) are InSAR unwrapped displacement field from descending track 399, ascending track 349 and the azimuth offset from descending track 399, respectively. b), e) and h) are corresponding model prediction at subsampled data points from a), d) and g), with c), f) and i) being the residuals from fitting.
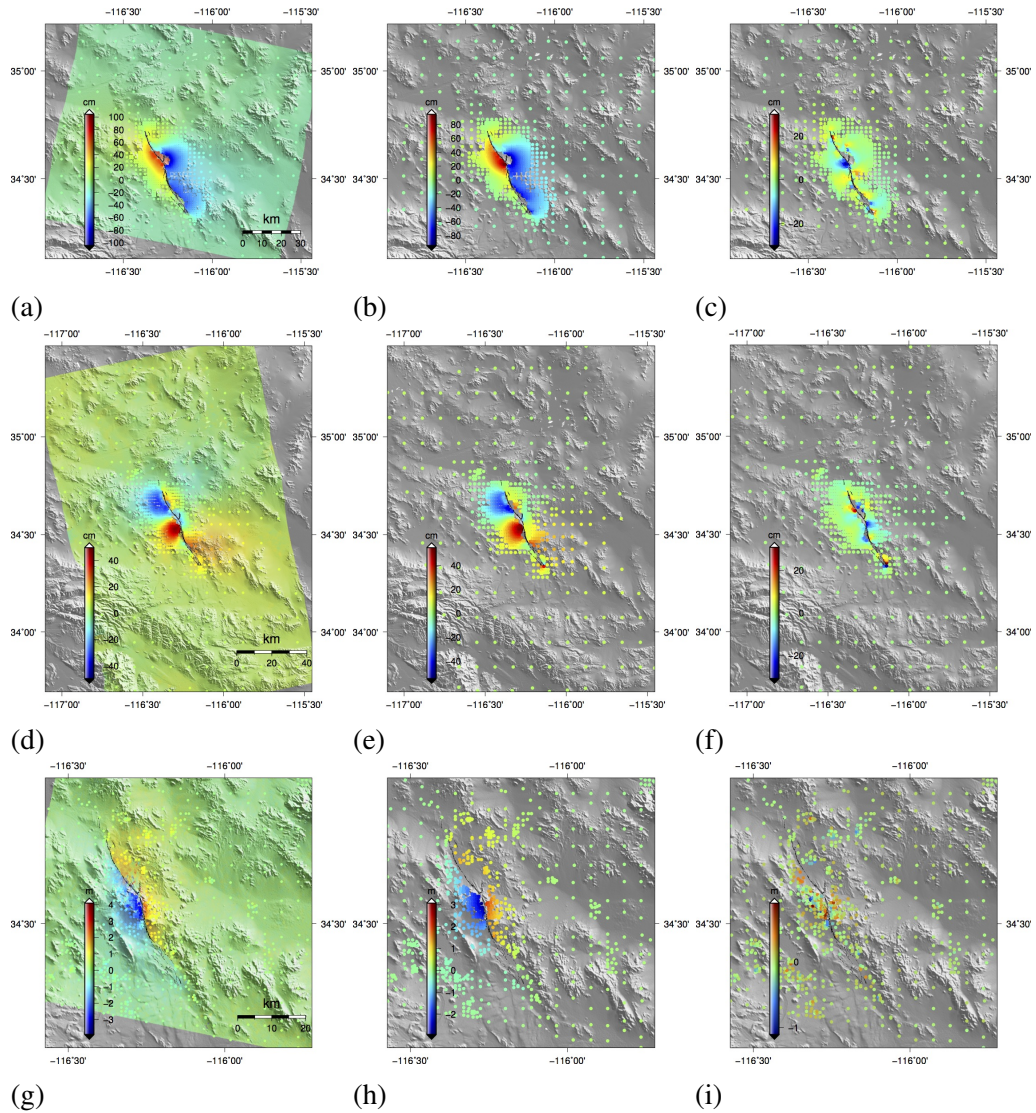
Figure 2.10: **Processed InSAR data, our model prediction and the residual after moving model from data for 1999 Hector Mine earthquake**. a), d) and g) are InSAR unwrapped displacement field from descending track 127, ascending track 77 and the azimuth offset from descending track 127, respectively. b), e) and h) are corresponding model prediction at subsampled data points from a), d) and g), with c), f) and i) being the residuals from fitting.

(a)   (b)   (c)

(d)   (e)   (f)

(g)   (h)   (i)
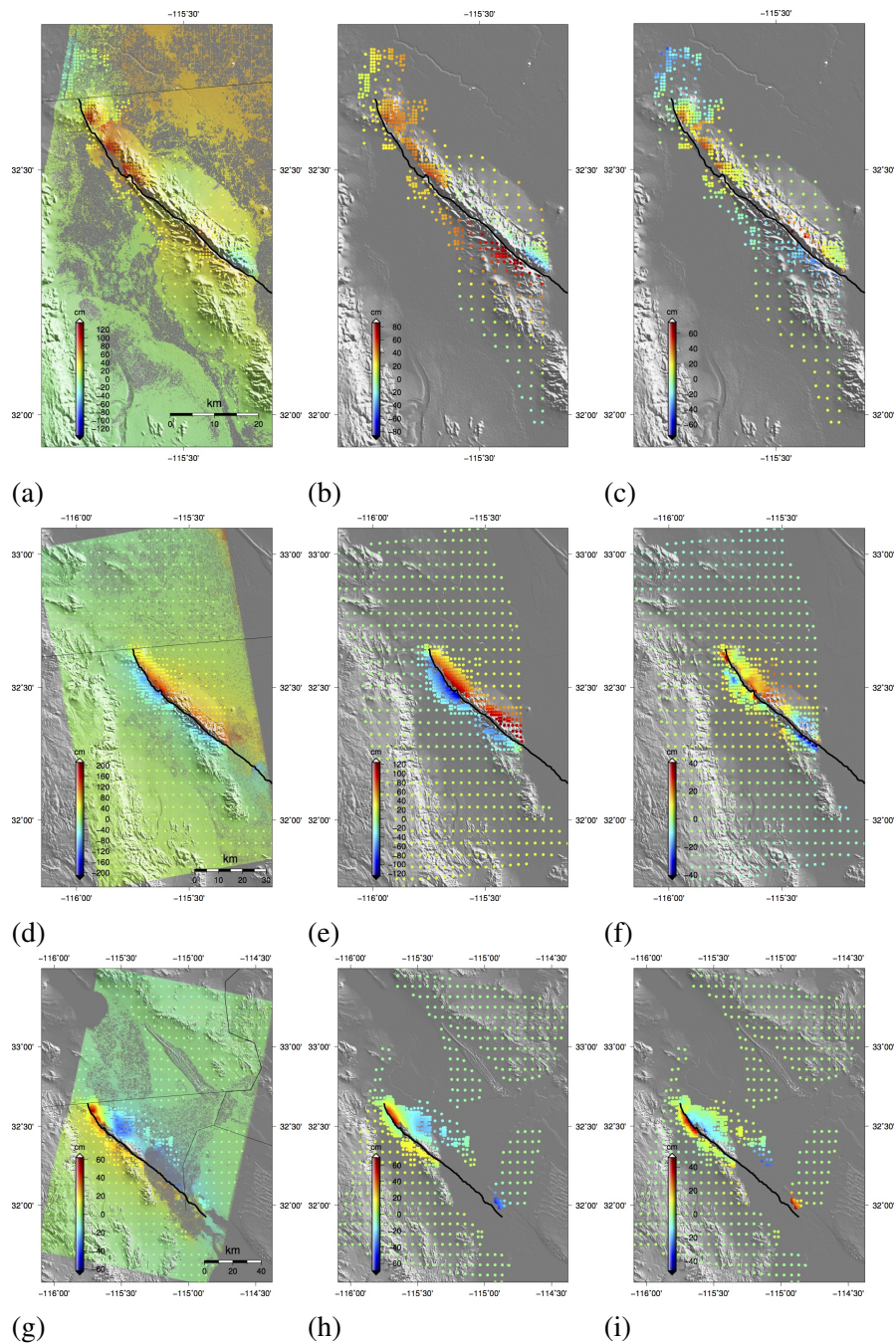
Figure 2.11: **Processed InSAR data, our model prediction and the residual after moving model from data for 2010 El Mayor-Cucapah earthquake**. a), d), g), j), m) and p) are InSAR unwrapped displacement field from ALOS descending track 532, ascending track 212, ENVISAT descending track 84, ascending track 77, ascending track 306 and the azimuth offset from ALOS ascending track 212 and 211. b), e), h), k), n) and q) are corresponding model prediction at subsampled data points from a), d), g), j), m) and p), with c), f), i), l), o) and r) being the residuals from fitting, respectively.
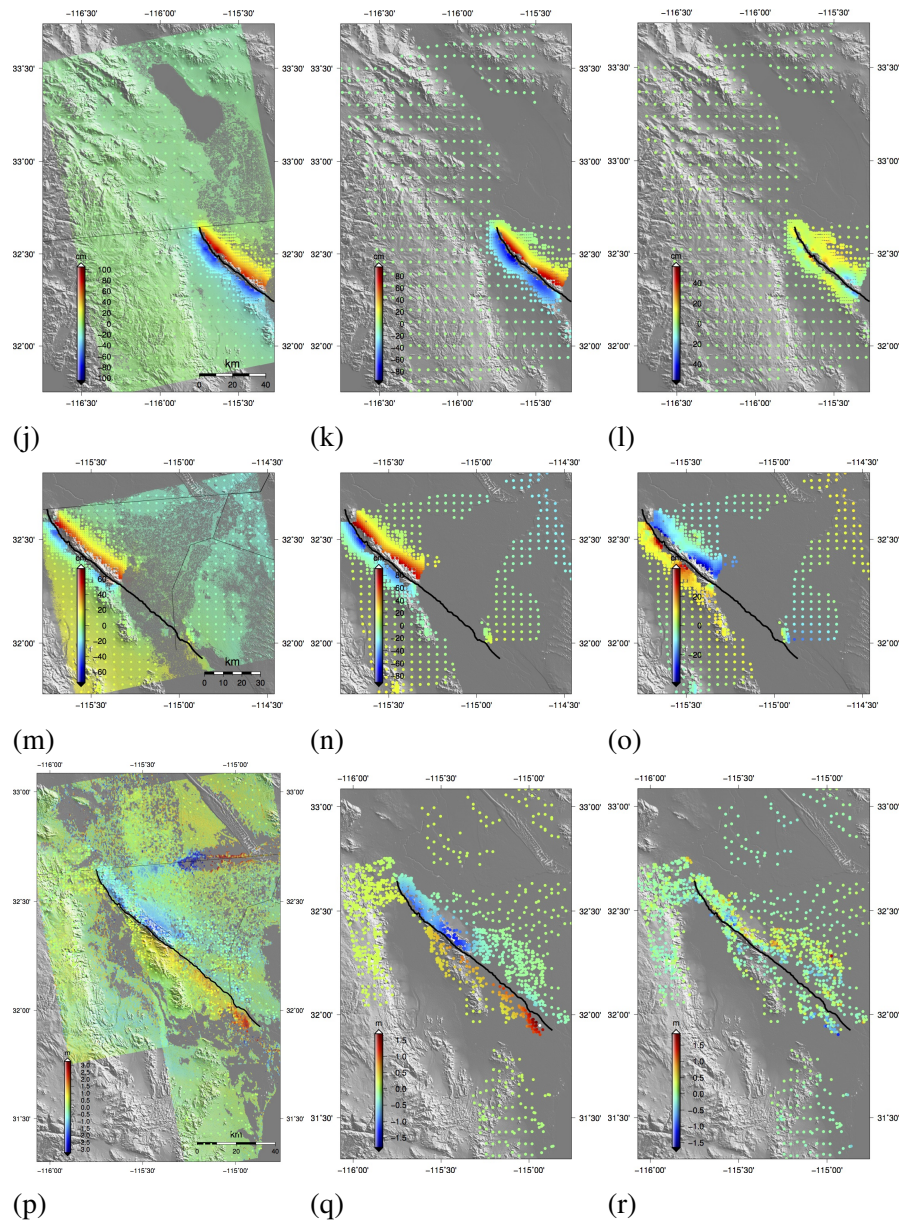
(j)   (k)   (l)

(m)   (n)   (o)

(p)   (q)   (r)

Figure 2.11: Processed InSAR data, our model prediction and the residual after moving model from data for 2010 El Mayor-Cucapah earthquake, continued.
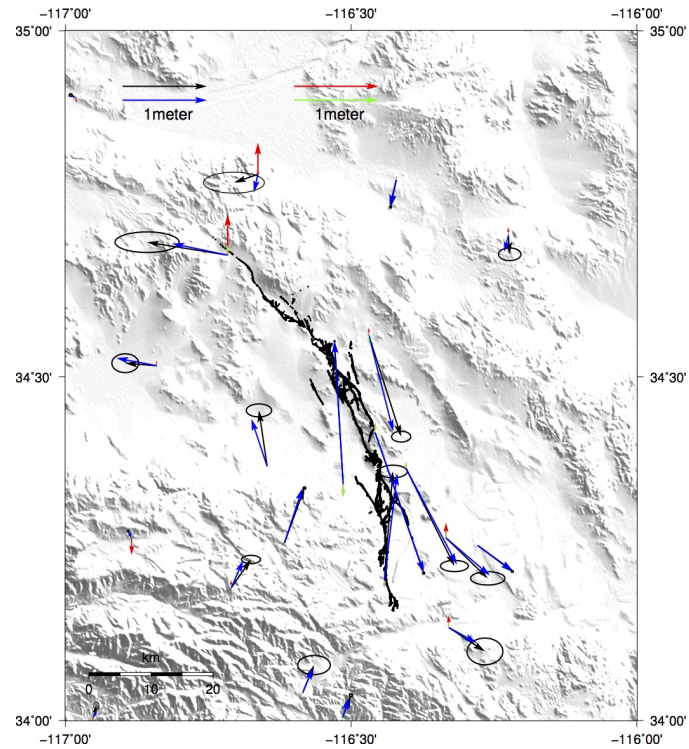
Figure 2.12: **GPS measurements from 82 stations and the forwarded displacement at these stations for 1992 Landers earthquake**. Black and red arrows represent horizontal and vertical measurements from GPS, and blue and green arrows are forwarded horizontal and vertical displacements from our model. Only near field stations are plotted.
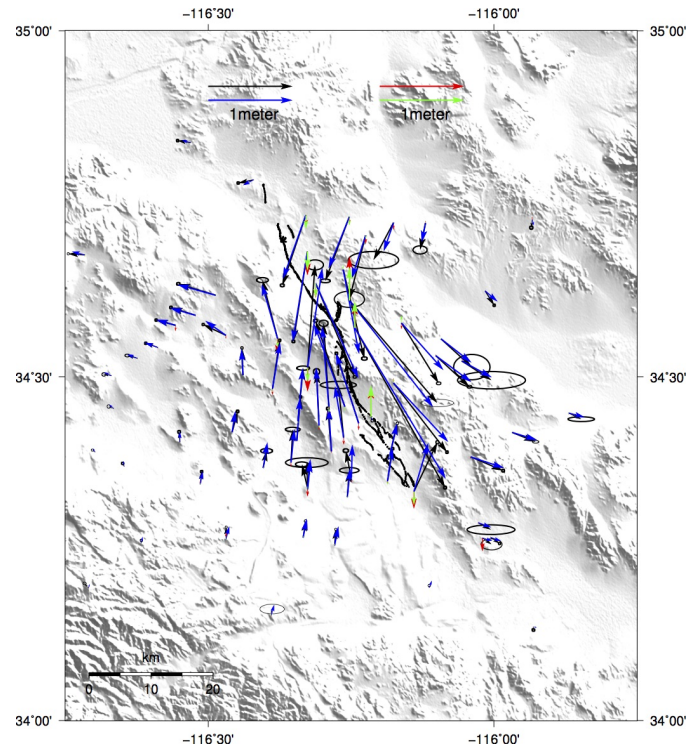
Figure 2.13: **GPS measurements from 77 stations and the forwarded displacement at these stations for 1999 Hector Mine earthquake**. Black and red arrows represent horizontal and vertical measurements from GPS, and blue and green arrows are forwarded horizontal and vertical displacements from our model. Only near field stations are plotted.
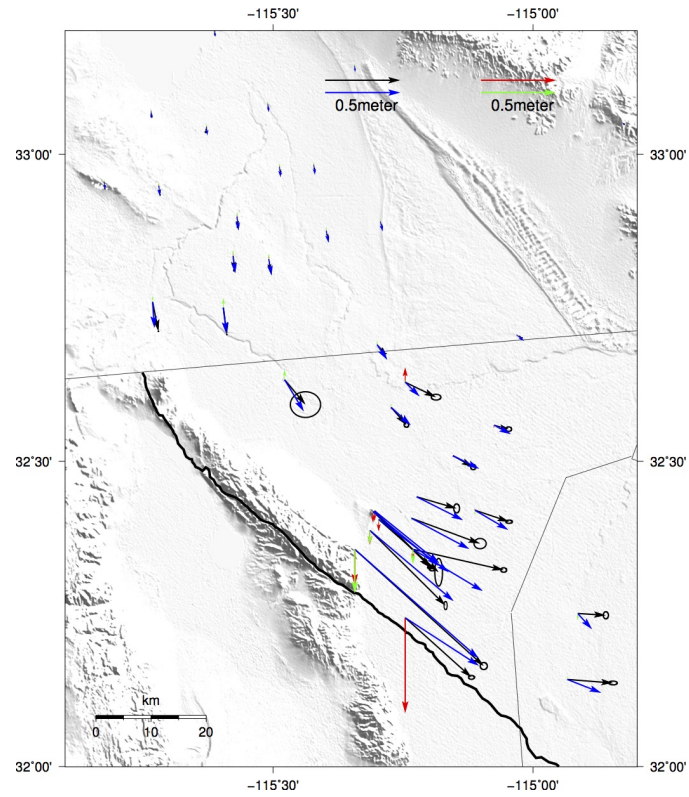
Figure 2.14: **GPS measurements from 158 stations and the forwarded displacement at these stations for 2010 El Mayor-Cucapah earthquake**. Black and red arrows represent horizontal and vertical measurements from GPS, and blue and green arrows are forwarded horizontal and vertical displacements from our model. Only near field stations are plotted.
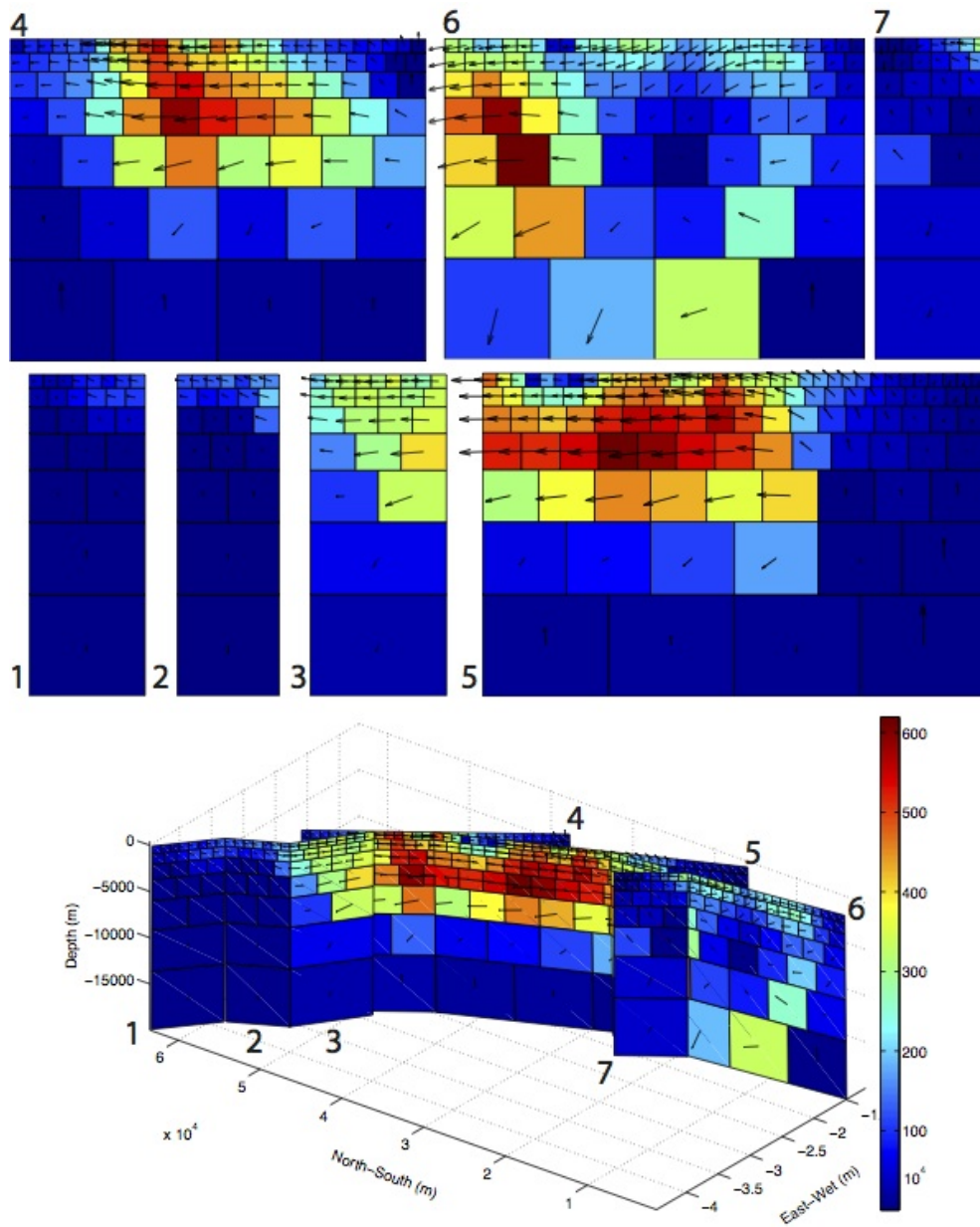
Figure 2.15: **Slip distribution from InSAR-GPS-Arial Image joint inversion for 1992 Landers earthquake with a elastic half space model**. Colors represents strike slip while arrows stand for total slip and the direction.
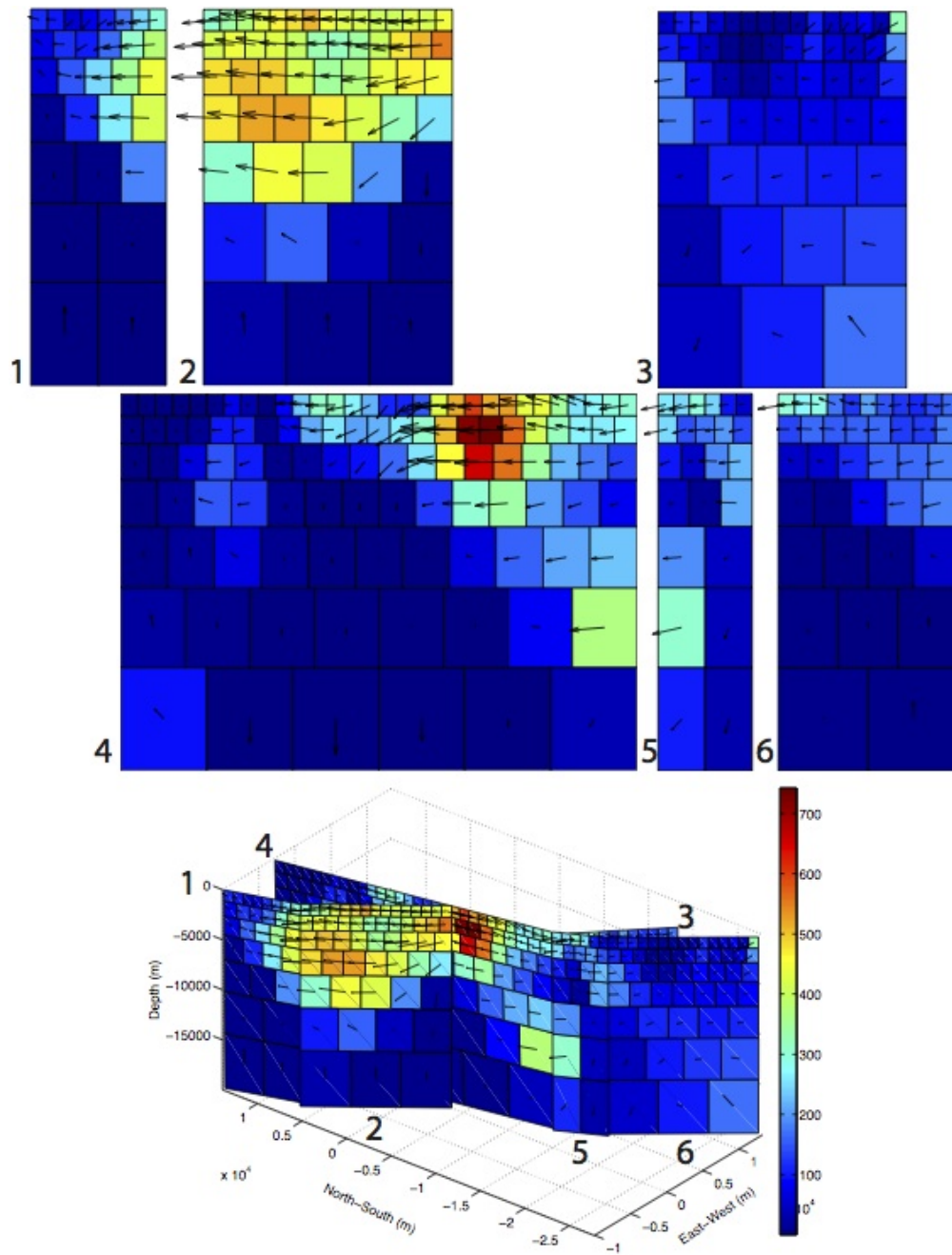
Figure 2.16: **Slip distribution from InSAR-GPS-Arial Image joint inversion for 1999 Hector Mine earthquake with a elastic half space model**. Colors represents strike slip while arrows stand for total slip and the direction.
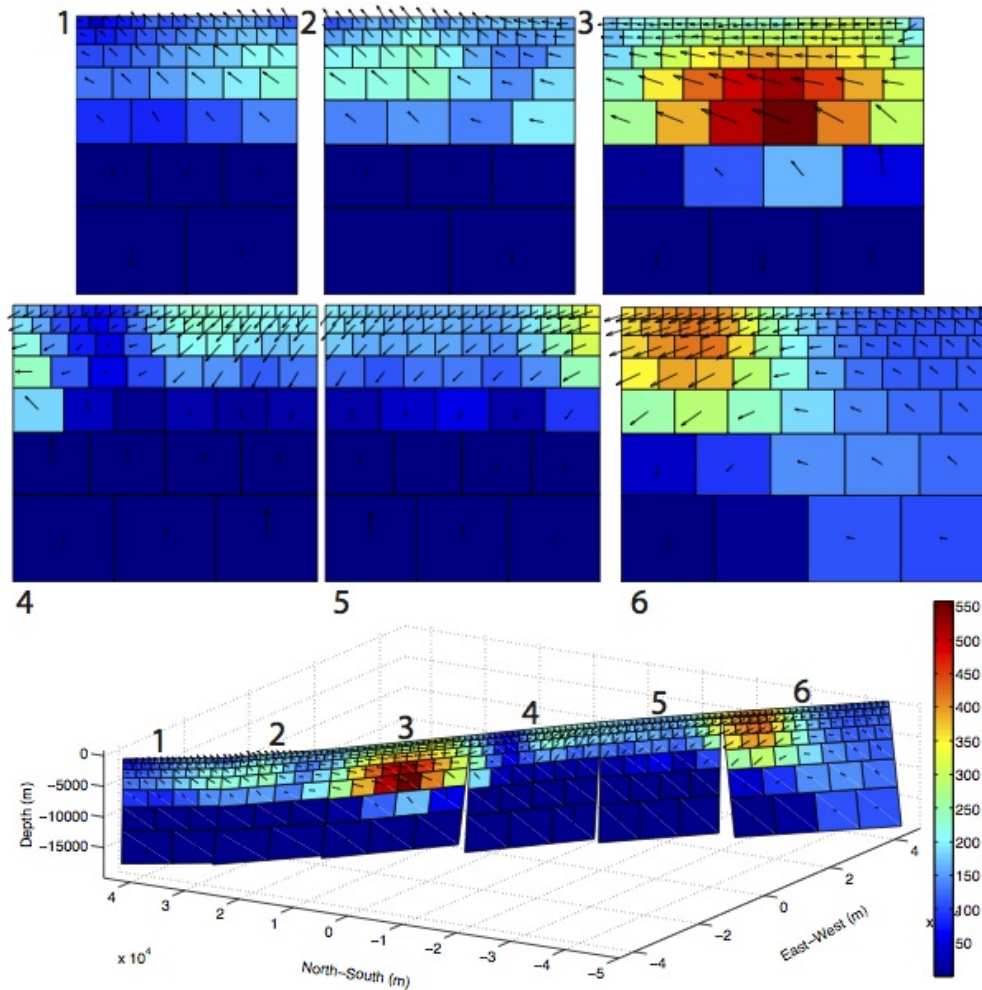
Figure 2.17: **Slip distribution from InSAR-GPS-Satellite Image joint inversion for 2010 El Mayor-Cucapah earthquake with a elastic half space model**. Colors represents strike slip while arrows stand for total slip and the direction.
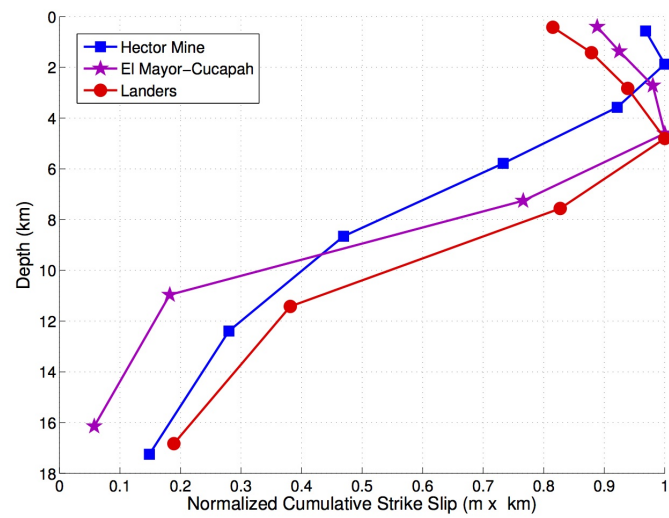
Figure 2.18: **Normalized cumulative strike slip versus depth for 3 large strike slip earthquakes, from new inversion results**. Cumulative strike slip is computed by integrating the strike slip along fault trace. The results are normalized by the maximum amount of cumulative strike slip.

Supplements
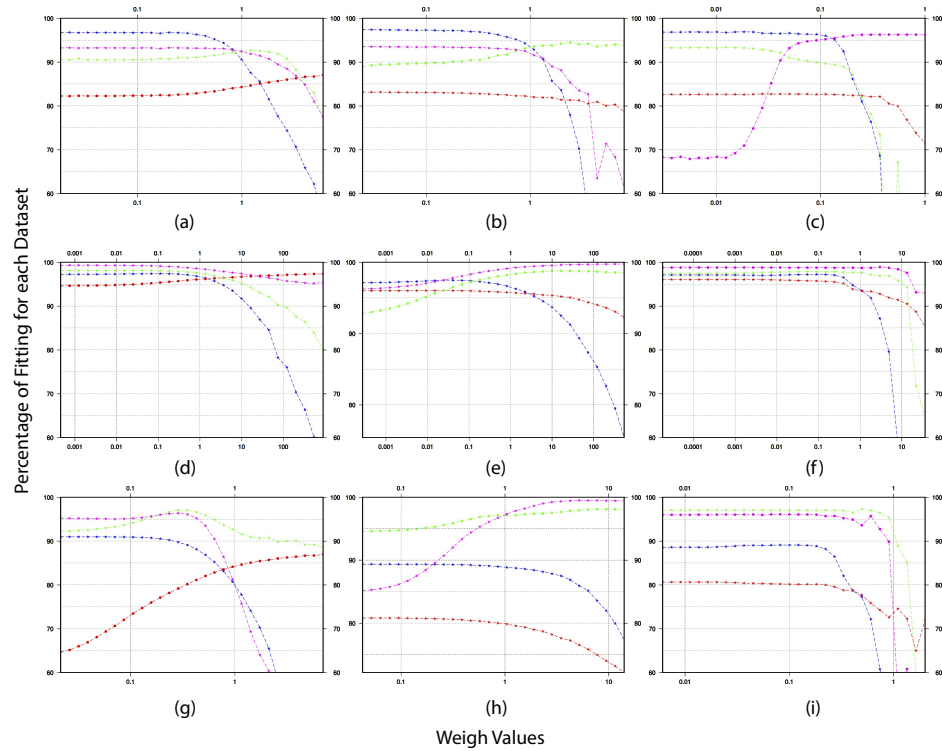
Figure S2.1: **Cross-sections in model space along weigh directions versus percentage of recovery**. Horizontal axes for (a) (b) and (c) represents weighs of azimuth offset, GPS observations and fault offset estimates from SPOT image, for the inversion of 1992 Landers earthquake, while weigh for InSAR phase data is defined as 1. Similarly, (d), (e) and (f) are weighs of the datasets for 1999 Hector Mine earthquake and (g), (h) and (i) for 2012 El Myaor-Cucapah earthquake. In all the plots above, blue line represents the recovery for InSAR phase data, red line for InSAR azimuth offset data, green line for the recovery of GPS data and magenta line for the recovery of estimated fault offset from aerial image. Gray dash lines represents the selection of the weigh values.
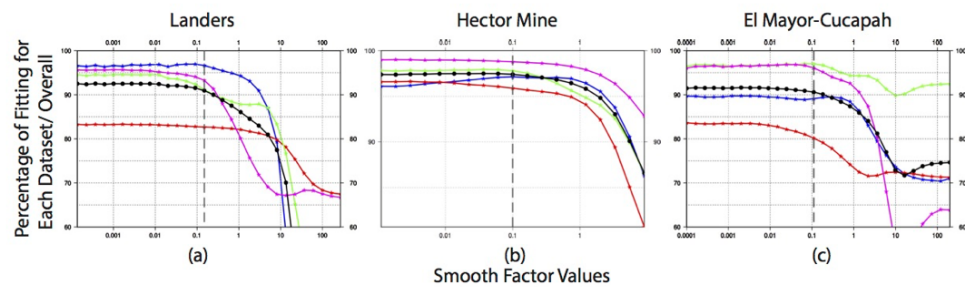
Figure S2.2: **Percentage of recovery for each dataset versus smooth factor in each inversion.** (a) 1992 Landers, (b) 1999 Hector Mine, (c) 2010 El Mayor-Cucapah. In all the plots above, blue line represents the recovery of InSAR phase data, red line for the recovery InSAR azimuth offset data, green line for the recovery of GPS data, magenta line for the recovery of estimated fault offset from aerial image and black line represents the mean recovery of these four data sets. Gray dash lines represent the selection of smooth factor for each earthquake.
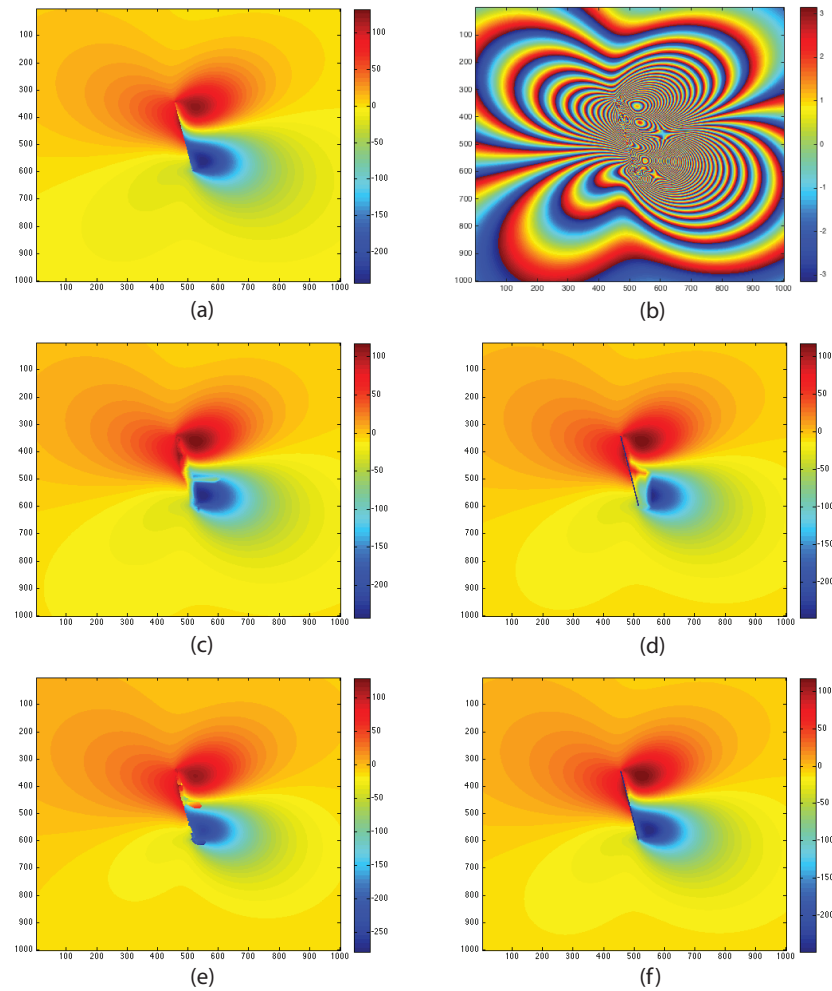
Figure S2.3: **How to correctly unwrap a deformation field with a rupture inside.** (a) is the true deformation field in radiant (phase). (b) is the wrapped phase, i.e. the synthetic interferogram. (c) is the directly unwrapped phase using SNAPHU with default settings. (d) is the unwrapped phase with a correlation mask right on the rupture. (e) is unwrapped phase with assuming a maximum discontinuity being approximately 400 radiant. (f) is unwrapped phase with combing methods in (d) and (e), i.e. assuming an approximate maximum discontinuity and setting a correlation mask on fault.

(a)

(b)

(c)
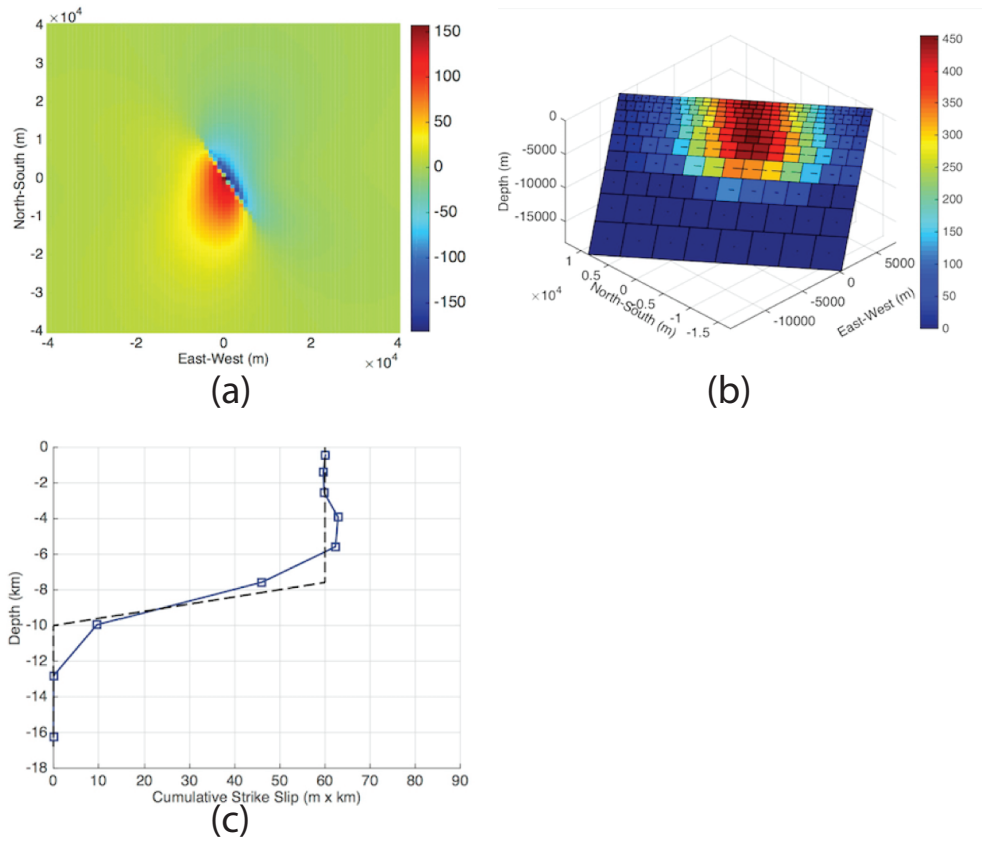
Figure S2.4: **Synthetic test of inversion with full data coverage.** (a) is the North component of the deformation field with assumed slip in Figure 3(a). (b) is the recovered slip from inversion with 2% local noise added. (c) is the cumulative strike slip v.s. depth with the dash line being the input slip from Figure 3(a).
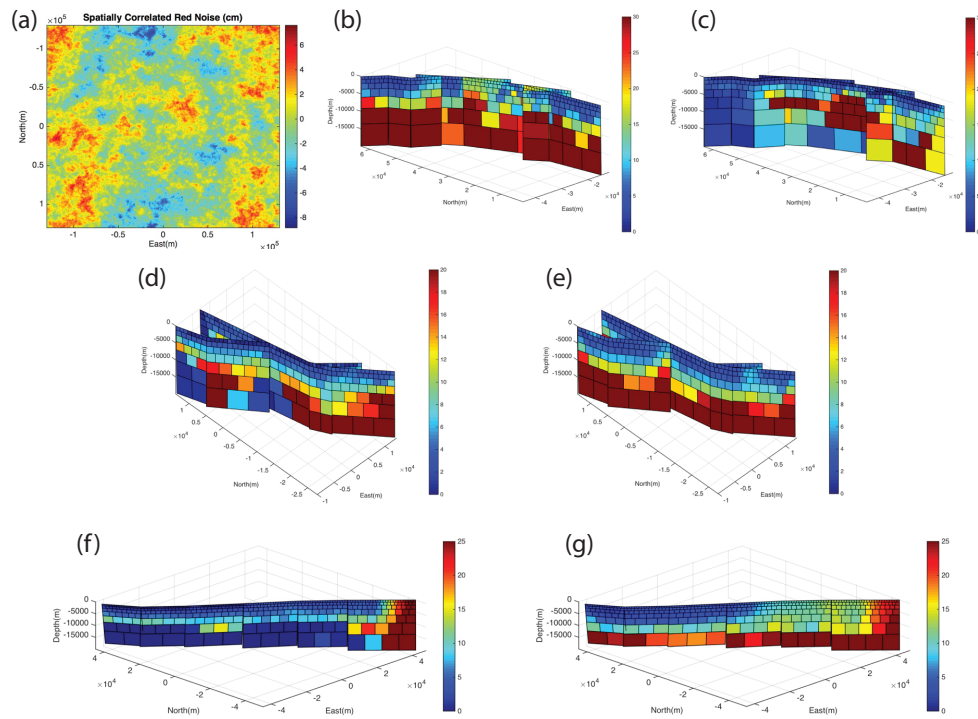
Figure S2.5: **Monte Carlo simulation for testing the model's uncertainty by perturbing the data with spatially correlated red noise** (1000 realizations). (a) is an example of the red noise generated for each InSAR scene during each realization. (b) and (c) are the strike-slip and dip-slip uncertainty for the 1992 Landers earthquake in cm. (d) and (e) are the strike-slip and dip-slip uncertainty for the 1999 Hector Mine earthquake in cm. (f) and (g) are the strike-slip and dip-slip uncertainty for the 2010 El Mayor-Cucapah earthquake in cm.

Chapter 3

A Spectral Expansion Approach for Geodetic Slip Inversion: Implications for the Down-dip Rupture Limits of Oceanic and Continental Megathrust Earthquakes

We have developed a data-driven spectral expansion inversion method to place bounds on the down-dip rupture depth of large megathrust earthquakes having good InSAR and GPS coverage. This inverse theory approach is used to establish the set of models that are consistent with the observations. In addition, the inverse theory method demonstrates that the spatial resolution of the slip models depends on two factors, the spatial coverage and accuracy of the surface deformation measurements, and the slip depth. Application of this method to the 2010 Mw 8.8 Maule Earthquake shows a slip maximum at 19 km depth tapering to zero at ∼40 km depth. In contrast, the continent-continent megathrust earthquakes of the Himalayas, e.g. 2015 Mw 7.8 Gorkha Earthquake, shows a slip maximum at 9 km depth tapering to zero at ∼18 km depth.

The main question is why is the maximum slip depth of the continental megathrust earthquake only 50% of that observed in oceanic megathrust earthquakes. To understand this difference, we have developed a simple 1-D heat conduction model that includes the effects of uplift and surface erosion. The relatively low erosion rates above the ocean megathrust results in a geotherm where the 450°-600°C transition is centered at ∼40 km depth. In contrast, the relatively high average erosion rates in the Himalayas of ∼1 mm/yr results in a geotherm where the 450°-600°C transition is centered at ∼20 km. Based on these new observations and models, we suggest that the effect of erosion rate on temperature explains the difference in the maximum depth of the seismogenic zone between Chile and the Himalayas.

3.1   Introduction

Over the past few decades, advances in space geodesy such as Interferometric Synthetic Aperture Radar (InSAR) and Global Positioning System (GPS) have facilitated detailed mapping of surface deformation. These high quality and regional datasets have enabled scientists to build 3-D deformation fields for many large earthquakes. Usually, the fault geometry can be reasonably approximated from aftershocks, geophysical imaging, and geological field studies. Elastic models that relate slip at depth to surface deformation can then be constructed by discretizing this fault into small patches before estimating the slip on each patch. While this method is straightforward, it hardly provides an estimate of the spatial resolution nor unbiased uncertainties associated with the slip model. It is well known that the equations which relate slip at depth to surface deformation contain an upward continuation term [Steketee 1958], which exponentially attenuates the rupture signal at wavelengths smaller than the depth, therefore making this inverse problem inherently non-unique [Parker 1994]. This is true even if the data coverage is complete

and the data have no errors. The non-uniqueness becomes evident in parameterized inversions when the discretized patch size is smaller than the depth; the inversions are poorly conditioned resulting in wild oscillations in slip distribution. In order to stabilize the solution, smoothness regularization combined with a non-negativity constraint is applied to the inversion, which acts as a strong prior knowledge to the model [Jónsson et al. 2002; Simons, Fialko, and Rivera 2002; Fialko 2004; Tarantola 2005]. In some studies, a checkerboard test is used to illustrate the resolving power of the data [Fialko 2004; Tong, Sandwell, and Fialko 2010]. [Tong, Sandwell, and Fialko 2010] performed this test for the Mw 8.8 2010 Maule earthquake and found the model can only recover a 20-km checker up to about 35km depth, but can recover a 40-km checker to 60km depth. These results are consistent with the inverse relation between model resolvability and rupture depth.

For several recent megathrust earthquakes, surface deformation has been well recorded and many studies have incorporated these data into earthquake rupture inversions using the standard parameter estimation approach. Inversions for the 2010 Mw 8.8 Maule earthquake (oceanic plate subducting) suggest a tapering of slip toward zero at ∼40 km depth [Tong, Sandwell, and Fialko 2010; Lorito et al. 2011]. This depth is similar to many other oceanic subduction slip inversions (e.g. the 2011 Mw 9.0 Tohoku-oki [Simons et al. 2011; Minson et al. 2014]; 2004 Mw 9.2 Sumatra-Andaman [Ammon et al. 2005; Lay et al. 2005; Chlieh et al. 2007]. By contrast, inversions for the 2015 Mw 7.8 Nepal earthquake (continental plate subducting) suggest a tapering of slip toward zero at less than 20 km [Wang and Fialko 2015; Galetzka et al. 2015]. This depth is consistent with the maximum depth of strong interseismic coupling resolved by geodetic models along the Himalayan front [Stevens and Avouac 2015]. This difference raises two questions. First, is the difference in down-dip rupture limit well resolved by the

observations? If it is well resolved, what physical mechanisms may explain such a large difference? This requires a real uncertainty estimate as well as an analysis of resolving power for inversion models.

To address the first question, we adopt the approach of linear inverse theory [Gilbert 1971; Parker 1977]. As noted by Parker [1977]: "The quality that distinguishes inverse theory from the parameter estimation problem of statistics is the unknowns are functions, not merely a handful of real numbers. This means that the solution contains in principle an infinite number of variables, and therefore with real data the problem is as underdetermined as it can be." The approach begins with the well-known Green's functions relating slip at depth on a prescribed fault plane to surface deformation. Following the spectral expansion method, we then construct a set of up to N orthonormal slip functions that span the set of N surface observations. The solution and its uncertainty are constructed from a finite number $M \leq N$ of these functions, or kernels, that match the data to within their uncertainty. The low order kernels are generally smoothest and well constrained by the data while the higher order kernels have more oscillations and are more poorly constrained. The solution is constructed from the well-resolved kernels. We use this approach to provide bounds on the depth distribution of slip during the Mw 8.8 Maule (oceanic) and Mw 7.8 Gorka (continental) megathrust areas, and show that the factor-of-two difference in slip depth is indeed well resolved by the geodetic data.

To address the second question, the pronounced difference in the slip depth, we develop a simple 1-D thermal model that includes the effects of vertical advection of heat due to erosion-induced rebound [Royden 1993]. We find that an erosion rate of 1 mm/yr decreases the depth of the 600°C isotherm by a factor of two, which can explain the relatively shallow rupture depth of the Gorka earthquake.

3.2 The spectral expansion approach

Here we give a brief summary of the spectral expansion theory from Parker [1977; 1994] as applied to static slip inversion. The theory is originally from Gilbert [1971]. The main difference between our formulation and the original formulation is that our model is 2-D vector slip (strike and dip) as a function of the two dimensions on the fault surface Note that the fault does not need to be a planar surface. The data are surface deformation sampled at a finite number of points on the surface of the Earth. GPS can provide 3 components of deformation while InSAR provides 1 or 2 line of sight components. Each component of each data point is and has an uncertainty . We use the elastic half-space Green's function [Okada 1985] to relate vector slip at depth to each component of surface deformation. We note that Green's functions for a more complicated elastic structure could be used. The convolution of the model and the Green's function is given by

$$d_i = \int_\Sigma G_i(\boldsymbol{x})\boldsymbol{m}(\boldsymbol{x})d\Sigma \tag{3.1}$$

where Σ represents integration over the entire fault plane. After dividing both sides of Equation 3.1 by the uncertainty the equation can be re-written as

$$d_i' = \int_\Sigma G_i'(\boldsymbol{x})\boldsymbol{m}(\boldsymbol{x})d\Sigma \tag{3.2}$$

Now the data d_i' as well as the Green's functions G_i' are dimensionless and the data have unit standard deviation. Following Parker [1977] we form the Gram matrix Γ

$$\Gamma_{ij} = \int_\Sigma G_i'(\boldsymbol{x})G_j'(\boldsymbol{x})d\Sigma \tag{3.3}$$

Thus, $\mathbf{\Gamma}$ is positive-definite and symmetric, and can be diagonalized with an orthonormal matrix $\mathbf{O}$ of eigenvectors

$$\mathbf{O}^T \mathbf{\Gamma} \mathbf{O} = \mathbf{\Lambda} \text{ , where } \mathbf{\Lambda} = \text{diag}\{\lambda_1, \lambda_2, \ldots, \lambda_N\} \text{ and } \lambda_1 \geq \lambda_2 \geq \cdots \geq \lambda_N > 0 \quad (3.4)$$

where λ_is are the eigenvalues; the full set of eigenvalues is called the spectrum. It's not difficult to show that

$$\lambda_i = O_i^T \mathbf{\Gamma} O_i = \sum_j O_{ji} \int_\Sigma \mathbf{G}\mathbf{G}^T d\Sigma O_{ij} = \int_\Sigma \sum_j O_{ji} \mathbf{G}\mathbf{G}^T O_{ij} d\Sigma \quad (3.5)$$

where $\mathbf{G}$ is a column vector of normalized Green's functions and the Gram matrix $\mathbf{\Gamma}$ can be treated as a dyad matrix. We rewrite the equation as following

$$\mathbf{\Lambda} = \int_\Sigma \mathbf{O}^T \mathbf{G}\mathbf{G}^T \mathbf{O} d\Sigma \quad (3.6)$$

Now consider the kernel functions defined by

$$\psi_i(\boldsymbol{x}) = \lambda_i^{-1/2} \sum_j O_{ji} G_j'(\boldsymbol{x}) \quad (3.7)$$

It can be easily verified from the equation 3.6 that $\psi_i(\boldsymbol{x})$ are an orthonormal set

$$\int_\Sigma \psi_i(\boldsymbol{x})\psi_j(\boldsymbol{x})d\Sigma = \delta_{ij} \quad (3.8)$$

Therefore, we consider the expansion of the model $\boldsymbol{m}(\boldsymbol{x})$ in terms of these kernels

$$\boldsymbol{m}(\boldsymbol{x}) = \sum_i a_i \psi_i(\boldsymbol{x}) + \psi^* \quad (3.9)$$

where ψ^* is the annihilator (i.e., models that produce no surface deformation at the positions of the data points). The coefficients of the expansion can be derived

$$
\begin{aligned}
a_i &= \int_\Sigma \psi_i(\boldsymbol{x})\boldsymbol{m}(\boldsymbol{x})d\Sigma \\
&= \int_\Sigma \lambda_i^{-1/2} \sum_j O_{ji} G'_j(\boldsymbol{x})\boldsymbol{m}(\boldsymbol{x})d\Sigma \\
&= \lambda_i^{-1/2} \sum_j O_{ji} \int_\Sigma G'_j(\boldsymbol{x})\boldsymbol{m}(\boldsymbol{x})d\Sigma \\
&= \lambda_i^{-1/2} \sum_j O_{ji} d'_j
\end{aligned}
\tag{3.10}
$$

Since all the d'_j have unit variance and the matrix $\boldsymbol{O}$ is orthonormal, the error estimates of a_i are simply and are statistically independent. When the inverse problem is handled with this approach, it is easy to isolate the parts that are better determined, i.e. those have smaller error or larger eigenvalue.

3.3 Application to 2-D and 3-D test cases

We first test this approach using an infinitely-long vertical strike-slip fault. Two input slip distributions are used for testing. The first is uniform slip (1 m) with depth between the surface and 12 km (Figure 3.1c, black dashed line). The second is a Gaussian-shaped slip centered at 8 km depth (Figure 3.1d, black dashed line). We then use the 2-D half-space Green's function [Cohen 1999] to forward generate surface observations from -50km to 50km distance with 200m sampling increment and add a random noise of 2% of the maximum shear deformation [Fialko 2004]. Next, we normalize the Green's function, compute the Gram matrix analytically and decompose it to get the eigenvalues (Figure 3.1a) as well as the orthonormal kernels (Figure 3.1b). Note that the orthonormal kernels have oscillations as a function of depth with more oscillations for higher kernel

number. After this step, we calculate the coefficient for each kernel and combine them to get the inverted slip (Figure 3.1c, blue line). The uncertainty of the inverted slip can be acquired by propagating the error of each coefficient to the model (Figure 3.1c, magenta dash-dotted line).

An additional test is done to explore the recoverability by inverting the synthetic data with no noise. The light blue line in Figure 3.1c shows the solution using the exact same number of kernels, while the transparent red and green lines are solutions using more. It's obvious that with more kernels, the solution will get closer to the step function we input, despite the fact that due to the upward continuation, a full recovery of the step function is not expected. Also, the rapid reduction in the eigenvalue causes the error from the data to be exponentially magnified when it comes to higher order. To further examine this approach, we set a Gaussian input slip centering 8km depth with the maximum slip being 1m (Figure 3.1d). The conclusion remains the same. In both cases, the surface deformation is well fit with the selected kernels determined from the misfit function $\chi^2 = \Sigma_{i=1}^{N}(d_i - d_i^{pred})^2/N\sigma_i^2$ (Figure S3.1). Note that from the theory (Section 3.2), if the same fault geometry is determined, once the locations of observations are set, every computation step will be the same until the calculation of coefficients for the kernels. In other words, both cases shown in Figure 3.1c and Figure 3.1d are just different re-compositions of the kernels shown in Figure 3.1b, based on different surface observations.

After considering the 2-D test, we expanded the formulation to a 3-D test case. We use a 350km long 250km wide planar fault with N30°E strike and 15° dip toward east. The input dip-slip is a Gaussian function shown in Figure 3.2a, with the corresponding moment magnitude being 8.0. Then we generate a forward model using the half-space Green's function [Okada 1985] and project the vector surface deformation into descend-

ing and ascending line-of-sight (LOS) directions to simulate the InSAR observations. Random noise (2% of maximum amplitude) [Fialko 2004] is added and then the data are down sampled with a quad-tree algorithm [Jónsson et al. 2002] based on the curvature of the deformation field. Due to the complexity of the 3-D half-space Green's function [Okada 1985], the computation of the Gram matrix is done with numerical integration for both strike and dip slip. We then decompose the Gram matrix to recover the eigenvalues and orthonormal kernels (Figure S3.3i, S3.6). We found the 3-D case has a much slower fall-off in misfit with increasing number of kernel functions than the 2-D case. To determine how many kernels to use, we examine the misfit function (Figure 3.2c) and chose the smallest number with reasonable misfit reduction (e.g. 100 kernels), in which case, more kernels will result in an explosion in model's uncertainty but no significant improvement on data fitting. While the along-strike cumulative dip slip shows a good fit to the input (Figure 3.2b) with the recovered moment magnitude being 7.99, a small component of strike slip was also "recovered", potentially due to incomplete coverage from down-sampled data and the noise we added. Besides, we also discovered some short wavelength undulations in the inverted slip, which we believe is due to the nature of this decomposition method.

To further understand the spatial resolution of the inversion, we developed a technique to qualitatively represent the resolving power of the slip model (Figure S3.2). For each kernel used in the construction of the model, we pick out the peaks and troughs, together with the corners and sides, to create a set of nodes. Next, we apply Delaunay triangulation [Delaunay 1934] to these nodes and set their values to the average of the distances between each node and its adjacent nodes. Then we fit these distance measures at each vertex using splines in tension [Smith and Wessel, 1990] and filter the result to get the resolving wavelength map for the kernel. When applying this to all the kernels

used in the spectral expansion inversion, the minimum value among all the kernels at every position on the fault plane is considered as the resolving wavelength for the model (Figure 3.2e and 3.2g). We also performed further tests for dip slip and a mixture of dip and strike slip scenarios, the results of which are presented in supplementary information (Figure S3.7, S3.8).

The two test cases reveal some interesting features of this spectral expansion approach. First, the eigenvalues derived from the Gram matrix decrease slower in the 3-D case than the 2-D case. We believe this is because the data in the 3-D case requires extra constraints for one more dimension, thus more eigenvalues are needed to achieve the same level of trade-offs. Second, the resolving power of the model depends a lot on data sampling. It's obvious, even from the equations in Section 3.2, that the shapes of kernels are completely determined by the model geometry and distribution of the data samples. The derived resolving wavelength could also act as a guide for the digitization of parameter estimation models. Third, the 2-D case shows an increase in uncertainty at shallower depth since it has complete surface coverage. The 3-D case shows a similar feature, but suddenly the uncertainty becomes smaller at the surface, which we relate to the lack of near-fault data. The truth is that the data can never be dense enough when it comes close to the fault, as the Green's function will change dramatically over a short distance. This inversion approach relies heavily on the similarity of Green's function between data points, i.e. the redundancy of data. Thus, in this case, the quad-tree algorithm may not be optimal for down sampling, as the redundancy of data is dependent on fault depth. Fourth, although the computation is defined as the inner product of the Green' functions over the model space, i.e. how similar their Green's functions are, the Gram matrix could potentially represent the covariance (after scaling by the data's uncertainty) between data points, if we assume the data having zero mean. In other words,

if the measurement of one data point changes away from zero due to an earthquake, the measurement of a nearby data point may also change correspondingly. Finally, the fault could be in any shape as long as the integration shown in Equation 3.3 can be done properly, which gives a strong adaptability to this approach.

3.4   Application to the 2010 Maule and the 2015 Gorkha earthquakes

We first use this spectral expansion approach to model the slip for the Mw 8.8 Maule, Chile earthquake. This earthquake was a megathrust event that ruptured a mature seismic gap [Moreno, Rosenau, and Oncken 2010] and generated a strong tsunami throughout the Pacific Ocean [Fritz et al. 2011]. Previous study shows coseismic rupture extending down-dip to a depth of $\sim$40km, which correlates well with interseismic coupling along the Andean subduction zone in south-central Chile [Lorito et al. 2011; Métois, Socquet, and Vigny 2012]. Here we apply the spectral expansion approach to the processed InSAR and GPS data presented in Tong et al. [2010] and analyze the uncertainty and resolving power of the model. We use the same fault geometry as in their study, with the fault plane extending 680 km along strike N16.5°E and 250km down dip 15° toward east. From the misfit function analysis (Figure 3.3e), we determined that 150 kernels were needed to represent the coseismic slip. The solution (Figure 3.3a and 3.3b) shows a total slip moment corresponding to moment magnitude 8.79 assuming an average shear modulus of 40GPa, with the thrust component being Nm and the strike component being Nm. This is close to the seismic moment reported by [NEIC 2010] (Mw 8.8). From the resolving wavelength analysis (Figure 3.3c and 3.3d), the model has the best resolution at intermediate depth (20 km to 40 km), with resolution decreasing

dramatically outside of this range. More interestingly, at shallower depth, due to the lack of offshore data, the resolution is actually worse than at deeper depth. This brings into question the very small uncertainty estimates near the fault surface. Are we so sure the uncertainty of the slip estimate is almost zero close to fault trace? The answer is yes, with a sacrifice in resolution, the statistical precision is almost intrinsically guaranteed. The cumulative dip slip (Figure 3.5a) increases from 0km to 20km depth and decreases to zero at roughly 45km depth. This is in good agreement with previous studies and the uncertainty of our model together with the resolving power analysis show that the reduction in slip amplitudes is well determined by observations.

We then reinvestigate the 2015 Mw 7.8 Gorkha earthquake in Nepal. This earthquake took place on a tectonic boundary due to the Indian-Eurasian collision and ruptured 140km on the Main Himalayan Fault [Galetzka et al. 2015]. In contrast to megathrust events at subduction zones, previous studies all show a very limited down-dip rupture extent with coseismic slip typically terminating between 15 km to 25 km depth [Wang and Fialko 2015; Galetzka et al. 2015]. Here we apply the spectral expansion inversion to the InSAR data from Lindsey et al. [2015] and GPS data from Galetzka et al. [2015]. We down-sample the InSAR data using the quad-tree algorithm with increased sampling density closer to the fault in order to increase the resolution at shallow depth. The sampling stops 20 km away from fault in order to maintain numerical stability and save computation time. We then combine the InSAR and GPS data to perform the spectral expansion inversion. The model is created following the main frontal thrust geometry from Ader et al. [2012], with the fault plane extending 200km along strike N71.5°W and 150 km along dip 7° toward north [Wang and Fialko, 2015]. By examining the misfit function, we determined that 250 kernels were needed to represent the coseismic slip (Figure 3.4e). The estimated total moment for the coseismic slip (Figure 3.4a and

3.4b) is Nm, with the corresponding moment magnitude being 7.80, assuming an average shear modulus of 30 GPa, which agrees with the seismic moment reported by [NEIC 2015] (Mw 7.8). From the resolving wavelength analysis (Figure 3.4c and 3.4d), the resolving power generally decays with depth except in areas with denser samples due to the quad-tree sampling. The cumulative dip slip with depth plot (Figure 3.5b) shows slip rapidly increasing at about 7 km depth, reaches its maximum around 10 km, and then decreases toward zero gradually. The slip vs. depth profile is in agreement with the previous studies [Wang and Fialko 2015]. From the uncertainty estimates and the resolving power analysis, this decay is also well resolved by the data.

For these two cases, the InSAR data's uncertainty is taken from previous studies, with 10 cm for all InSAR data in the Maule case [Tong, Sandwell, and Fialko 2010] and 2.3 cm, 5.4 cm, 4.1 cm for track 47, 48, 157 in the Nepal case [Wang and Fialko 2015]. One interesting feature from the spectral expansion is that the eigenvalues computed for the Maule case (Figure S3.4i) decreases faster than for the Nepal case (Figure S3.5i), potentially because the Nepal earthquake has a shallower dipping angle or more data close to trench.

3.5 Discussion

3.5.1 The influence of erosion rate on thermal structure

The inversion approach we developed in this study confirms that the contrasting down-dip rupture extents of the two earthquakes are indeed well determined by observations. This raises the next question: Why is the down-dip rupture extent of Himalayan megathrust earthquakes (15-20 km) a factor of 2 shallower than the down-dip limit (>40

km) of megathrust earthquakes in oceanic subduction zones? Temperature exerts a strong influence on both dehydration reactions and deformation mechanisms. In particular, the transition from friction to intracrystalline plasticity as the dominant deformation mechanism in quartzofeldspathic rocks occurs at temperatures of 325 - 350°C, and is often proposed to define the upper temperature bound for seismic behavior in crustal rocks [Hyndman and Wang 1993; Hyndman, Wang, and Yamano 1995; Hyndman, Yamano, and Oleskevich 1997; Oleskevich, Hyndman, and Wang 1999]. It has been also proposed that earthquake ruptures initiated below this temperature bound may propagate with decreasing slip to where the temperature is 450 °C [Hyndman, Yamano, and Oleskevich 1997].

Due to the existence of subduction, the temperature is generally higher on the side of the overriding plate, which is roughly around 600 °C [Klingelhoefer et al. 2010]. The rapid subduction of cooler oceanic lithosphere will depress the isotherms on the megathrust interface, but this can account for only a 5 km deepening when subduction rate changes from 2cm/yr to 4cm/yr [Klingelhoefer et al. 2010]. To further understand what is causing the factor of 2 difference between the Himalayian rupture depth and the Maule rupture depth, we follow Royden [1993] and developed a 1-D heat conduction model that accounts for the effect of erosion rate (Appendix). We assume that the surface is at a quasi-steady stage where the uplift from accretion and rebound is balanced by the effect of erosion. We then adopt the parameters in Royden [1993] who assumes the erosion rate to be 1 mm/yr and vary the remaining variables to calculate the corresponding temperature profiles (Figure 3.6). From our analysis, both the heat production in the upper crust and the mantle temperature has little effect on depth of the 600 °C isotherm, while the erosion rate influences the temperature profile significantly. This can be understood by considering the effects of accretion or erosion/rebound; the hotter materials are

directly brought up toward the surface, which is far more efficient than heat conduction. Recent studies show that in the region of the Gorkha earthquake, the surface erosion rate increases from about 0.5 mm/yr in the up-dip region to 3.5 mm/yr down dip [Whipple et al. 2016], while for south-central Chile, this number is quite small (< 0.3 mm/yr) [Aguilar et al. 2011; Carretier et al. 2013]. Figure 3.6a shows that an average 1 mm/yr erosion rate is sufficient to bring the 600 °C isotherm from a depth of 40 km to 17 km, which is consistent with our findings from spectral expansion inversion.

3.5.2 Correlations between forearc ridges and the down-dip limit of the seismogenic zone

Bassett and Watts [Bassett and Watts 2015a; Bassett and Watts 2015b] have developed a spectral averaging method of suppressing the large-amplitude, long-wavelength, trench-normal topographic and gravimetric expression of subduction zones. The global application of this technique revealed that in at-least five circum-Pacific subduction zones with a history of large megathrust earthquakes, the down-dip limit of the seismogenic zone was approximately correlated with the location of a trench-parallel forearc ridge (TPFR). The longest TPFR parallels the coastline of Chile for >2000 km and is coincident with the Chilean coastal Cordillera. As shown in Figure 3.7, the TPFR in southern Chile is well correlated with the maximum depth of earthquakes with Global Centroid Moment Tensors (GCMT) [Dziewonski, Chou, and Woodhouse 1981; Ekström, Nettles, and Dziewoński 2012] consistent with megathrust slip, the maximum depth of coseismic slip in the 2010 Mw 8.8 Maule earthquake [Tong, Sandwell, and Fialko 2010; Delouis, Nocquet, and Vallée 2010], and the maximum depth of interseismic coupling as constrained by campaign GPS measurements [Moreno, Rosenau, and Oncken 2010]. A similar correlation has been recognised in northern Chile [Béjar-Pizarro et al. 2013].

To investigate whether a similar relation is observed for the Gorka earthquake, we have applied this technique of spectral averaging to calculate residual topographic anomalies along the Himalayas. We have analyzed the global SRTM15 topographic grid, which has a resolution of 15 arc-seconds (roughly 500m). Residual topographic anomalies along the Himalayas are shown in Figure 8. The Gorka earthquake occurred immediately up-dip of an elongated, strike-parallel region of positive residual topographic anomalies, which correlates remarkably well with the 3500 m elevation contour of the Hymalayas [Avouac 2003; Stevens and Avouac 2015]. This elevated band may be analogous to the TPFR previously observed in oceanic subduction zones. Black contours show the distribution of interseismic coupling as constrained by campaign GPS measurements [Stevens and Avouac 2015]. It is intriguing that we observe a similar spatial association between the down-dip transition from an interseismically locked to creeping megathrust, with the elevated residual topography of the high Himalayas.

In subduction zones, the broad pattern of interseismic deformation can be modeled by placing an edge dislocation at the down dip end of the locked fault with its Burger's vector parallel to fault dip [Savage 1983]. This model predicts a broad interseismic subsidence over the majority of the locked fault, with interseismic uplift located near the down-dip limit of locking. Over many earthquake cycles, the incomplete recovery of interseismic elastic deformation by earthquakes and postseismic slip may lead to permanent deformation of the forearc that spatially mirrors the sign of interseismic deformation. This model has been proposed to explain long-term coastal uplift in oceanic subduction zones in Cascadia [Kelsey et al. 1994] and Mexico [Ramırez-Herrera, Kostoglodov, and Urrutia-Fucugauchi 2004] and we suggest unrecovered interseismic deformation may also be contributing to the elevation and growth of the high Himalaya

in eastern Nepal, which is in agreement with previous studies [Meade 2010].

3.6   Conclusions

In this study, we developed and tested a data-driven spectral expansion approach that possess the advantages of 1) mathematical robustness, 2) smoothness and stableness without regularization, 3) capability of adopting complex fault surface, 4) giving real uncertainty estimates and 5) providing resolving power analysis. With this approach, we confirmed that the down dip ruptures of the 2010 Mw 8.8 Maule earthquake and the 2015 Mw 7.8 Gorkha earthquake are well resolved by the data. The Maule earthquake rupture terminates around 45 km depth and the Gorkha earthquake rupture stops shallower than 20 km. Both these depths are well correlated with the location of trench-parallel forearc ridges, which may reflect unrecovered interseismic elastic deformation. To understand the difference in maximum rupture depth between the two cases, we constructed 1-D thermal conduction models with different erosion rate, upper-crust heat production and mantle temperature. By comparing different models, we conclude that the erosion rate has a major influence on the down dip rupture limit.

Appendix: Derivation of the 1-D Heat Conduction Model

Following Royden [1993], we simplified and modified the heater conduction equation as follows, assuming the accretion and erosion rates are in balance.

$$\frac{d^2 T}{dz^2} + \frac{\nu}{\alpha}\frac{dT}{dz} + \frac{A_0}{K}e^{-z/h} = 0$$

where T is the temperature, z is the depth, v is the accretion rate, α is the thermal diffusivity, A_0 is the heat production rate at the surface, K is the thermal conductivity and h is the characteristic decaying depth for heat production. We simplify the equation a little more by substituting some of the variables as follows.

$$\frac{d^2T}{dz^2} + a\frac{dT}{dz} + be^{-cz} = 0$$

Then further simplify the equation form a 2-nd order ordinary differential equation (ODE) to a 1-st order ODE by letting $dT/dz = y$. Then we have the equation as

$$\frac{dy}{dz} + ay + be^{-cz} = 0$$

As for the type of 1-st order ODE like $y' + P(xy = Q(x))$, the general solution is

$$y = e^{-\int_{x_0}^{x} P(t)dt} \int Q(x)e^{\int_{x_0}^{x} P(t)dt} dx$$

Thus, we have the solution for y as

$$y = -\frac{b}{a-c}(e^{-cz} + C_1 e^{-az})$$

Substitute y with dT/dz and solve the ODE, we'll get

$$T = \frac{b}{c(a-c)}e^{-cz} + C_1\frac{b}{a(a-c)}e^{-az} + C_2$$

Consider the boundary condition

$$z = 0, \qquad T = T_0$$

$$z = H, \qquad T = T_m$$

We can get the coefficients

$$C_1 = -\left(T_m \frac{a(a-c)}{b} + \frac{a}{c}(1 - e^{-cH}) \right) / (1 - e^{-aH})$$

$$C_2 = \left(T_m + \frac{b}{c(a-c)}(e^{-aH} - e^{-cH}) \right) / (1 - e^{-aH})$$

Acknowledgements

Chapter 3, in full, is a reprint of the material as it appears in Geophysical Journal International: Xu, X., Sandwell, D.T. and Bassett, D., 2017, "A Spectral Expansion Approach for Geodetic Slip Inversion: Implications for the Down-dip Rupture Limits of Oceanic and Continental Megathrust Earthquakes", *Geophysical Journal International*,

p.ggx408. The dissertation author is the primary investigator and author of this paper.

References

Ader, T., Avouac, J.-P., Liu-Zeng, J., Lyon-Caen, H., Bollinger, L., Galetzka, J., Genrich, J., Thomas, M., Chanard, K., Sapkota, S. N., Sudhir, R., Shrestha, P., Ding, L., and Flouzat, M. (2012). "Convergence rate across the Nepal Himalaya and interseismic coupling on the Main Himalayan Thrust: Implications for seismic hazard". In: *Journal of Geophysical Research: Solid Earth* 117.B4.

Aguilar, G., Riquelme, R., Martinod, J., Darrozes, J., and Maire, E. (2011). "Variability in erosion rates related to the state of landscape transience in the semi-arid Chilean Andes". In: *Earth Surface Processes and Landforms* 36.13, pp. 1736–1748.

Ammon, C. J., Ji, C., Thio, H.-K., Robinson, D., Ni, S., Hjorleifsdottir, V., Kanamori, H., Lay, T., Das, S., Helmberger, D., Ichinose, G., Polet, J., and Wald, D. (2005). "Rupture process of the 2004 Sumatra-Andaman earthquake". In: *Science* 308.5725, pp. 1133–1139.

Avouac, J.-P. (2003). "Mountain building, erosion, and the seismic cycle in the Nepal Himalaya". In: *Advances in geophysics* 46, pp. 1–80.

Bassett, D. and Watts, A. B. (2015a). "Gravity anomalies, crustal structure, and seismicity at subduction zones: 1. Seafloor roughness and subducting relief". In: *Geochemistry, Geophysics, Geosystems* 16.5, pp. 1508–1540.

— (2015b). "Gravity anomalies, crustal structure, and seismicity at subduction zones: 2. Interrelationships between fore-arc structure and seismogenic behavior". In: *Geochemistry, Geophysics, Geosystems* 16.5, pp. 1541–1576.

Béjar-Pizarro, M., Socquet, A., Armijo, R., Carrizo, D., Genrich, J., and Simons, M. (2013). "Andean structural control on interseismic coupling in the North Chile subduction zone". In: *Nature Geoscience* 6.6, pp. 462–467.

Carretier, S., Regard, V, Vassallo, R, Aguilar, G, Martinod, J, Riquelme, R, Pepin, E, Charrier, R, Hérail, G., Farías, M, Guyot, J.-L., Vargas, G, and Lagane, C. (2013). "Slope and climate variability control of erosion in the Andes of central Chile". In: *Geology* 41.2, pp. 195–198.

Chlieh, M., Avouac, J.-P., Hjorleifsdottir, V., Song, T.-R. A., Ji, C., Sieh, K., Sladen, A., Hebert, H., Prawirodirdjo, L., Bock, Y., and Galetzka, J. (2007). "Coseismic slip and afterslip of the great Mw 9.15 Sumatra–Andaman earthquake of 2004". In: *Bulletin of the Seismological Society of America* 97.1A, S152–S173.

Cohen, S. C. (1999). "Numerical models of crustal deformation in seismic zones". In: *Advances in Geophysics* 41, pp. 133–231.

Delaunay, B. (1934). "Sur la sphere vide". In: *Izv. Akad. Nauk SSSR, Otdelenie Matematicheskii i Estestvennyka Nauk* 7.793-800, pp. 1–2.

Delouis, B., Nocquet, J.-M., and Vallée, M. (2010). "Slip distribution of the February 27, 2010 Mw= 8.8 Maule earthquake, central Chile, from static and high-rate GPS, InSAR, and broadband teleseismic data". In: *Geophysical Research Letters* 37.17.

Dziewonski, A., Chou, T.-A., and Woodhouse, J. (1981). "Determination of earthquake source parameters from waveform data for studies of global and regional seismicity". In: *Journal of Geophysical Research: Solid Earth* 86.B4, pp. 2825–2852.

Ekström, G, Nettles, M, and Dziewoński, A. (2012). "The global CMT project 2004–2010: Centroid-moment tensors for 13,017 earthquakes". In: *Physics of the Earth and Planetary Interiors* 200, pp. 1–9.

Fialko, Y. (2004). "Probing the mechanical properties of seismically active crust with space geodesy: Study of the coseismic deformation due to the 1992 Mw7. 3 Landers (southern California) earthquake". In: *Journal of Geophysical Research: Solid Earth (1978–2012)* 109.B3.

Fritz, H. M., Petroff, C. M., Catalán, P. A., Cienfuegos, R., Winckler, P., Kalligeris, N., Weiss, R., Barrientos, S. E., Meneses, G., Valderas-Bermejo, C., Ebeling, C., Papadopoulos, A., Contreras, M., Almar, R., Dominguez, J. C., and Synolakis, C. E. (2011). "Field survey of the 27 February 2010 Chile tsunami". In: *Pure and Applied Geophysics* 168.11, pp. 1989–2010.

Galetzka, J., Melgar, D., Genrich, J. F., Geng, J., Owen, S., Lindsey, E. O., Xu, X., Bock, Y., Avouac, J.-P., Adhikari, L. B., Upreti, B. N., Pratt-Sitaula, B., Bhattarai, T. N., Sitaula, B. P., Moore, A., Hudnut, K. W., Szeliga, W., Normandeau, J., Fend, M., Flouzat, M., Bollinger, L, Shrestha, P, Koirala, B, Gautam, U, Bhatterai, M, Gupta, R, Kandel, T, Timsina, C, Sapkota, S., Rajaure, S, and Maharjan, N (2015). "Slip pulse and resonance of the Kathmandu basin during the 2015 Gorkha earthquake, Nepal". In: *Science* 349.6252, pp. 1091–1095.

Gilbert, F. (1971). "Ranking and winnowing gross Earth data for inversion and resolution". In: *Geophysical Journal International* 23.1, pp. 125–128.

Hyndman, R., Wang, K, and Yamano, M (1995). "Thermal constraints on the seismogenic portion of the southwestern Japan subduction thrust". In: *Journal of Geophysical Research: Solid Earth* 100.B8, pp. 15373–15392.

Hyndman, R. and Wang, K. (1993). "Thermal constraints on the zone of major thrust earthquake failure: The Cascadia subduction zone". In: *Journal of Geophysical Research: Solid Earth* 98.B2, pp. 2039–2060.

Hyndman, R. D., Yamano, M., and Oleskevich, D. A. (1997). "The seismogenic zone of subduction thrust faults". In: *Island Arc* 6.3, pp. 244–260.

Jónsson, S., Zebker, H., Segall, P., and Amelung, F. (2002). "Fault slip distribution of the 1999 Mw 7.1 Hector Mine, California, earthquake, estimated from satellite radar and GPS measurements". In: *Bulletin of the Seismological Society of America* 92.4, pp. 1377–1389.

Kelsey, H. M., Engebretson, D. C., Mitchell, C. E., and Ticknor, R. L. (1994). "Topographic form of the Coast Ranges of the Cascadia margin in relation to coastal uplift rates and plate subduction". In: *Journal of Geophysical Research: Solid Earth* 99.B6, pp. 12245–12255.

Klingelhoefer, F., Gutscher, M.-A., Ladage, S, Dessa, J.-X., Graindorge, D., Franke, D, André, C., Permana, H., Yudistira, T, and Chauhan, A. (2010). "Limits of the seismogenic zone in the epicentral region of the 26 December 2004 great Sumatra-Andaman earthquake: Results from seismic refraction and wide-angle reflection surveys and thermal modeling". In: *Journal of Geophysical Research: Solid Earth* 115.B1.

Lay, T., Kanamori, H., Ammon, C. J., Nettles, M., Ward, S. N., Aster, R. C., Beck, S. L., Bilek, S. L., Brudzinski, M. R., Butler, R., DeShon, H. R., Ekström, G., Satake, K., and Sipkin, S. (2005). "The great Sumatra-Andaman earthquake of 26 december 2004". In: *Science* 308.5725, pp. 1127–1133.

Lindsey, E. O., Natsuaki, R., Xu, X., Shimada, M., Hashimoto, M., Melgar, D., and Sandwell, D. T. (2015). "Line-of-sight displacement from ALOS-2 interferometry: Mw 7.8 Gorkha Earthquake and Mw 7.3 aftershock". In: *Geophysical Research Letters* 42.16, pp. 6655–6661.

Lorito, S, Romano, F, Atzori, S, Tong, X, Avallone, A, McCloskey, J, Cocco, M, Boschi, E, and Piatanesi, A (2011). "Limited overlap between the seismic gap and co-seismic slip of the great 2010 Chile earthquake". In: *Nature Geoscience* 4.3, p. 173.

Meade, B. J. (2010). "The signature of an unbalanced earthquake cycle in Himalayan topography?" In: *Geology* 38.11, pp. 987–990.

Métois, M., Socquet, A., and Vigny, C. (2012). "Interseismic coupling, segmentation and mechanical behavior of the central Chile subduction zone". In: *Journal of Geophysical Research: Solid Earth* 117.B3.

Minson, S., Simons, M, Beck, J., Ortega, F, Jiang, J, Owen, S., Moore, A., Inbal, A, and Sladen, A (2014). "Bayesian inversion for finite fault earthquake source models–II: the 2011 great Tohoku-oki, Japan earthquake". In: *Geophysical Journal International* 198.2, pp. 922–940.

Moreno, M., Rosenau, M., and Oncken, O. (2010). "2010 Maule earthquake slip correlates with pre-seismic locking of Andean subduction zone". In: *Nature* 467.7312, p. 198.

NEIC (2010). "National Earthquake Information Center (NEIC) (2010)Magnitude 8.8 Offshore Maule Chile". In: *U. S. Geol. Surv.Denver Colo*.

— (2015). "National Earthquake Information Center (NEIC) (2015)Magnitude 7.8 Gorkha Nepal". In: *U. S. Geol. Surv.Denver Colo*.

Okada, Y. (1985). "Surface deformation due to shear and tensile faults in a half-space". In: *Bulletin of the seismological society of America* 75.4, pp. 1135–1154.

Oleskevich, D., Hyndman, R., and Wang, K (1999). "The updip and downdip limits to great subduction earthquakes: Thermal and structural models of Cascadia, south Alaska, SW Japan, and Chile". In: *Journal of Geophysical Research: Solid Earth* 104.B7, pp. 14965–14991.

Parker, R. L. (1977). "Understanding inverse theory". In: *Annual Review of Earth and Planetary Sciences* 5.1, pp. 35–64.

Parker, R. L. (1994). *Geophysical inverse theory*. Princeton university press.

Ramırez-Herrera, M. T., Kostoglodov, V., and Urrutia-Fucugauchi, J. (2004). "Holocene-emerged notches and tectonic uplift along the Jalisco coast, Southwest Mexico". In: *Geomorphology* 58.1, pp. 291–304.

Royden, L. H. (1993). "The steady state thermal structure of eroding orogenic belts and accretionary prisms". In: *Journal of Geophysical Research: Solid Earth* 98.B3, pp. 4487–4507.

Savage, J. (1983). "A dislocation model of strain accumulation and release at a subduction zone". In: *Journal of Geophysical Research: Solid Earth* 88.B6, pp. 4984–4996.

Simons, M., Fialko, Y., and Rivera, L. (2002). "Coseismic deformation from the 1999 Mw 7.1 Hector Mine, California, earthquake as inferred from InSAR and GPS observations". In: *Bulletin of the Seismological Society of America* 92.4, pp. 1390–1402.

Simons, M., Minson, S. E., Sladen, A., Ortega, F., Jiang, J., Owen, S. E., Meng, L., Ampuero, J.-P., Wei, S., Chu, R., Helmberger, D. V., Kanamori, H., Hetland, E.,

Moore, A. W., and Webb, F. H. (2011). "The 2011 magnitude 9.0 Tohoku-Oki earthquake: Mosaicking the megathrust from seconds to centuries". In: *science* 332.6036, pp. 1421–1425.

Steketee, J. (1958). "On Volterra's dislocations in a semi-infinite elastic medium". In: *Canadian Journal of Physics* 36.2, pp. 192–205.

Stevens, V. and Avouac, J. (2015). "Interseismic coupling on the main Himalayan thrust". In: *Geophysical Research Letters* 42.14, pp. 5828–5837.

Tarantola, A. (2005). *Inverse problem theory and methods for model parameter estimation*. SIAM.

Tong, X., Sandwell, D. T., and Fialko, Y. (2010). "Coseismic slip model of the 2008 Wenchuan earthquake derived from joint inversion of interferometric synthetic aperture radar, GPS, and field data". In: *Journal of Geophysical Research: Solid Earth (1978–2012)* 115.B4.

Wang, K. and Fialko, Y. (2015). "Slip model of the 2015 Mw 7.8 Gorkha (Nepal) earthquake from inversions of ALOS-2 and GPS data". In: *Geophysical Research Letters* 42.18, pp. 7452–7458.

Whipple, K. X., Shirzaei, M., Hodges, K. V., and Arrowsmith, J. R. (2016). "Active shortening within the Himalayan orogenic wedge implied by the 2015 Gorkha earthquake". In: *Nature Geoscience* 9.9, pp. 711–716.

Figures
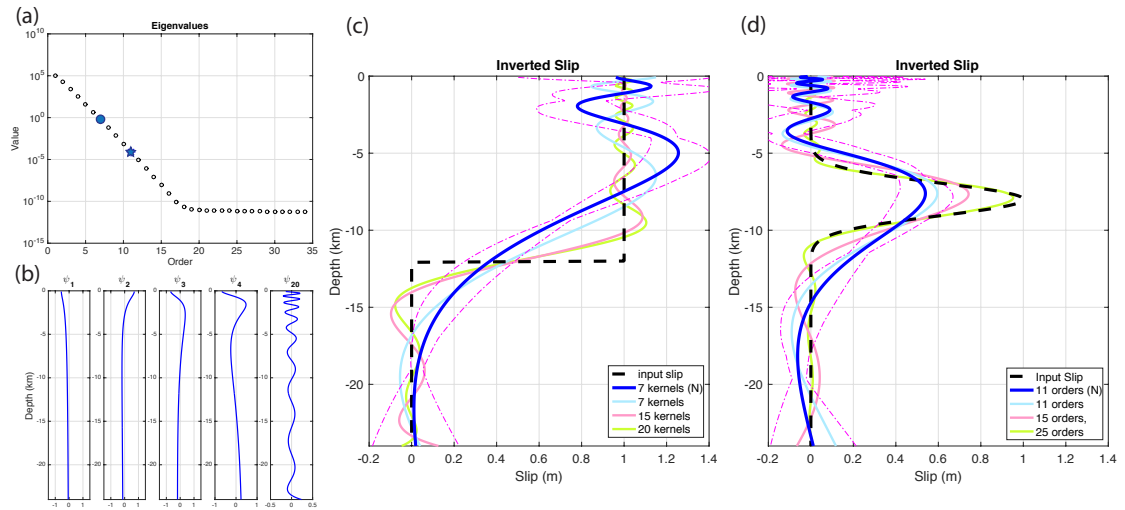
Figure 3.1: **2-D infinite fault test case for the spectral expansion approach.** (a) Eigenvalues vs. order, with the blue circle denoting the order selected for the step case (c) and blue star for the Gaussian case (d) when using noisy data. (b) Some examples of orthonormal kernels vs. depth. (c) Recovered slip vs. depth plot for input slip being a step function and (d) recovered slip vs. depth plot for input slip being a Gaussian function. For (c) and (d), the black dashed lines represent the input slip, blue lines are slip inverted using noisy data with magenta dash-dot lines being the uncertainty bounds, light blue lines are the slip inverted using noise-free data, transparent red and green lines are inverted slip using noise-free data with more kernels. The forward model and fitting can be found in Figure S3.1.
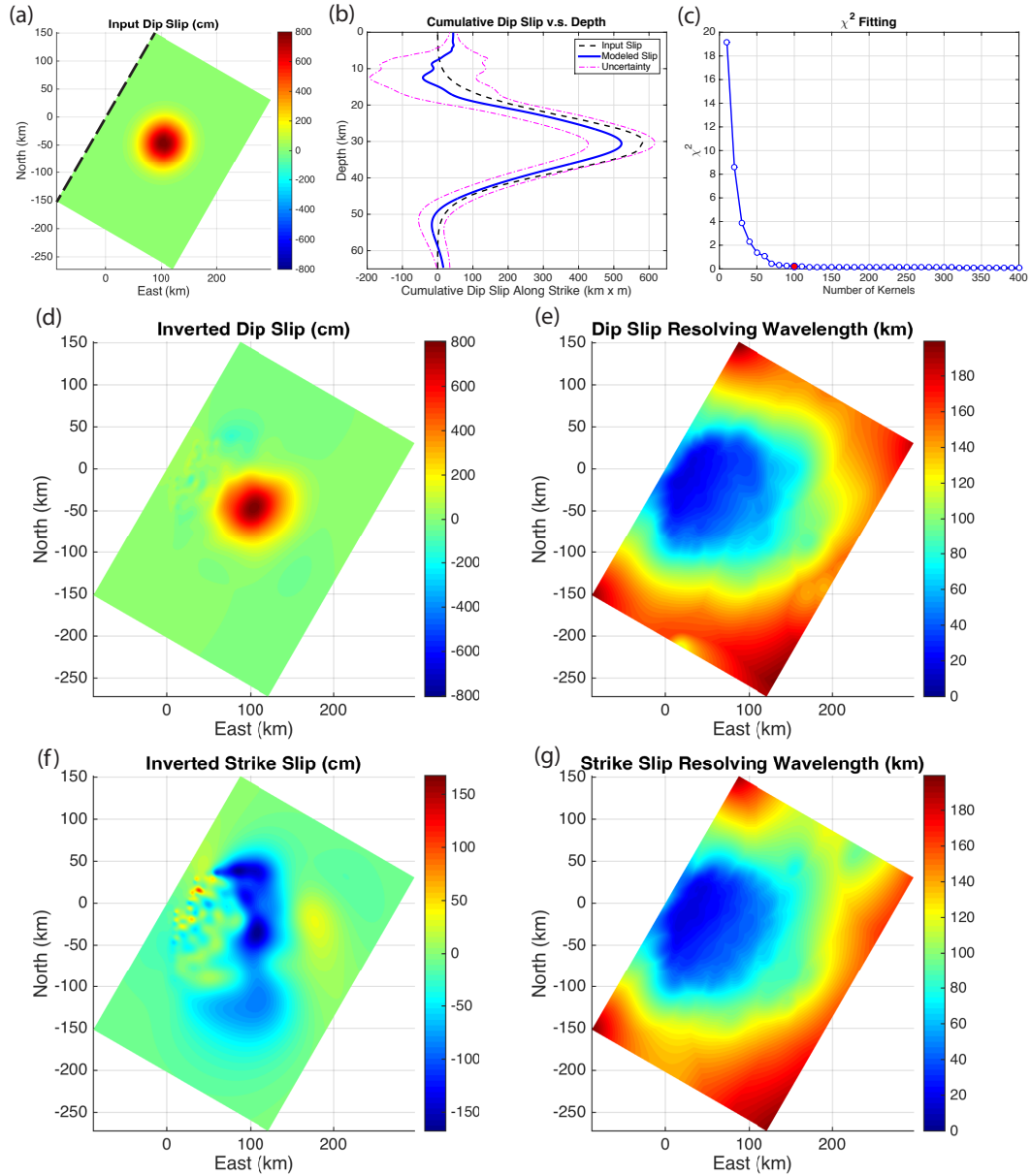
Figure 3.2: **3-D test case for the spectral expansion approach.** (a) Input dip slip with positive defined as hanging wall moving up-dip. The black dashed line is the fault trace. (b) Cumulative dip slip [Simons and Fialko, 2002] vs. depth plot with black dashed line being the input dip slip, blue line representing the inverted dip slip and magenta dash-dot lines denoting the uncertainty. (c) Misfit vs. number of kernels, with the red dot being the order selected. (d) Inverted dip slip and (f) inverted strike slip with hanging wall moving north-eastward defined as positive. Resolving wavelength for dip slip (e) and strike slip (g) constructed by the algorithm shown in Figure S3.2. Data fitting and eigenvalues can be found in Figure S3.3.
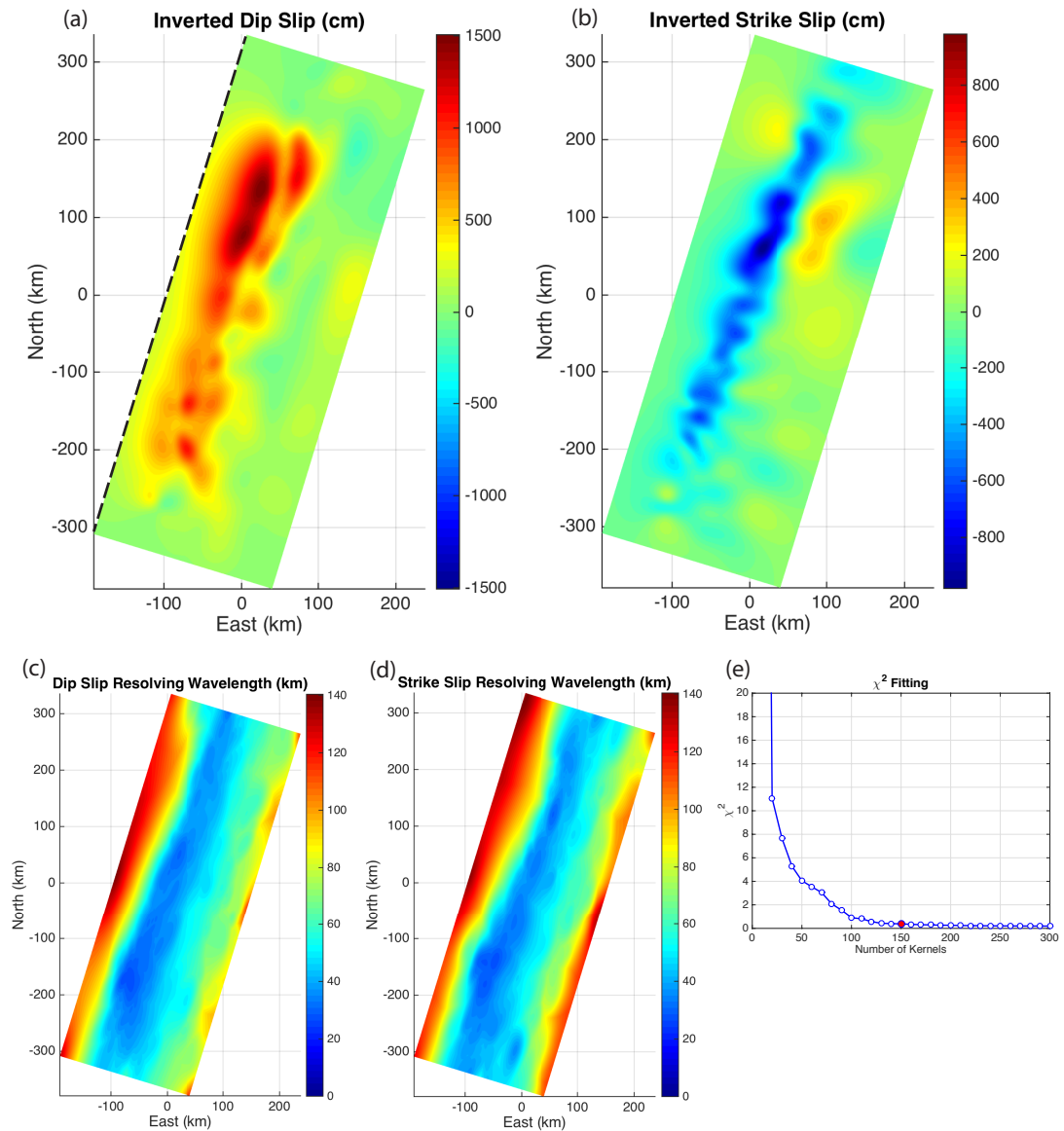
Figure 3.3: **Inverted slip for the 2010 Mw 8.8 Maule Earthquake.** (a) Inverted dip slip and (b) inverted strike slip, with same positivity definition as Figure 2d and 2f. The black dashed line in (a) represents the fault trace. Resolving wavelength for dip slip (c) and strike slip (d). (e) Misfit vs. the number of kernels used. The data fitting, uncertainty estimate and eigenvalues can be found in Figure S3.4.
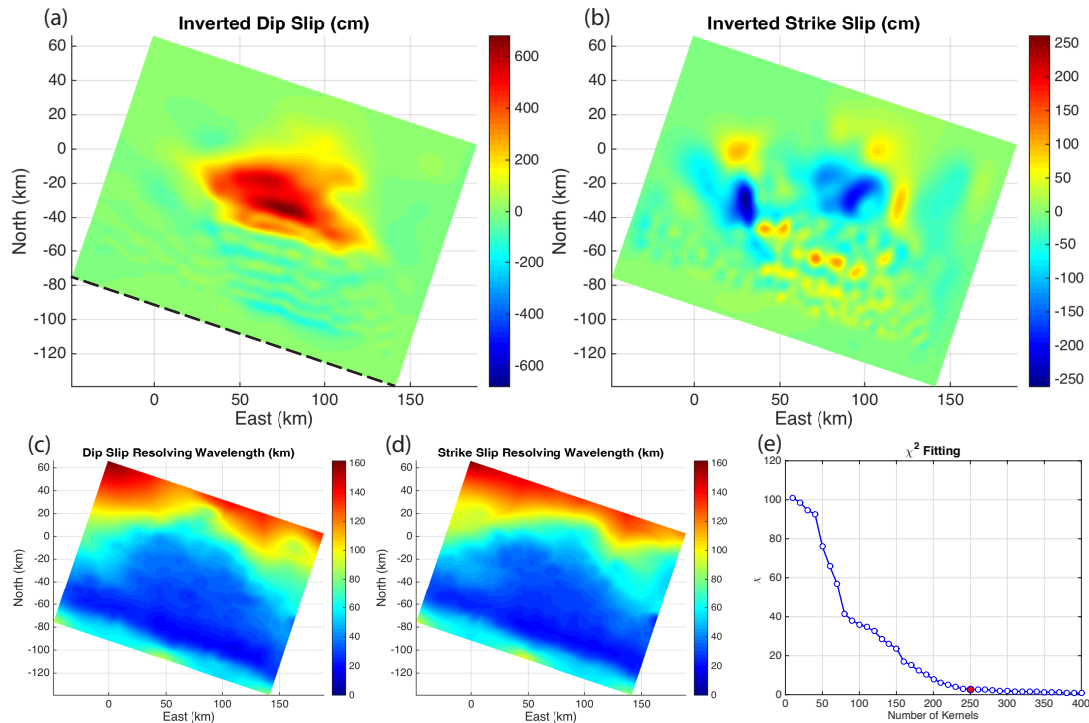
Figure 3.4: **Inverted slip for the 2015 Mw 7.8 Gorkha Earthquake.** (a) Inverted dip slip with same positivity definition as Figure 2d and (b) is the inverted strike slip with positive defined as the hanging wall moving north-westward. The black dashed line in (a) represents the fault trace. Resolving wavelength for dip slip (c) and strike slip (d). (e) Misfit function vs. the number of kernels used. The data fitting, uncertainty estimate and eigenvalues can be found in Figure S3.5.
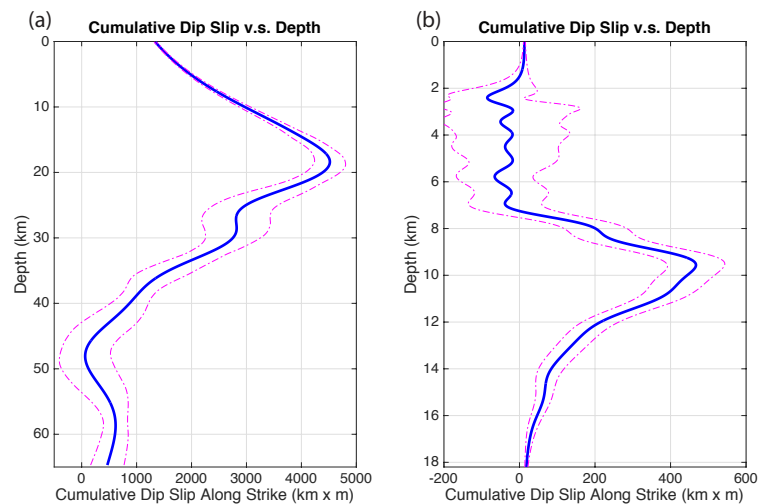
Figure 3.5: **Cumulative dip slip vs. depth plots.** (a) is the 2010 Mw 8.8 Maule Earthquake and (b) is the 2015 Mw 7.8 Gorkha Earthquake, with blue lines denoting the cumulative dip slip and magenta dash-dot lines representing the uncertainty bounds.

Figure 3.6: **Temperature vs. depth for 1-D heat conduction model.** (a) Models with different accretion/erosion rate. (b) Models with different upper crust heat generation rate. (c) Models with different mantle temperature.
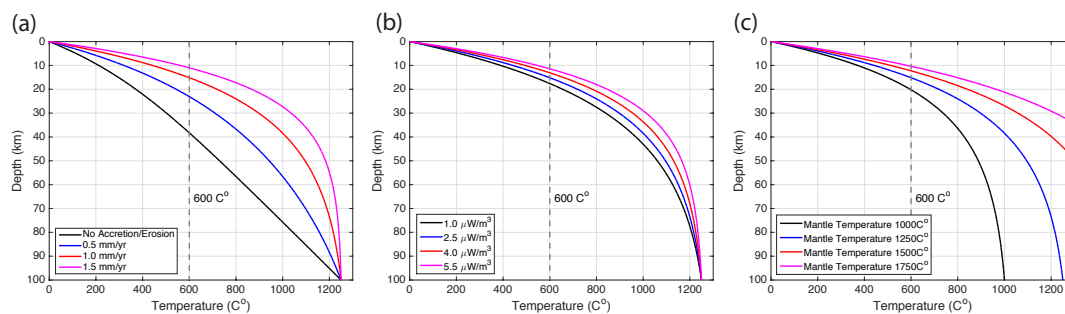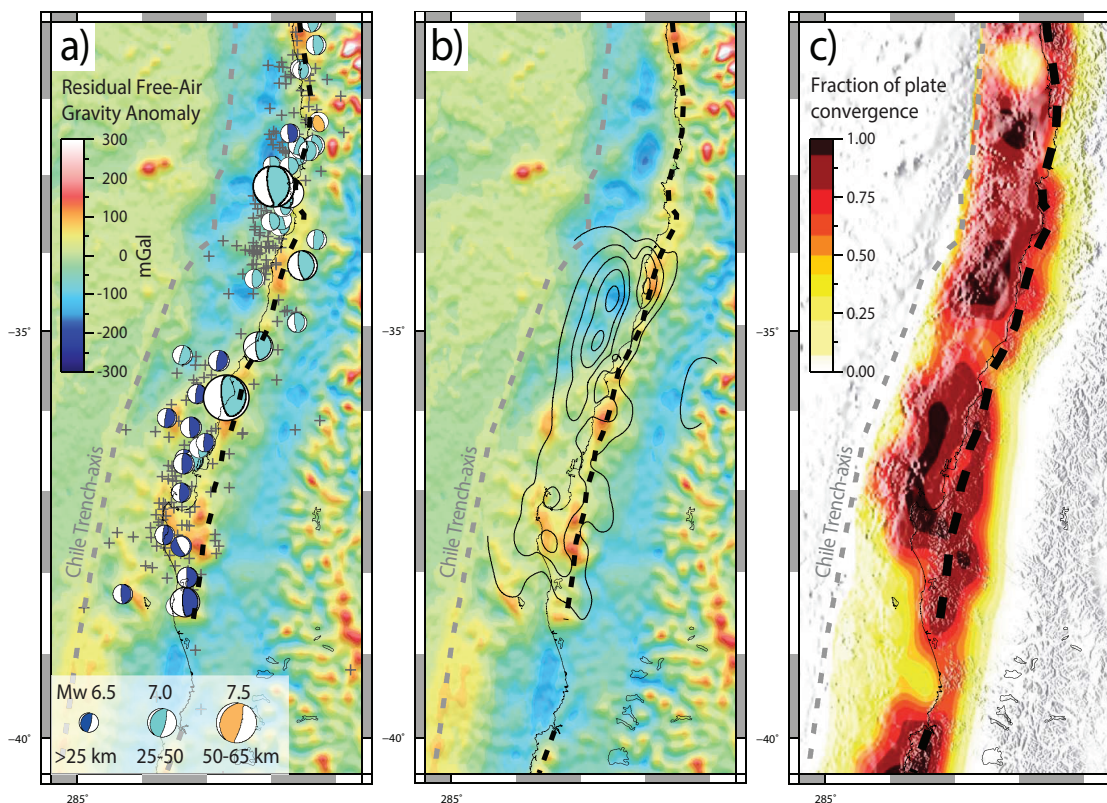

Figure 3.7: **Gravity anomaly over the 2010 Chile earthquake region.** a) Residual free-air gravity anomaly at the 2010 Chile Mw 8.8 earthquake region with grey dashed line denotes the trench axis and the black dashed line represents the TPFR. Grey pluses mark GCMT thrust events with Mw ¡ 6.5. GCMT events with Mw ¿= 6.5 are plotted with beach ball, scaled for magnitude, colored for depth. b) Same as a) with grey solid contours are the inverted slip pattern with each line representing 3m slip. c) Fraction of Plate Convergence from [Moreno et al., 2011]. The grey dashed line and black dashed line are the same as in a) and b).
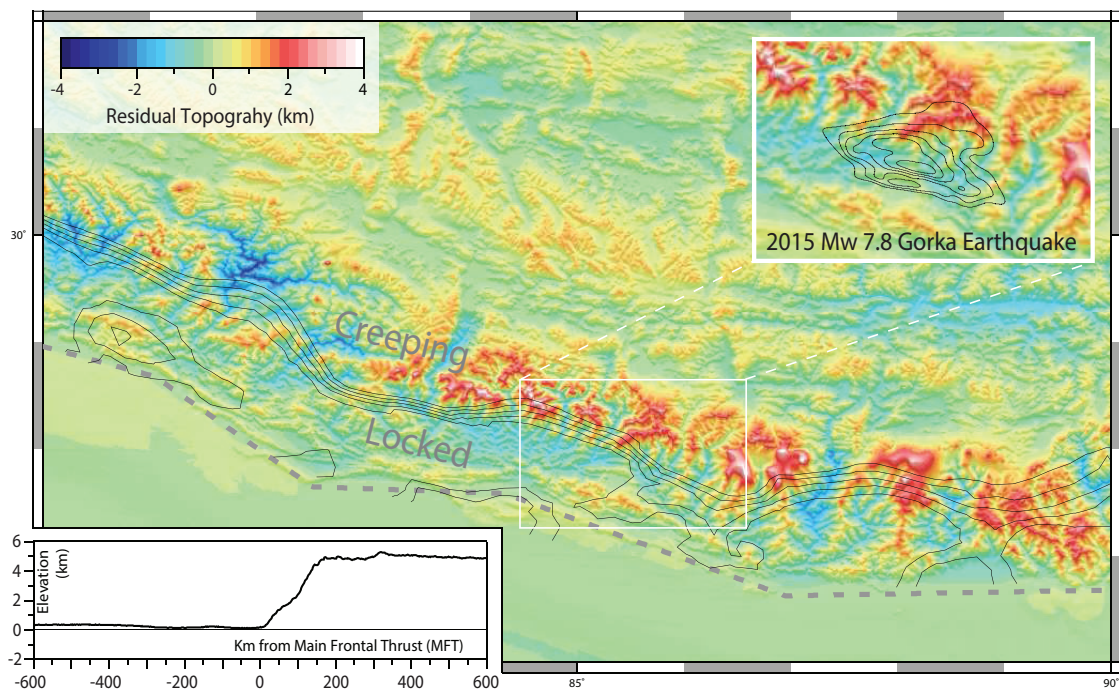
Figure 3.8: **Residual topography for the 2015 Mw 7.8 Nepal earthquake region.** The grey dashed line denotes the Main Frontal Thrust (MFT). The grey lines are the locking contours from [Stevens and Avouac, 2015]. The grey lines in the subplot at upper-right corner are 1-m slip contours. The bottom-left plot is the average elevation at this region.

Supplements
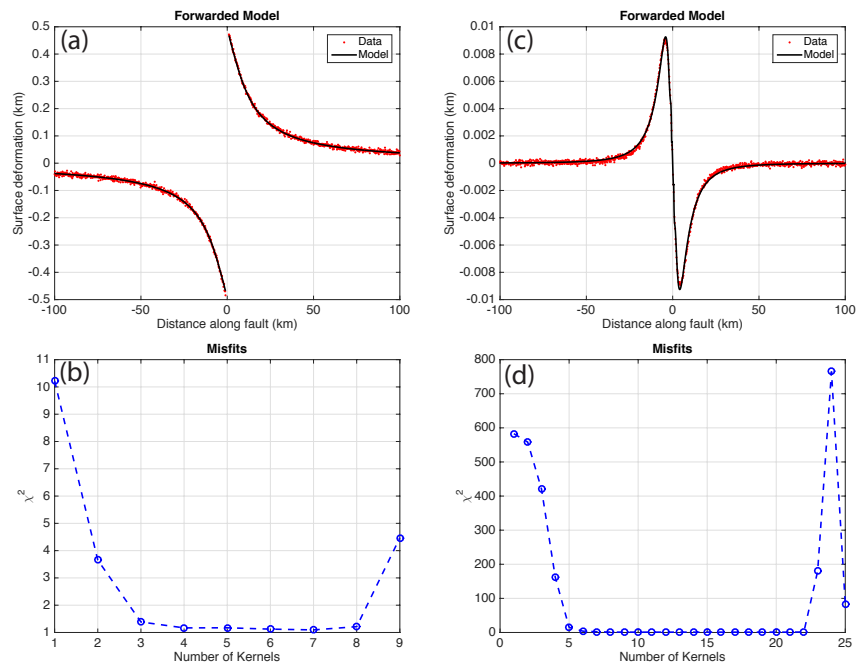
Figure S3.1: **Supplementary figures of 2-D test case**. (a) Comparison between surface deformation derived from the input slip (red dots, noise added) and inverted slip (7 kernels, black line) corresponding to Figure 2c. (b) Misfit function vs. the number of kernels used for Figure 2c. (c) Comparison between surface deformation corresponding to Figure 2d (11 kernels). (d) Misfit function plot vs. number of kernels used for Figure 2d.
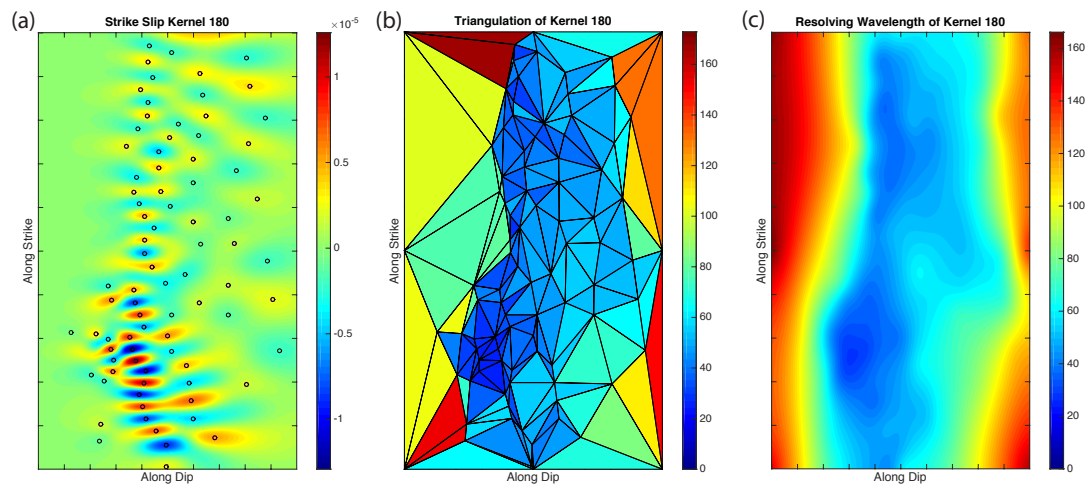
Figure S3.2: **How to calculate representative resolving wavelength of a kernel**. (a) An example 2-D kernel for the 2010 Maule Earthquake, with black circles denoting the peaks and troughs of the kernel. (b) Delaunay triangulation for the nodes (circles) in (a) (adding 8 nodes at corners and middle of sides, value of each node is the average distance from the node to its adjacent nodes), with color representing the average from the triangle's 3 nodes. (c) Map generated applying a surface technique and filtering to the nodes in (b).
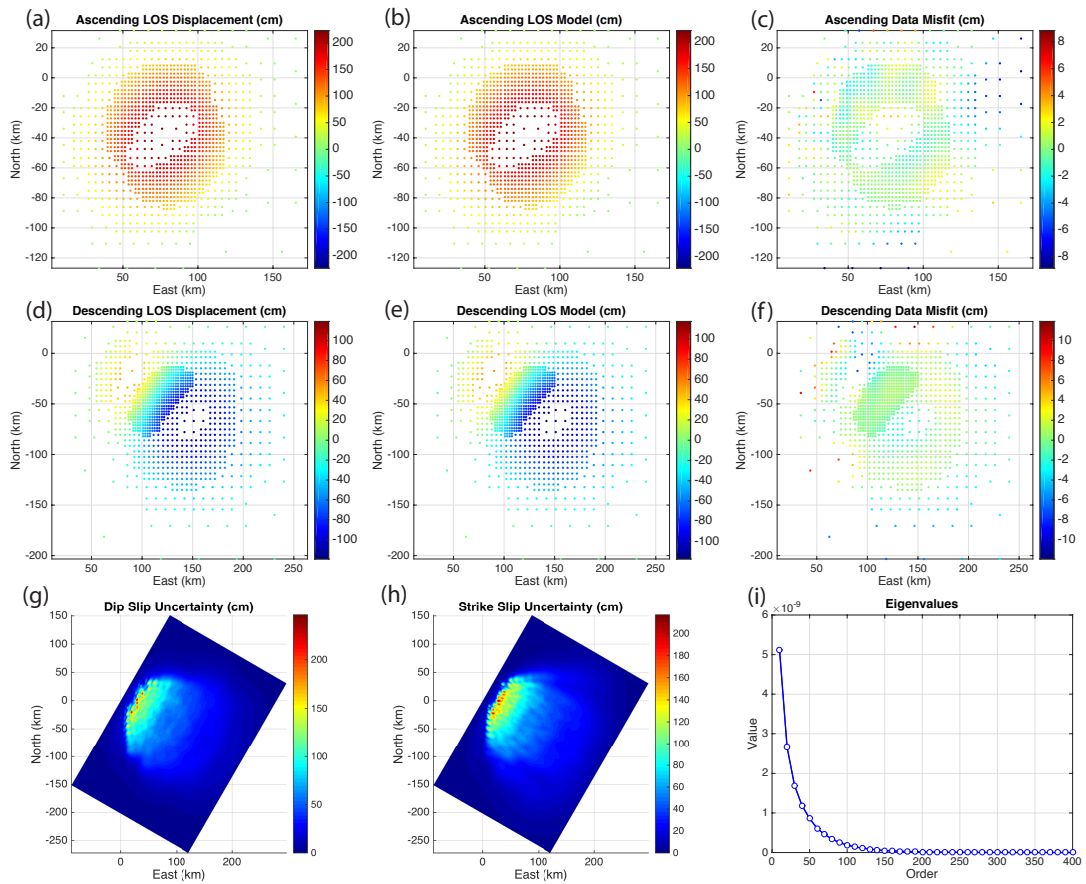
Figure S3.3: **Supplementary figures of the 3-D test case**. Plots (a), (b) and (c) are the subsampled data, forwarded model, and misfit for the simulated noisy ascending data. Plots (d), (e) and (f) are the subsampled data, forwarded model, and misfit for the simulated noisy descending data. (g) Uncertainty map for dip slip in Figure 3d. (h) Uncertainty map for strike slip in Figure 3f. (i) Eigenvalues vs. order.
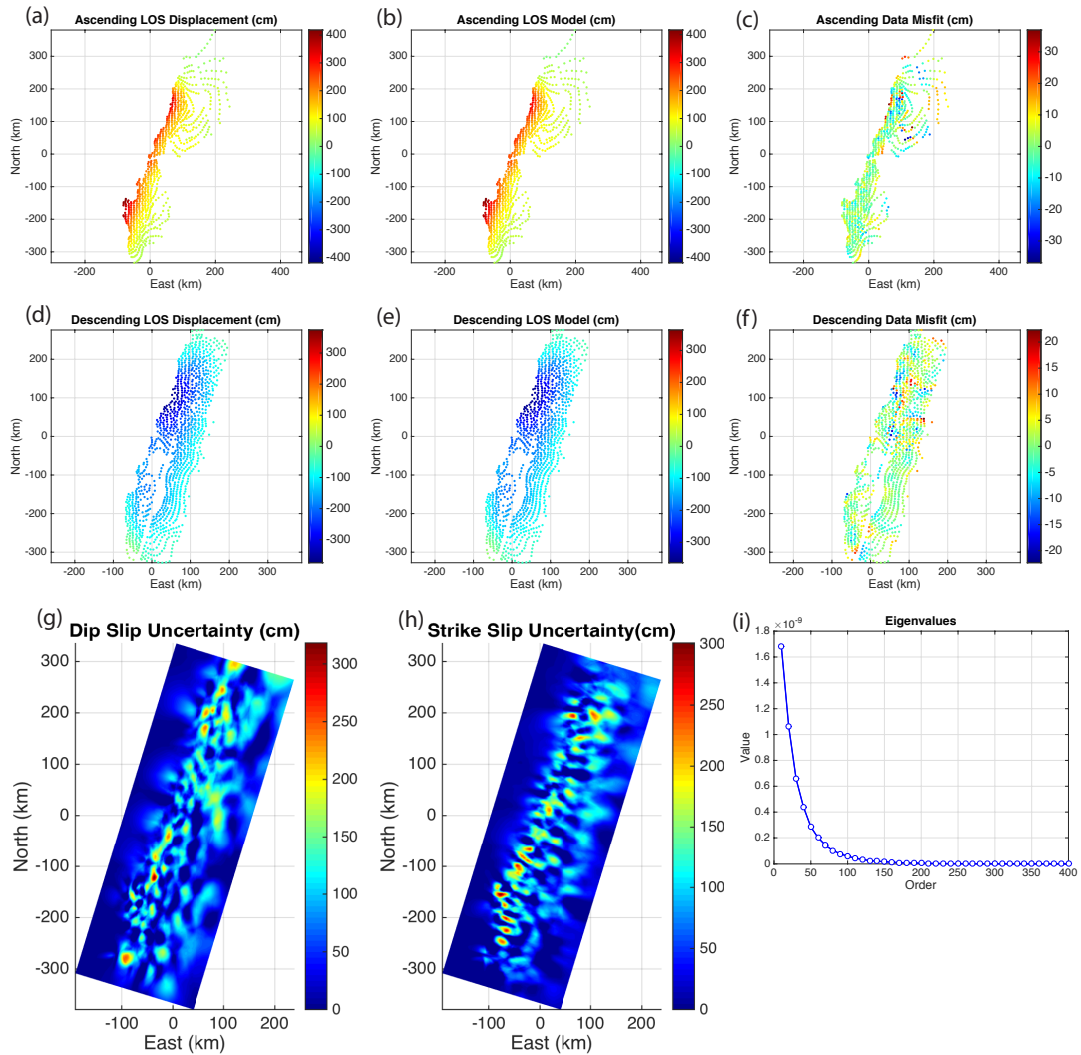
Figure S3.4: **Supplementary figures of the Maule earthquake inversion**. Plots (a), (b) and (c) are the subsampled data, forwarded model, and misfit for the ascending data for the 2010 Mw 8.8 Maule Earthquake. Plots (d), (e) and (f) are the subsampled data, forwarded model, and misfit for the descending data. (g) Uncertainty map for dip slip in Figure 4a. (h) Uncertainty map for strike slip in Figure 4b. (i) Eigenvalues vs. order.
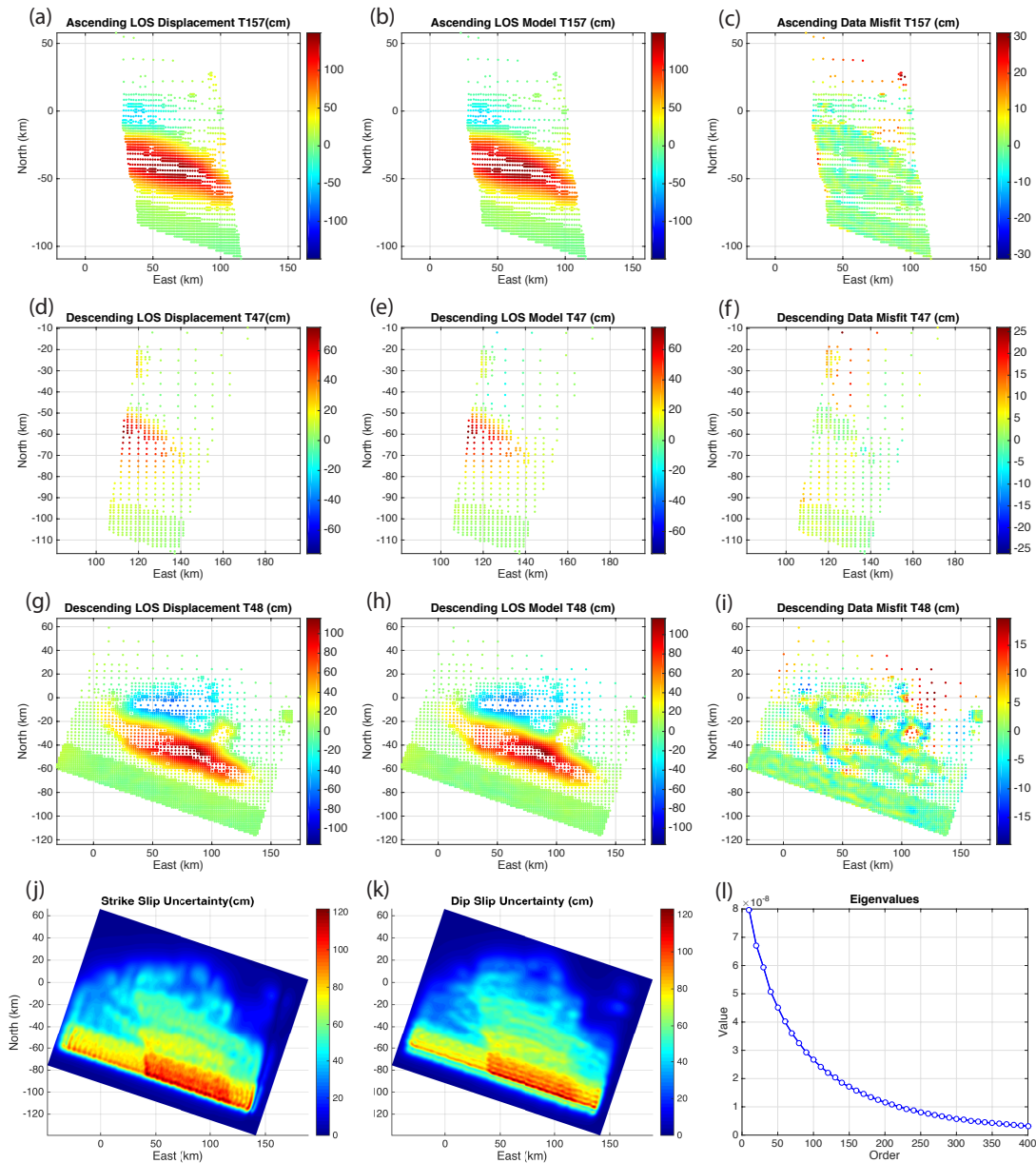
Figure S3.5: **Supplementary figures of the Grokha Nepal earthquake inversion**. Plots (a), (b) and (c) are the subsampled data, forwarded model, and misfit for the data from ALOS-2 ascending track 157 for the 2015 Mw 7.8 Nepal earthquake. Plots (d), (e) and (f) are the subsampled data, forwarded model, and misfit for the data from ALOS-2 descending track 47. Plots (g), (h) and (i) are the subsampled data, forwarded model, and misfit for the data from ALOS-2 descending track 48. (j) Uncertainty map for dip slip in Figure 5a. (k) is the uncertainty map for strike slip in Figure 5b. (l) Eigenvalues v. order.
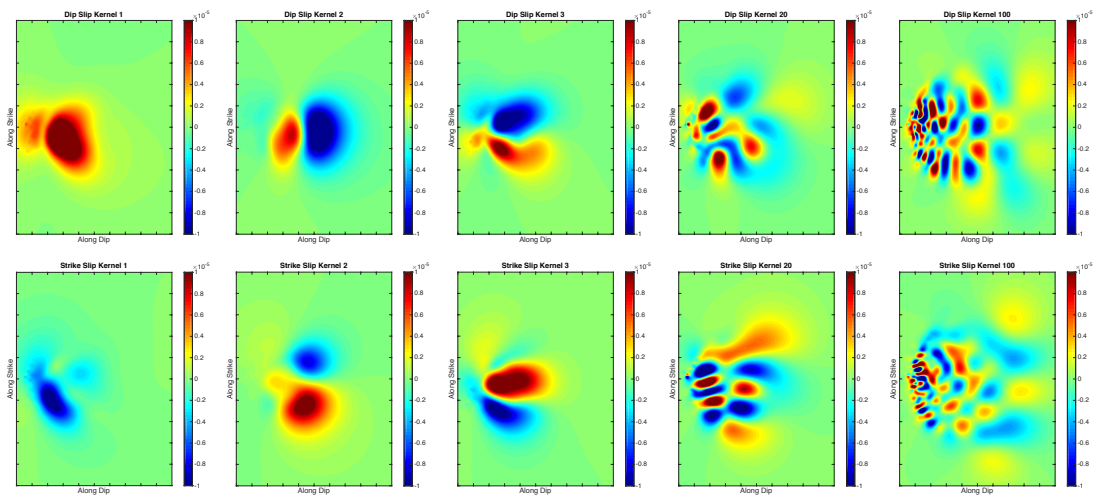
Figure S3.6: **Some examples of kernels for the 3-D test**. The upper row shows the dip slip kernels and the lower row shows the strike slip kernels. The wavelength of the kernel decreases as the order increases.
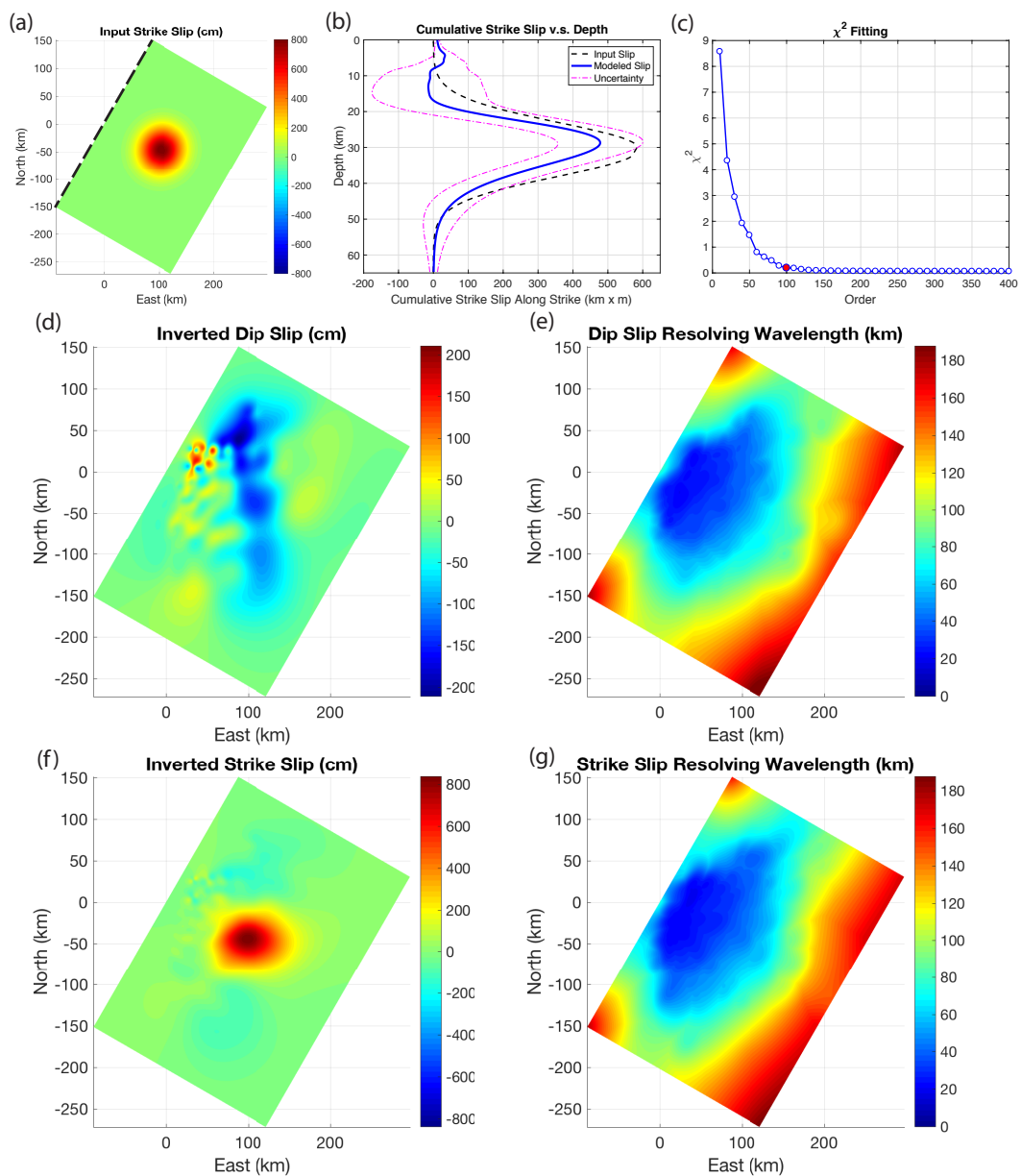
Figure S3.7: **3-D strike-slip test case**. (a) Input strike slip with the black dashed line denoting the fault trace. (b) Cumulative strike slip vs. depth with black dashed line being the input strike slip, blue line representing the inverted strike slip, and magenta dash-dot lines denoting the uncertainty. (c) Misfit vs. order with the red dot being the order selected. (d) Inverted dip slip and (f) inverted strike slip. Resolving wavelength for dip slip (e) and strike slip (g) constructed by the algorithm shown in Figure 3.2.
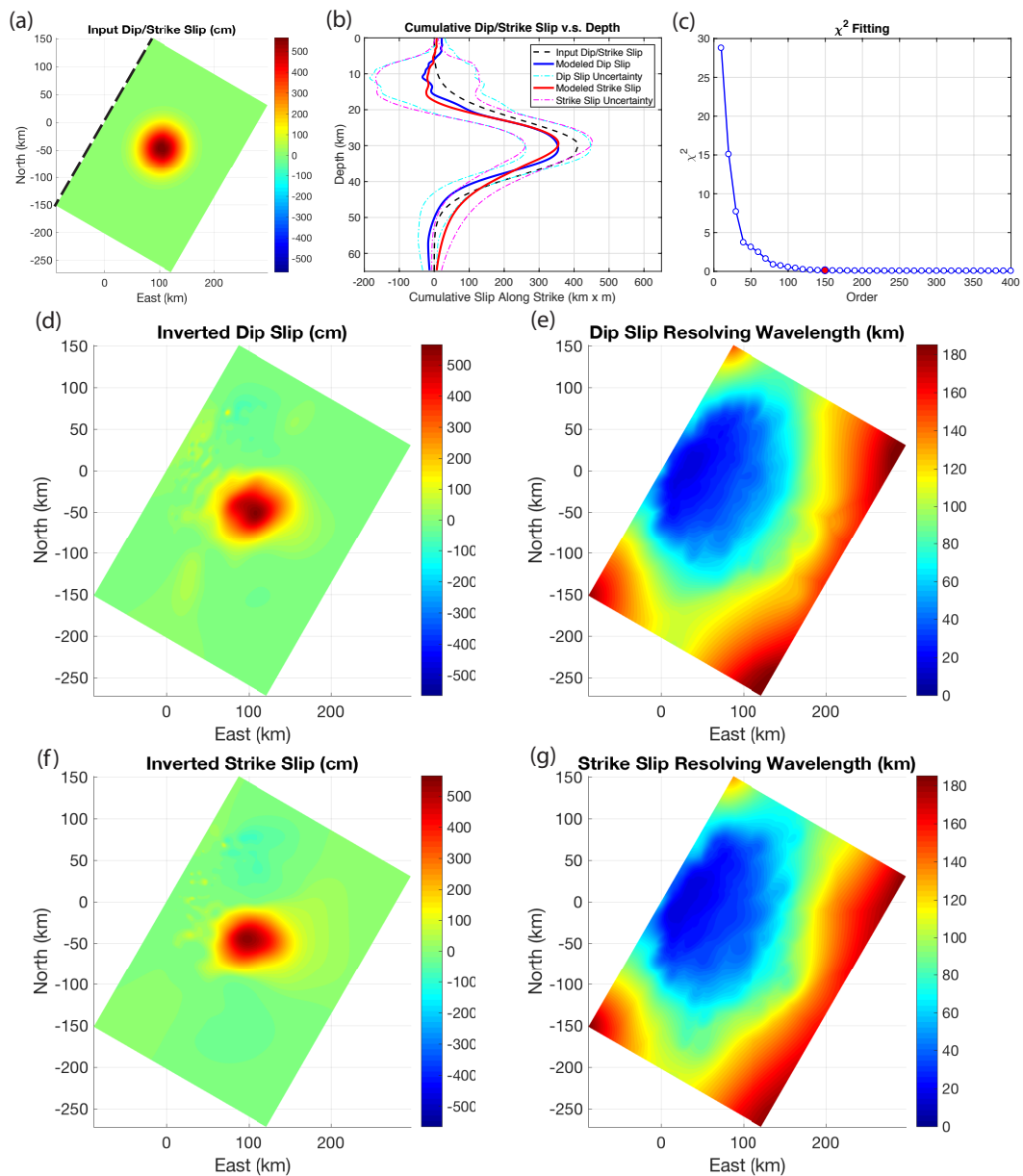
Figure S3.8: **3-D mixture of dip and strike slip test case**. (a) Input strike and dip slip (same amplitude) with the black dashed line denoting the fault trace. (b) Cumulative slip vs. depth plot with black dashed line being the input dip/strike slip, blue line representing the inverted dip slip and cyan dash-dot lines denoting the uncertainty, red line representing the inverted strike slip, and magenta dash-dot lines denoting the uncertainty. (c) Misfit vs. order with the red dot being the order selected. (d) Inverted dip slip and (f) inverted strike slip. Resolving wavelength for dip slip (e) and strike slip (g) constructed by the algorithm shown in Figure 3.2.

Chapter 4

Development on Sentinel TOPS data processing and it's application to the Cerro Prieto Geothermal Field

The Cerro Prieto Geothermal Field (CPGF) lies at the step-over between the Imperial and the Cerro Prieto Faults in northern Baja California, Mexico. While tectonically this is the most active section of the southern San Andreas Fault system, the spatial and temporal deformation in the area is poorly resolved by the sparse Global Positioning System (GPS) network coverage. Moreover, interferograms from satellite observations spanning more than a few months are decorrelated due to the extensive agricultural activity in this region. Here we investigate the use of frequent, short temporal baseline interferograms offered by the new Sentinel-1A satellite to recover two components of deformation time series across these faults. Following previous studies, we developed a purely geometric approach for image alignment that achieves better than 1/200 pixel alignment needed for accurate phase recovery. We construct InSAR time series using a coherence-based SBAS method with atmospheric corrections by means of common-

point stacking. We did not apply Enhanced Spectral Diversity (ESD) because the burst discontinuities are generally small (< 1.4 mm) and can be effectively captured during the atmospheric corrections. With these algorithms, the subsidence at CPGF is clearly resolved. The maximum subsidence rate of 160 mm/yr, due to extraction of geothermal fluids and heat, dominates the $\sim$40 mm/yr deformation across the proximal ends of the Imperial, the Cerro Prieto and the Indiviso Faults.

4.1   Introduction

The Cerro Prieto Geothermal Field (CPGF) is the second largest geothermal field in the world with an average annual net fluid extraction over 10 million tons. As a consequence, the surface subsides at an extraordinary rate despite the fact that the reservoir is deep and isolated from groundwater [Vasco et al. 2002]. Surrounding the CPGF, the fault system is complex. The northeast end of the CPGF connects to the Imperial fault while the southwest end reaches the Cerro Prieto fault. The Indiviso fault, where the 2010 El-Mayor Cucapah earthquake rupture took place, is only 15 km to the west [Gonzalez-Ortega et al. 2014]. Previous estimates of the subsidence rate at CPGF are up to 120-140 mm per year [Sarychikhina et al. 2011; Trugman, Borsa, and Sandwell 2014; Sarychikhina et al. 2015; Glowacka et al. 2010; Hanssen 2001], and the expected horizontal deformation across the Imperial fault and the Cerro Prieto fault is around 40 mm per year [Bennett, Rodi, and Reilinger 1996]. Tectonically, this is the most active zone of the southern San Andreas Fault system, but the spatial and temporal deformation for this area is poorly resolved. Part of the reason is the lack of Global Positioning System (GPS) data coverage, and the fact that observations from Interferometric Synthetic Aperture Radar (InSAR) are often biased due to the de-correlation introduced by extensive agricultural activity. (InSAR tutorial can be found in Simons and Rosen [2007],

Massonnet and Souyris [2008])

To overcome these challenges, we use SAR data from the C-band Sentinel-1A satellite operated by the European Space Agency (ESA). Sentinel-1A was launched on April 3rd, 2014, and has been in routine operation for about 2 years. The satellite is capable of revisiting a prioritized area (like CPGF) with every 12 days, primarily with a burst radar acquisition mode called Terrain Observation by Progressive Scan (TOPS). For other areas, the revisit time is usually 24 days. While the short revisit time is achieved by using TOPS mode, this new type of acquisition mode brings challenges to data processing. Following previous studies [Prats-Iraola et al. 2012; González et al. 2015], we developed a geometric alignment approach using post-processed precise orbits of Sentinel-1A ($\sim$50 mm along-track and $\sim$20-30 mm cross-track [Fernández et al. 2015]). We performed a systematic analysis to test the capabilities of this dataset, and used coherence-based SBAS [Tong and Schmidt 2016] and atmospheric correction with common-point stacking [Tymofyeyeva and Fialko 2015] to calculate the deformation time series around CPGF. The potential burst discontinuities caused by miss-registration along azimuth were handled during the atmospheric correction step instead of directly applying Enhanced Spectral Diversity (ESD) after geometric alignment, taking advantage of the errors being randomly distributed in time. With these algorithms, the maximum subsidence velocity at the CPGF is clearly resolved $\sim$160 mm/yr and the tectonic deformation rate across this region is $\sim$40 mm/yr.

4.2 Sentinel-1 TOPS Processing

The Sentinel-1 mission was designed to acquire frequent observations (12 or 24 days) with Interferometric Wide Swath ($\sim$250 km) product using TOPS mode [Torres

et al. 2012]. Unlike conventional ScanSAR, which illuminates the ground with a series of separated bursts, the TOPS mode SAR system rotates its antenna during the observation of each burst. While this type of observation reduces the along-track amplitude scalloping (signal-to-noise ratio change), it also introduces azimuthally-varying Doppler centroid [Prats-Iraola et al. 2012]. The Doppler centroid variation ($\sim$4.5kHz) wraps the satellite Pulse Repetition Frequency (PRF $\sim$486 Hz) 9 times (Figure 4.1). Due to this feature, the azimuth miss-registration error has to be better than 1/200th of a pixel (i.e. 66 mm) to keep the phase difference at burst boundaries to less than 1.4 mm. Note that standard image cross correlation methods only achieve $\sim$1/10 pixel accuracy, which would result in an unacceptably large phase mismatch of 28 mm at burst boundaries [De Zan 2014]. Moreover, the extra Doppler centroid goes beyond the Nyquist frequency, so accurate interpolation of the slave image into the master coordinates is not possible without de-ramping the slave, as discussed in [Miranda and Meadows 2015].

We have implemented a robust co-registration method based on the geometric approach and optional enhanced spectral diversity (ESD) described in previous studies [Sansosti et al. 2006; Yague-Martinez, De Zan, and Prats-Iraola 2017]. The code is available as a new pre-processing module in GMTSAR (`http://gmt.soest.hawaii.edu/projects/gmt5sar`). The pre-processing starts with a pixel-wise estimate of range and azimuth offsets using precise orbits and a downsampled ($\sim$360 m) Digital Elevation Model (DEM), which covers the region of the Single Look Complex (SLC) satellite images (step 1 in Figure 4.2). The precise orbit is used to back-project each pixel in the DEM (lon, lat, ellipsoidal height) into the range and azimuth coordinates of the master and slave images . The algorithm first uses a golden section search method [Press 1992] to quickly find the closest point at the PRF sampling ($\sim$14.5 m along-track) between the orbital trajectory and the topography pixel. Then a polynomial refinement algorithm is used to

improve the numerical accuracy to better than 10 mm in the azimuth coordinate. The range coordinate is the range between the antenna and the topography pixel evaluated at the corresponding azimuth coordinate. Note that the range-rate or Doppler is zero at this closest point. (A correction for alignment to a non-zero Doppler is discussed in the GMTSAR documentation [Sandwell et al. 2011].) The differences between the range and azimuth of the slave image with respect to the master image are used to construct a dense look-up map of range and azimuth shifts, using a surfacing technique described in [Smith and Wessel 1990]. After these maps are generated, the co-registration is done pixel-wise, which accounts for topography variation across the full image.

The second step in the processing is to resample the slave image into the coordinates of the master image (step 2 in Figure 4.2). Prior to resampling with a 2-D sync function, the slave image is de-ramped and demodulated following the algorithm in Miranda and Meadows [2015]. Best results are achieved if the de-ramping and re-ramping are only performed on slave image, leaving the master image unchanged. Using this approach, any possible inaccuracies in the de-ramping function will introduce no error because each slave is re-ramped using the conjugate of the original de-ramp function plus an appropriate phase shift related to the azimuth shift. De-ramping, interpolation, and re-ramping are performed burst by burst, after which all bursts within one sub-swath are stitched to generate one aligned SLC image.

The third (optional) step in the processing is to use the ESD approach to refine the overall azimuth shift . This follows the method described in previous studies [De Zan et al. 2014; Yague-Martinez, De Zan, and Prats-Iraola 2017]. The burst overlap areas are extracted from the aligned master and slave SLCs and a double-difference interferogram is formed. Azimuth filtering is used to estimate phase, after which the coherence and the

median of the phase for all the burst overlaps are used to estimate the phase shift using equation S1. ESD estimation is available in GMTSAR, so the user can decide when it is needed. The advantages and disadvantages of using ESD are discussed below.

The final step is to use any pair of aligned slave images to form an interferogram. We de-burst the SLCs by removing $1/2$ of the lines along the lower overlap zone of the first burst and $1/2$ of the lines along the upper overlap zone of the second burst, and abut the lines to form continuous SLC files. The full resolution DEM, mapped into the range and azimuth coordinates of the reference image, is used to form a full-resolution interferogram with the topographic contribution removed. At this point, the user can decide on the type of spatial filter used to estimate phase, coherence, and amplitude. In the examples below, we use a Gaussian filter with a 0.5 gain at a wavelength of 300 m in azimuth and ground range. The interferometric products are sampled at $1/4$ of the filter wavelength or smaller (<75m). Each subswath is processed independently and then stitched in radar coordinates. Phase unwrapping is performed in radar coordinates. The results presented below were geocoded at 4 arc-seconds resolution.

The only significant differences between this approach and the approach described in [Yague-Martinez, De Zan, and Prats-Iraola 2017] are that we do not perform common-band filtering in range or azimuth, and we use geometric alignment instead of patch cross correlation in range. We have tested both range alignment approaches and find that they work equally well. One potential advantage of the geometric range alignment approach is that it provides a pixel-wise topographically-dependent range shift, but that is only needed when the baseline approaches a large fraction of the critical baseline, which does not happen for Sentinel-1 satellites.

There are two important advantages to this pure geometric co-registration approach. The first is that it does not require any phase coherence between the master and slave images. This will become increasingly important as the time separation between the master and the newly acquired slaves increases beyond several years. The second advantage is that after each slave is aligned to the same single master image, interferograms can be constructed from any two images in the set without needing further co-registration. This is confirmed below and in the supplementary material (Figure S4.3, S4.6), where we show that the sum of the phase of interferograms in closed circuits is zero to within the phase noise of the radar. This enables the construction of long deformation time series from short timespan interferograms. Moreover, this greatly improves the efficiency in data processing since all images need only be aligned once to a single master.

After point-by-point geometric co-registration, the typical discontinuity between bursts is 1/400th of pixel (Table S4.1). Larger burst discontinuities are occasionally visible but they are not a constant azimuth shift at all the burst boundaries as expected [Scheiber et al. 2015; De Zan et al. 2014]. These burst discontinuities are potentially due to spatial variations in the ionosphere or clock error on certain bursts [Fattahi, Agram, and Simons 2017; Gomba, González, and De Zan 2017].

To illustrate the accuracy of the geometric alignment as well as the subswath-to-subswath fidelity of the Sentinel-1 radar, we show a typical TOPS-mode interferogram (i.e., 3 sub-swaths) combined in geo-coordinates, which covers a very large area ($\sim$250 km cross-track, $\sim$750 km along-track), from the Sierra Nevada Mountains across the Central Valley to the beach at Santa Barbara (Figure 4.3). The acquisitions come from relative orbit number (track) 144 on date 07/06/2015 and 07/30/2015. The interferogram was processed with pure geometric alignment/co-registration and no extra adjustment

from enhanced spectral diversity (ESD - [Prats-Iraola et al. 2012]). Within this large area, the phase is visually continuous across burst and sub-swath boundaries. When observed at such a large scale, it is clear that the interferogram contains a significant amount of atmospheric noise, some of which is strongly correlated with topography. Also, even though the time-span of the interferogram is only 24 days, there is already some de-correlation around the farms in the Central Valley.

4.3   Estimation of InSAR Time Series at the CPGF

To investigate the evolution of the subsidence at CPGF, and the spatial and temporal deformation across the nearby faults, we processed interferometric synthetic aperture radar data from the Sentinel 1-A satellite spanning the period from October 2014 to July 2016. The satellite collected 42 acquisitions on descending track 173 and 36 acquisitions on ascending track 166. We constructed 201 interferograms from the descending scenes and 183 from the ascending scenes, with a 90-day temporal threshold and a 200-meter perpendicular baseline threshold (Figure 4.4, Figure S4.2). We did not use the ESD method [Prats-Iraola et al. 2012], because the phase discontinuities at burst boundaries were much smaller than the atmospheric phase contributions (Table S4.1, Figures S4.3 and S4.4), and could be effectively removed along with the atmospheric signals as described below. To confirm that ESD is not needed, we also performed the analysis using ESD and compared the results (Figure S4.8). The differences in average velocity are generally less than 1 mm/yr. C-band data from synthetic aperture radar (SAR) observations are strongly decorrelated by agricultural activity or existence of vegetation over this region [Wei and Sandwell 2010]. The short 90-day temporal threshold was set in order to mitigate this effect, and also resolve seasonal changes in time series.

4.3.1 Circuit Test

To further illustrate the accuracy of the geometric alignment, as well as the accuracy of the calculation of the interferometric baselines, we performed a circuit test for track 173 by summing up interferograms along the dashed lines shown in Figure 4.4. The circuit had two segments. The time-increasing segment was the sum of 21 interferograms from 10/29/2014 to 07/26/2016, as shown with dashed blue lines in Figure 4.4. The time-decreasing segment spanned the same time interval, and is shown by the dashed red lines in Figure 4.4. Theoretically, the sum around this circuit should be zero except for possible phase noise due to decorrelation. The results are shown in Figure 4.5, where the phase and coherence of the direct 2-year interferogram are compared with the sum of 21 interferograms over the same time span. While the phase from a direct interferogram and the summed interferograms share similar features, the coherences are very different. The average coherence of the 21 interferograms is significantly higher than the coherence of the direct 2-year interferogram. This provides improved phase recovery of the summed interferogram with respect to the direct interferogram. The closure test (Figure 4.5f, Figure S4.6) produces a very small phase residual (median of 0.013 mm, median absolute deviation of 0.97 mm), considering that we are summing up 42 interferograms spanning 4 years. This indicates the error introduced from data processing is small for deformation signals greater than $\sim$1 mm/4yrs.

4.3.2 Atmospheric Correction and SBAS

The main objective of this analysis is to compute displacement time series for each of the ascending and descending stacks of SAR images to an accuracy of a few mm/yr, in order to better constrain the interseismic deformation of the region. Because atmospheric and ionospheric phase delays, as well as orbital and clock errors, are

sometimes much greater than the ground deformation signal, we use the high redundancy of the interferograms to estimate and remove these errors. This is done in combination with SBAS time series estimation using an iterative approach described in [Tymofyeyeva and Fialko 2015]. They note that the phase of each interferogram can be decomposed into the following terms

$$\Delta\phi_{ij} = \Delta\tau_{ij} + \alpha_j - \alpha_i + \varepsilon_{ij} \tag{4.1}$$

where τ is the deformation signal (steady in time), α is the phase error (turbulent in time) in each SAR image, and ε represents other errors, such as an inaccurate DEM or antenna noise. These α-related errors can be estimated and removed by means of common-point stacking, assuming they are randomly distributed in time. One important advantage of this stacking method is that it will capture the miss-registration errors at the same time, as they are also random in time. Together with this error correction, we applied a coherence-based small baseline subset (SBAS) method to compute time series for the CPGF region [González and Fernandez 2011; Marotti et al. 2012; Tong and Schmidt 2016]. Instead of omitting low coherence pixels, this algorithm solves for the time series at every pixel while taking in coherence as weights [Rosen et al. 2000] for the least squares problem. The short revisit times of the Sentinel-1A satellite, combined with the coherence-based SBAS, help mitigate strong de-correlation in this area.

4.3.3 Velocity and Displacement Time Series

The mean line-of-sight (LOS) velocity acquired for each track is shown in Figure 4.6. Since there is no good quality GPS model for the region [Sandwell et al. 2016] to provide large spatial scale control on the InSAR data, we selected a point far from faults on the North America plate and set its displacement to zero for every interferogram; this provides a reference point for all other pixels. Note that this does not violate the

closure test that is the preset rule for error estimation by common-point stacking. The displacement time series and atmospheric corrections for each epoch are provided in the supplementary material (Figure S4.3 and Figure S4.4). The maximum observed LOS velocity of the subsiding region is -168mm/yr for track 173 and -157 mm/yr for track 166. The boundaries of the subsidence are well defined in LOS velocity map and the overall subsidence rate increases toward the east from the Cerro Prieto fault to the Imperial fault. More interestingly, the eastern margin of the subsidence terminates at the southern end of the Imperial fault, which may indicate that the fault acts as a barrier to subsurface fluid flow.

We decomposed the two LOS velocity maps into fault-parallel horizontal velocity and vertical velocity, by assuming the average fault azimuth to be N36.5^z∘W [Lindsey et al. 2014]. The estimated maximum vertical subsidence is 163 mm/yr and the horizontal motion from east to west (over the mapped area) is roughly 40 mm/yr, in agreement with the overall change in velocity across these fault systems [Bennett, Rodi, and Reilinger 1996]. The large vertical deformation in the region of the CPGF is caused by removal of geothermal fluids [Glowacka et al. 2010]. If the CPGF were modeled by deflating Mogi source(s) one would expect significant horizontal motions in a direction pointing to the region of maximum subsidence (e.g., [Segall 2010]). Therefore our fault-parallel decomposition is not valid in this region and the original LOS data should be used for inverting for the Mogi sources [Trugman, Borsa, and Sandwell 2014]. In addition to the subsidence of the CPGF, we also observe significant subsidence at Heber geothermal field (black circle in Figure 4.6a), although the maximum LOS velocity here is smaller, only around -60 mm/yr.

As mentioned in Section 4.2, there is usually a small phase offset (< 1.4 mm)

between bursts. We do not correct for this offset because it has the same temporal characteristics as the atmospheric delay, in that it is common in interferograms that share an acquisition date and random in time. Therefore, we use the common-point stacking approach [Tymofyeyeva and Fialko 2015] to magnify, estimate, and remove the burst offsets together with the atmospheric noise. Figure 4.7 shows the estimated error on 04/24/2015 from the time series calculated for descending track 173. The uncorrected deformation map (Figure 4.7, left) is contaminated by an atmospheric delay having the characteristic pattern as a lee-wave [Vachon, Johannessen, and Johannessen 1994]. Also, there are small burst discontinuities around azimuth line 2700 and 4100. These features are absorbed into the estimated error (Figure 4.7, center). After applying the correction, the deformation time series are considerably flatter (Figure 4.7, right). A full comparison for track 173 can be found in Movie S1, where the uncorrected time series is more turbulent in time and the corrected is much cleaner. It also brought our attention that, during this study, the assumption that the atmosphere is equally strong across the full scene is occasionally biased by topographical barriers. When different sources of atmospheric signal come in to the same scene, the stronger one will potentially dominate the atmospheric correction sequence, thus a prioritized area (usually your area of interest) needs to be selected ahead to avoid such situation. Figure 4.8 shows the corrected and uncorrected LOS displacement time series at the CPGF. The corrected time series are very clean, while the uncorrected time series are quite noisy, even though they were computed with the same smoothness parameter using coherence based SBAS [Tong and Schmidt 2016].

4.3.4 Comparison with GPS Data

Over the past six years, we have deployed two linear GPS arrays across the Imperial and Cerro Prieto faults to better characterize their velocity gradient. The monuments consist of stainless steel couplers cemented into massive concrete structures. The GPS antennas are screwed directly into the couplers for accurate and rapid deployment. To obtain the GPS position estimates we used GAMIT/GLOBK software [Herring, King, and McClusky 2008] in ITRF2008 reference frame [Altamimi, Collilieux, and Métivier 2011]. Site velocities were computed by least squares linear fitting to time variation of coordinates for each station and then rotated with respect to Stable North America Reference Frame (SNARF) [Blewitt et al. 2005]. Velocity uncertainties are estimated within 1-sigma confidence level [Herring 2003]. We extracted fault-parallel velocity along two traces to compare with InSAR data. The extracted InSAR velocity is the mean value over 10x10-pixel ($\sim$180m260m) boxes along A-A' and B-B' traces shown in Figure 4.6d, taking the standard deviation as the measurement uncertainty. The InSAR velocity is shifted to match the GPS, because during InSAR data processing, the point pinned to zero is not essentially zero if measured with GPS under North America fixed reference frame. The A-A' trace is not extracted exactly along the GPS locations because these areas are not well correlated. However, the comparison shows good agreement across the Imperial Fault with an overall $\sim$30 mm/yr deformation across the fault (Figure 4.9a). The fast increase toward the western end suggests there is a hidden fault, as pointed out by [Lindsey and Fialko 2016], or possibly this sharp curve is biased by the subsidence signal from the nearby Heber geothermal field. The comparison also shows good agreement across the western side of the Cerro Prieto fault but poorer agreement on the eastern side. The InSAR measurements in this eastern area were extracted slightly south of the GPS line in the Colorado River valley where the correlation is the best. The InSAR to GPS differences in this region may be may be due to seasonal hydrologic signals, which

would contaminate the frequent InSAR acquisitions, but would not be resolved by the less frequent GPS measurements. If we combine the GPS and InSAR data, the estimated deformation from east to west along B-B' is close to 40 mm/yr, with a larger portion going across the Indiviso fault than the Cerro Prieto fault. The higher deformation rate over Indiviso fault may reflect continued postseismic deformation following the 2010 El-Mayor Cucapah earthquake [Gonzalez-Ortega et al. 2014].

4.4   Discussion and Conclusions

We demonstrate a pure geometric algorithm for InSAR processing of TOPS data from the Sentinel-1A satellite. The accurate orbits and software result in phase differences at burst boundaries of generally less than 1.4 mm. Since this error is far smaller than the atmospheric phase delays and could be associated with azimuthal misalignment, ionospheric variations, or true ground motion, we propose that the enhanced spectral diversity method for tuning the azimuth alignment is not needed. Moreover, there are three significant advantages to pure geometric alignment with no ESD. First by aligning all repeat images to a single reference, circuit closure is guaranteed. This closure is required for common point stacking and long timespan SBAS time series. Second, long time series can be processed incrementally, so that when a new SAR image is added it can be geometrically aligned to the master image and interferograms can be constructed from any of the other images. Third, interseismic motion can produce a significant along-track shift that can be corrected using an accurate plate tectonic model rather than estimated with ESD. For example, consider a long time span interferogram of a stable plate interior that is moving at 40 mm/yr in the satellite azimuth direction with respect to the International Terrestrial Reference Frame. The satellite orbit is computed in this fixed reference frame so after a decade of plate motion the azimuth shift of 0.4 m will cause a

large burst mismatch of 8 mm. The coherence between the reference and repeat images may not be sufficient for accurate ESD, but since the tectonic motion is well known, an accurate azimuth shift can be applied during the processing. The main disadvantage to not performing ESD is that the small residual mismatch can lower the coherence at the burst boundaries [Shirzaei, Bürgmann, and Fielding 2017].

We demonstrate the combined accuracy of the Sentinel-1 radar and orbits as well as the GMTSAR software by performing a circuit sum of 42 interferograms. The circuit closes to less than 1 mm, which is much smaller than the atmospheric error. This accurate closure ensures that long time-span interferograms can be accurately constructed from SBAS analyses of redundant short time-span interferograms. This approach provides a means to extract interseismic motion in agricultural areas where 1- and 2-year interferograms are largely decorrelated.

We applied the method of pure geometric alignment, common-point stacking for error estimation, and coherence based SBAS to ascending (42) and descending (34) acquisitions in the region surrounding the CPGF. The error estimation technique works well due to the small baselines, short time-span, and regular cadence of Sentinel-1A satellite. The improved coverage facilitates the combination ascending and descending LOS mean velocity grids into vertical and fault-parallel grids. The fault-parallel estimates show adequate agreement with two dense GPS profiles across the Imperial and Cerro Prieto faults. This new analysis provides refined estimates of three important crustal deformation signals in the region. 1) We produce the first complete map of the area of high subsidence rate at the step-over between the Imperial and Cerro Prieto faults. The estimated subsidence rate is higher now ($\sim$160 mm/yr) than in the past (120-140 mm/yr). Considering that the CPGF is currently only 11 m above sea level, the region

will be at sea level in just 65 years if the current rate continues. 2) We show that the Imperial fault does not accommodate the full 40 mm/yr of strike slip motion across the region and there is significant deformation across unmapped faults in the western Mexicali valley and further to the west. 3) We observe that currently the Cerro Prieto fault accommodates less than half of the full plate motion. Our analysis shows significant motion across the Indiviso fault and faults further to the west. This could be continued near-field postseismic deformation following the 2010 El-Mayor Cucapah earthquake. These three crustal deformation signals will be more fully resolved in the next few years as the Sentinel-1B begins its systematic coverage of the region to complement the critical measurements from Sentinel-1A.

Acknowledgements

Chapter 4, in full, is a reprint of the material as it appears in Transactions on Geoscience and Remote Sensing: Xu, X., Sandwell, D.T., Tymofyeyeva, E., González-Ortega, A. and Tong, X., 2017, "Tectonic and Anthropogenic Deformation at the Cerro Prieto Geothermal Step-Over Revealed by Sentinel-1A InSAR", *IEEE Transactions on*

Geoscience and Remote Sensing. The dissertation author was the primary investigator and author of the paper.

References

Altamimi, Z., Collilieux, X., and Métivier, L. (2011). "ITRF2008: an improved solution of the international terrestrial reference frame". In: *Journal of Geodesy* 85.8, pp. 457–473.

Bennett, R. A., Rodi, W., and Reilinger, R. E. (1996). "Global Positioning System constraints on fault slip rates in southern California and northern Baja, Mexico". In: *Journal of Geophysical Research: Solid Earth* 101.B10, pp. 21943–21960.

Blewitt, G, Argus, D, Bennett, R, Bock, Y, Calais, E, Craymer, M, Davis, J, Dixon, T, Freymueller, J, Herring, T, Johnson, D, Larson, K, Miller, M, Sella, G, Snay, R, and M, T. (2005). "A stable North America reference frame (SNARF): First release". In: *Proceedings of the Joint UNAVCO/IRIS Workshop, Stevenson, WA, USA, June*, pp. 9–11.

De Zan, F. (2014). "Accuracy of incoherent speckle tracking for circular Gaussian signals". In: *IEEE Geoscience and Remote Sensing Letters* 11.1, pp. 264–267.

De Zan, F., Prats-Iraola, P., Scheiber, R., and Rucci, A. (2014). "Interferometry with TOPS: Coregistration and azimuth shifts". In: *EUSAR 2014; 10th European Conference on Synthetic Aperture Radar; Proceedings of.* VDE, pp. 1–4.

Fattahi, H., Agram, P., and Simons, M. (2017). "A network-based enhanced spectral diversity approach for TOPS time-series analysis". In: *IEEE Transactions on Geoscience and Remote Sensing* 55.2, pp. 777–786.

Fernández, J., Escobar, D., Peter, H., and Féménias, P. (2015). "COPERNICUS POD SERVICE OPERATIONS–ORBITAL ACCURACY OF SENTINEL-1A AND SENTINEL-2A". In: *Proc. Int. Symp. Space Flight Dyn*.

Glowacka, E., Sarychikhina, O., Suárez, F., Nava, F. A., and Mellors, R. (2010). "Anthropogenic subsidence in the Mexicali Valley, Baja California, Mexico, and slip on the Saltillo fault". In: *Environmental Earth Sciences* 59.7, pp. 1515–1524.

Gomba, G., González, F. R., and De Zan, F. (2017). "Ionospheric phase screen compensation for the Sentinel-1 TOPS and ALOS-2 ScanSAR modes". In: *IEEE Transactions on Geoscience and Remote Sensing* 55.1, pp. 223–235.

González, P. J. and Fernandez, J. (2011). "Error estimation in multitemporal InSAR deformation time series, with application to Lanzarote, Canary Islands". In: *Journal of Geophysical Research: Solid Earth* 116.B10.

González, P. J., Bagnardi, M., Hooper, A. J., Larsen, Y., Marinkovic, P., Samsonov, S. V., and Wright, T. J. (2015). "The 2014–2015 eruption of Fogo volcano: Geodetic modeling of Sentinel-1 TOPS interferometry". In: *Geophysical research letters* 42.21, pp. 9239–9246.

Gonzalez-Ortega, A., Fialko, Y., Sandwell, D., Alejandro Nava-Pichardo, F, Fletcher, J., Gonzalez-Garcia, J., Lipovsky, B., Floyd, M., and Funning, G. (2014). "El Mayor-Cucapah (Mw 7.2) earthquake: Early near-field postseismic deformation from InSAR and GPS observations". In: *Journal of Geophysical Research: Solid Earth* 119.2, pp. 1482–1497.

Hanssen, R. F. (2001). *Radar interferometry: data interpretation and error analysis*. Vol. 2. Springer Science & Business Media.

Herring, T., King, R., and McClusky, S. (2008). "Introduction to GAMIT/GLOBK, report, mass". In: *Institute of Technology, Cambridge*.

Herring, T. (2003). "MATLAB Tools for viewing GPS velocities and time series". In: *GPS solutions* 7.3, pp. 194–199.

Lindsey, E. O. and Fialko, Y. (2016). "Geodetic constraints on frictional properties and earthquake hazard in the Imperial Valley, southern California". In: *Journal of Geophysical Research: Solid Earth* 121.2, pp. 1097–1113.

Lindsey, E. O., Fialko, Y., Bock, Y., Sandwell, D. T., and Bilham, R. (2014). "Localized and distributed creep along the southern San Andreas Fault". In: *Journal of Geophysical Research: Solid Earth* 119.10, pp. 7909–7922.

Marotti, L., Prats, P., Scheiber, R., Wollstadt, S., and Reigber, A. (2012). "Differential SAR interferometry with TerraSAR-X TOPS data: Mexico city subsidence results". In: *Synthetic Aperture Radar, 2012. EUSAR. 9th European Conference on*. VDE, pp. 677–680.

Massonnet, D. and Souyris, J.-C. (2008). *Imaging with synthetic aperture radar*. CRC Press.

Miranda, N and Meadows, P. (2015). *Radiometric Calibration of S-1 Level-1 Products Generated by the S-1 IPF. Technical note*.

Prats-Iraola, P., Scheiber, R., Marotti, L., Wollstadt, S., and Reigber, A. (2012). "TOPS interferometry with TerraSAR-X". In: *IEEE Transactions on geoscience and remote sensing* 50.8, pp. 3179–3188.

Press, W. H. (1992). *The art of scientific computing*. Cambridge university press.

Rosen, P. A., Hensley, S., Joughin, I. R., Li, F. K., Madsen, S. N., Rodriguez, E., and Goldstein, R. M. (2000). "Synthetic aperture radar interferometry". In: *Proceedings of the IEEE* 88.3, pp. 333–382.

Sandwell, D., Mellors, R., Tong, X., Wei, M., and Wessel, P. (2011). "Open radar interferometry software for mapping surface deformation". In: *Eos, Transactions American Geophysical Union* 92.28, pp. 234–234.

Sandwell, D. T., Zeng, Y., Shen, Z.-K., Crowell, B., Murray, J., McCaffrey, R., and Xu, X. (2016). "The SCEC Community Geodetic Model V1: Horizontal Velocity Grid". In: *SCEC Annu. Meeting*.

Sansosti, E., Berardino, P., Manunta, M., Serafino, F., and Fornaro, G. (2006). "Geometrical SAR image registration". In: *IEEE Transactions on Geoscience and Remote Sensing* 44.10, pp. 2861–2870.

Sarychikhina, O., Glowacka, E., Mellors, R., and Vidal, F. S. (2011). "Land subsidence in the Cerro Prieto Geothermal Field, Baja California, Mexico, from 1994 to 2005: An integrated analysis of DInSAR, leveling and geological data". In: *Journal of Volcanology and Geothermal Research* 204.1, pp. 76–90.

Sarychikhina, O., Glowacka, E., Robles, B., Nava, F. A., and Guzmán, M. (2015). "Estimation of Seismic and Aseismic Deformation in Mexicali Valley, Baja California, Mexico, in the 2006–2009 Period, Using Precise Leveling, DInSAR, Geotechnical Instruments Data, and Modeling". In: *Pure and Applied Geophysics* 172.11, pp. 3139–3162.

Scheiber, R., Jäger, M., Prats-Iraola, P., De Zan, F., and Geudtner, D. (2015). "Speckle tracking and interferometric processing of TerraSAR-X TOPS data for mapping nonstationary scenarios". In: *IEEE Journal of Selected Topics in Applied Earth Observations and Remote Sensing* 8.4, pp. 1709–1720.

Segall, P. (2010). *Earthquake and volcano deformation*. Princeton University Press.

Shirzaei, M., Bürgmann, R., and Fielding, E. J. (2017). "Applicability of Sentinel-1 Terrain Observation by Progressive Scans multitemporal interferometry for monitoring slow ground motions in the San Francisco Bay Area". In: *Geophysical Research Letters* 44.6, pp. 2733–2742.

Simons, M and Rosen, P. (2007). "Interferometric synthetic aperture radar geodesy". In: *Treatise on Geophysics*.

Smith, W. and Wessel, P (1990). "Gridding with continuous curvature splines in tension". In: *Geophysics* 55.3, pp. 293–305.

Tong, X. and Schmidt, D. (2016). "Active movement of the Cascade landslide complex in Washington from a coherence-based InSAR time series method". In: *Remote Sensing of Environment* 186, pp. 405–415.

Torres, R., Snoeij, P., Geudtner, D., Bibby, D., Davidson, M., Attema, E., Potin, P., Rommen, B., Floury, N., Brown, M., Traver, I. N., Deghaye, P., Duesmann, B., Rosich, B., Miranda, N., Bruno, C., L'Abbate, M., Croci, R., Pietropaolo, A., Huchler, M., and Rostan, F. (2012). "GMES Sentinel-1 mission". In: *Remote Sensing of Environment* 120, pp. 9–24.

Trugman, D. T., Borsa, A. A., and Sandwell, D. T. (2014). "Did stresses from the Cerro Prieto Geothermal Field influence the El Mayor-Cucapah rupture sequence?" In: *Geophysical Research Letters* 41.24, pp. 8767–8774.

Tymofyeyeva, E. and Fialko, Y. (2015). "Mitigation of atmospheric phase delays in InSAR data, with application to the eastern California shear zone". In: *Journal of Geophysical Research: Solid Earth* 120.8, pp. 5952–5963.

Vachon, P., Johannessen, O. M., and Johannessen, J. A. (1994). "An ERS 1 synthetic aperture radar image of atmospheric lee waves". In: *Journal of Geophysical Research: Oceans* 99.C11, pp. 22483–22490.

Vasco, D., Wicks Jr, C., Karasaki, K., and Marques, O. (2002). "Geodetic imaging: reservoir monitoring using satellite interferometry". In: *Geophysical Journal International* 149.3, pp. 555–571.

Wei, M. and Sandwell, D. T. (2010). "Decorrelation of L-band and C-band interferometry over vegetated areas in California". In: *IEEE Transactions on Geoscience and Remote Sensing* 48.7, pp. 2942–2952.

Yague-Martinez, N., De Zan, F., and Prats-Iraola, P. (2017). "Coregistration of Interferometric Stacks of Sentinel-1 TOPS Data". In: *IEEE Geoscience and Remote Sensing Letters*.
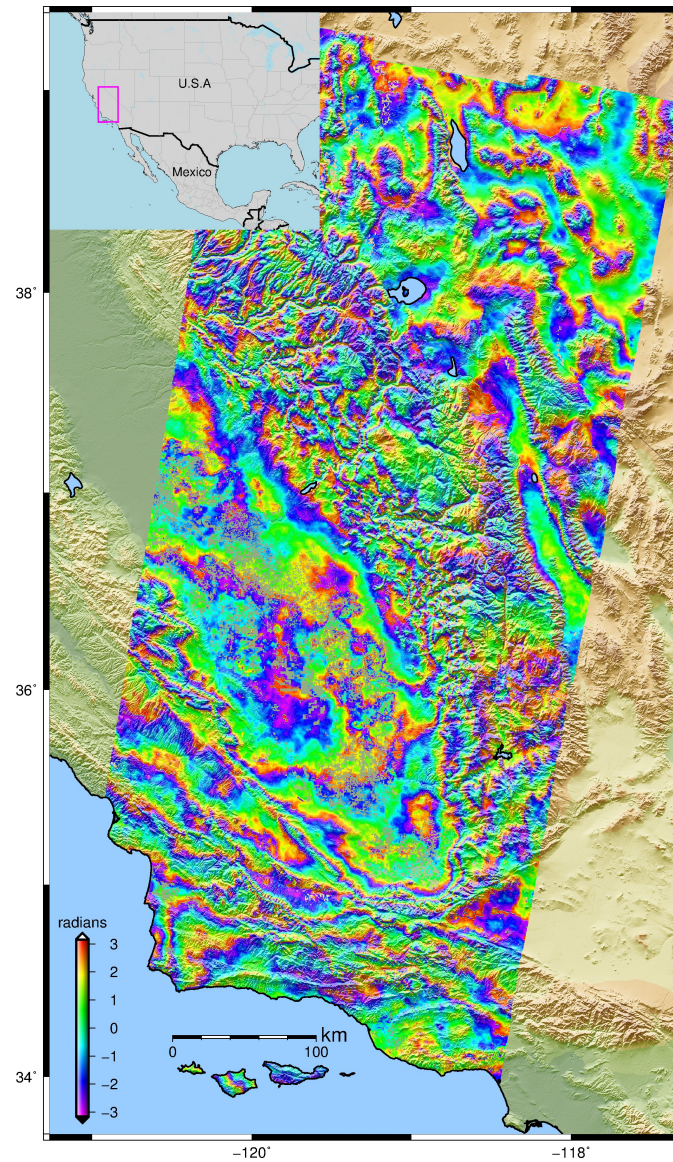
Figures
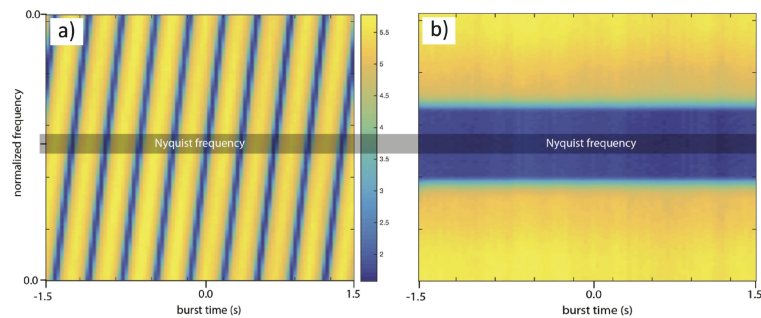
Figure 4.1: **Spectrogram of one burst of TOPS-mode data plotted on a log color scale.** (a) Original spectrogram of a single burst of TOPS data wraps around the Nyquist frequency 9 times. (b) Spectrogram after deramping has low power close to the Nyquist, which enables accurate resampling.
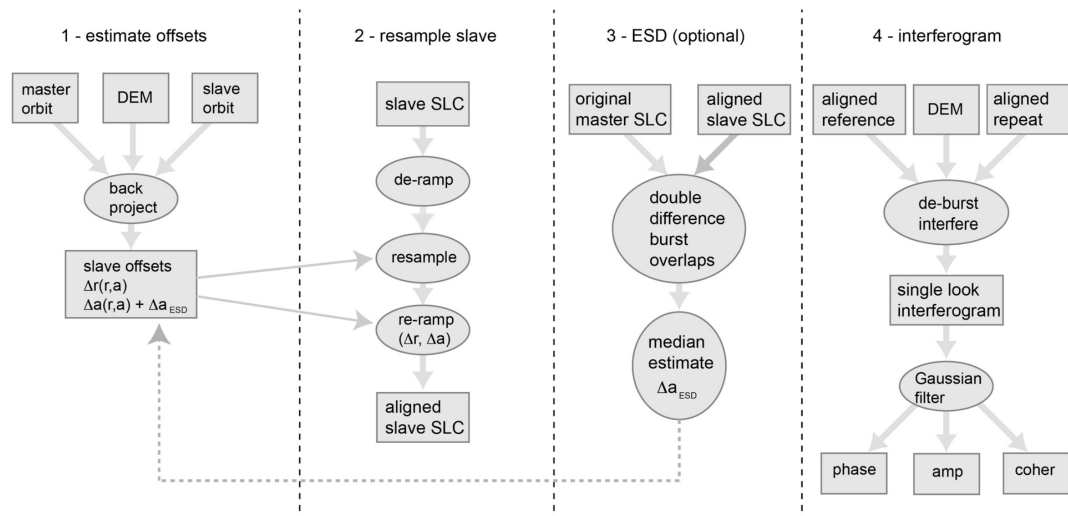

Figure 4.2: **Processing chain for TOPS data using precise orbits and point-by-point geometric co-registration.** The ESD algorithm is implemented in GMTSAR but not used in this study.

Figure 4.3: **An interferogram combining 3 sub-swaths (109 bursts) from track 144 of Sentinel-1A data, processed with GMTSAR with geometric alignment/coregistration.** No enhanced spectral diversity or swath-boundary adjustments were applied.
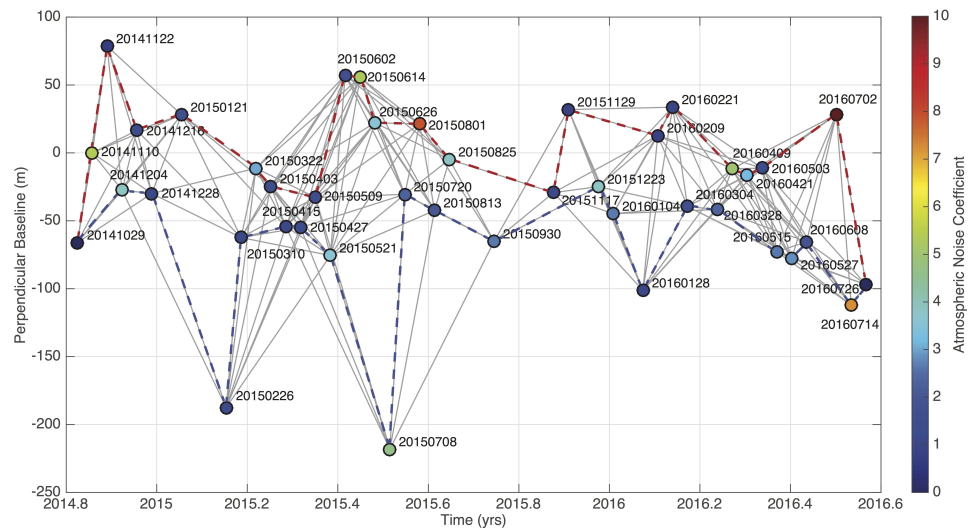
Figure 4.4: **Perpendicular baseline vs. time plot for track 173 over CPGF.** The dots represent acquisition dates and the grey lines denote interferometric pairs selected with a 200-meter baseline threshold and 90-day temporal threshold. The colors of the dots indicate the atmospheric noise coefficient (ANC) [Tymofyeyeva and Fialko 2015], with a larger value representing a stronger atmospheric noise contribution on that date. The red and blue dashed lines correspond to the interferograms used in the circuit test.
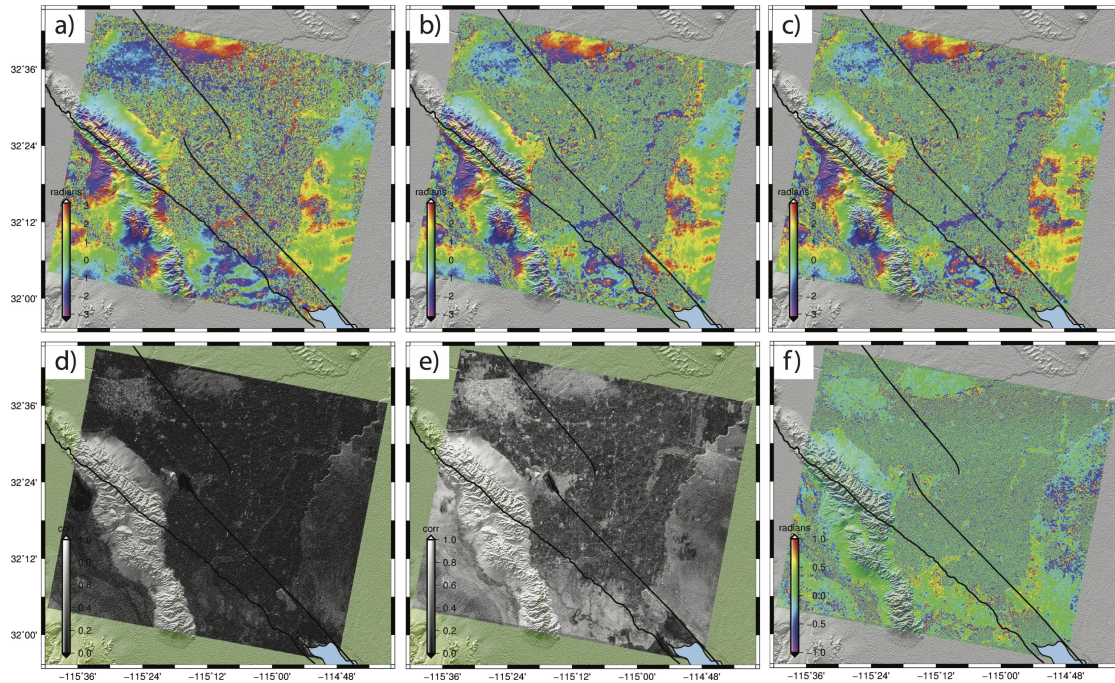
Figure 4.5: **Circuit test for the CPGF area on track 173.** a) is an interferogram connecting 10/29/2014 and 07/26/2016 with d) being its coherence. b) is the interferogram generated by adding up 21 interferograms following the red dashed line in Figure 4, with e) being their average coherence. c) is the interferogram generated by adding up 21 interferograms following the blue dashed line in Figure 4. f) is the phase residual when adding up 42 interferograms along the dashed line circuit (median of 0.013 mm, median absolute deviation of 0.97 mm). The black lines are the nearby faults provided by Centro de Investigación Científica y de Educación Superior de Ensenada (CICESE).
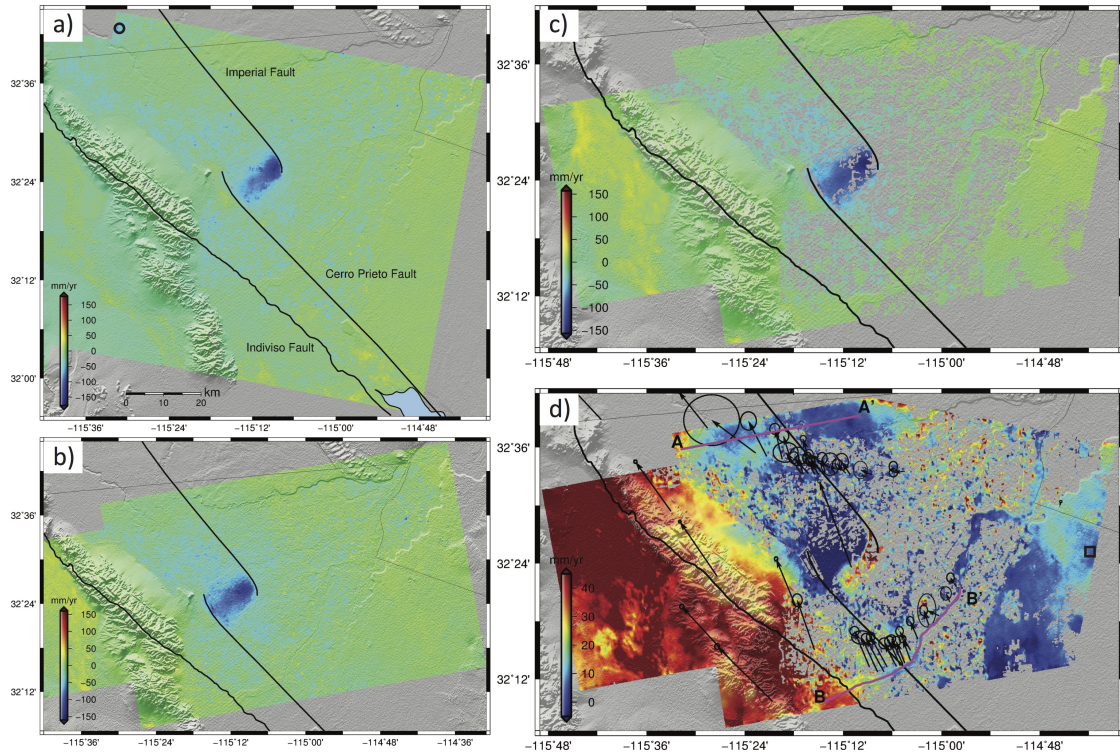
Figure 4.6: **Velocity map derived from analyzing 42 scenes, 201 interferograms (Figure 4) from descending track 173, and 34 scenes 183 interferograms (Figure S4.2) from ascending track 166.** a) is the line-of-sight (LOS) velocity map for track 173. b) is the LOS velocity map for track 166. c) and d) are the decomposed vertical velocity and fault parallel velocity following Lindsey et al. [2014], assuming the average fault azimuth to be N36.5°W. A 0.15 coherence threshold was used to mask the data projected. The black lines are the faults and black arrows are GPS survey mode data in North America fixed reference frame with circles denoting the uncertainty. The black circle in a) is the location of the Heber geothermal field and the black square in d) is the location we pinned down to zero in the SBAS processing.
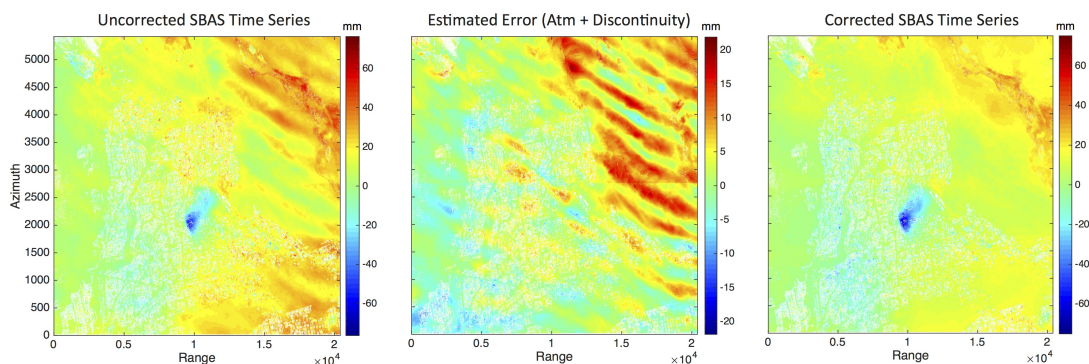
Figure 4.7: **Error reduction by common point stacking.** The plot on the left is the uncorrected displacement in radar coordinates on 04/27/2015 with respect to the first acquisition on 10/29/2014, estimated with coherence based SBAS for descending track 173. The middle plot is the error estimated by the common point stacking method [Tymofyeyeva and Fialko, 2015]. The plot on the right is the displacement acquired with coherence based SBAS after removing the estimated error from every interferograms.
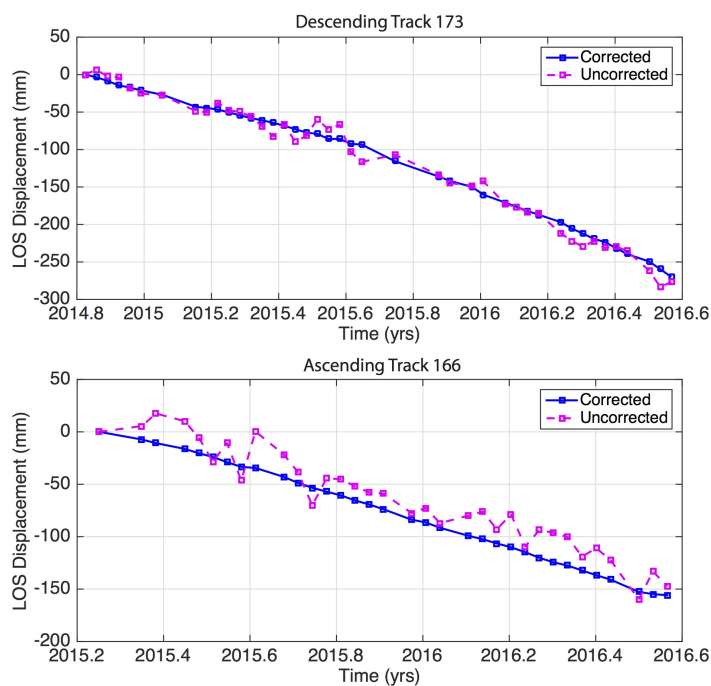
Figure 4.8: **LOS displacement time series at CPFG.** Top plot is the subsidence revealed by descending track 173, and the bottom plot is ascending track 166. The magenta dashed lines are the time series without the error correction from [Tymofyeyeva and Fialko, 2015], and the blue lines are the corrected time series. Both results used coherence based SBAS [Tong and Schmidt, 2016] with the same smoothing parameter.
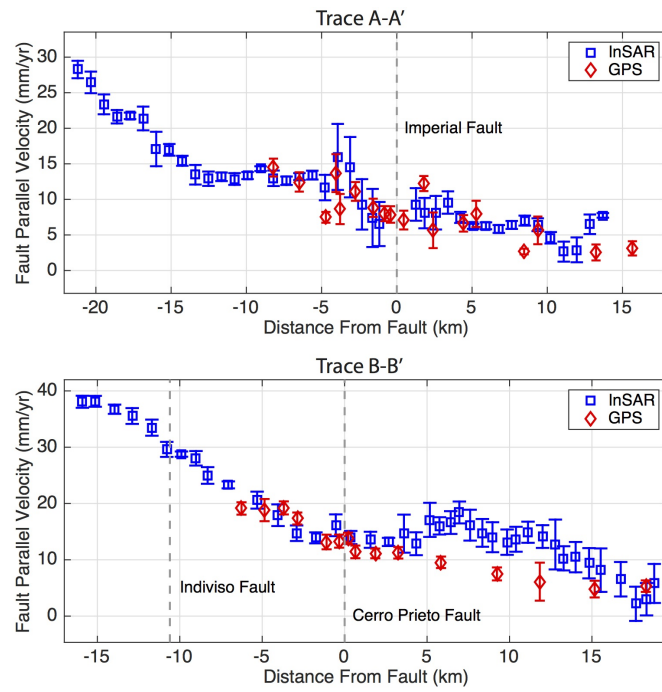
Figure 4.9: **Comparison between InSAR fault-parallel velocity map and GPS.** In-SAR velocity are extracted along the two magenta trace in Figure 6d. GPS data are projected to the fault parallel direction.

Supplements

Table S4.1: **Estimates of azimuth offset from track 173.**The last column is the estimate of median phase difference $\Delta\phi$ at the burst boundary for an interferogram between the master and slave. This is converted to an along-track azimuth shift Δa using the formula $\Delta a = PRF \frac{\Delta\phi}{2\pi(f_u - f_l)}$ where $(f_u - f_l)$ is the difference between the Doppler rate at the upper and lower edge of each burst ($\sim$4500 Hz) and the effective PRF is 486 Hz so keeping the phase mismatch below, for example, 0.54 radian (2.8 mm) requires azimuth alignment to 0.01 pixel accuracy.

Scene	Date	Δa pixels	$\Delta\phi$ (mm)
S1A20141029	2014301	-0.0002037	-0.0571
S1A20141110	2014313	master	master
S1A20141122	2014325	0.0009851	0.2758
S1A20141204	2014337	-0.0003378	-0.0946
S1A20141216	2014349	-4.64E-05	-0.013
S1A20141228	2014361	0.0008317	0.2329
S1A20150121	2015020	-0.0001029	-0.0288
S1A20150226	2015056	0.0043452	1.2167
S1A20150310	2015068	-0.0037625	-1.0535
S1A20150322	2015080	0.0058622	1.6414
S1A20150403	2015092	0.0009582	0.2683
S1A20150415	2015104	0.0004369	0.1224
S1A20150427	2015116	-0.005689	-1.5929
S1A20150509	2015128	0.0031756	0.8892
S1A20150521	2015140	-0.0027981	-0.7835
S1A20150602	2015152	-0.0002216	-0.0621
S1A20150614	2015164	-0.0021707	-0.6078
S1A20150626	2015176	0.004141	1.1595
S1A20150708	2015188	0.0035343	0.9896
S1A20150720	2015200	0.0009581	0.2683
S1A20150801	2015212	-0.0045896	-1.2851
S1A20150813	2015224	-0.0019004	-0.5321
S1A20150825	2015236	-0.0015675	-0.4389

Table S4.1: Estimates of azimuth offset from track 173, continued.

| Scene	Date	Δa pixels	$\Delta \phi$ (mm)
S1A20150930	2015272	0.0033381	0.9347
S1A20151117	2015320	4.21E-05	0.0118
S1A20151129	2015332	-0.0006378	-0.1786
S1A20151223	2015356	0.0002627	0.0736
S1A20160104	2016003	0.0018979	0.5314
S1A20160128	2016027	-7.53E-05	-0.0211
S1A20160209	2016039	-0.0054238	-1.5187
S1A20160221	2016051	0.001188	0.3327
S1A20160304	2016063	-0.0030715	-0.8600
S1A20160328	2016087	-0.0011519	-0.3225
S1A20160409	2016099	0.0017592	0.4926
S1A20160421	2016111	-0.0038621	-1.0814
S1A20160503	2016123	-0.0001058	-0.0296
S1A20160515	2016135	-0.0019231	-0.5385
S1A20160527	2016147	0.0021068	0.5899
S1A20160608	2016159	-0.0046403	-1.2993
S1A20160702	2016183	-0.0044538	-1.2471
S1A20160714	2016195	0.0040212	1.1260
S1A20160726	2016207	-0.0026054	-0.7295
S1A20141029	2014301	0.0009851	0.2758
S1A20141110	2014313	-0.0003377	-0.0946
minimum		-0.0056890	-1.5929
maximum		0.0058623	1.6414
std		0.0028599	0.8008
mad		0.0022351	0.6258
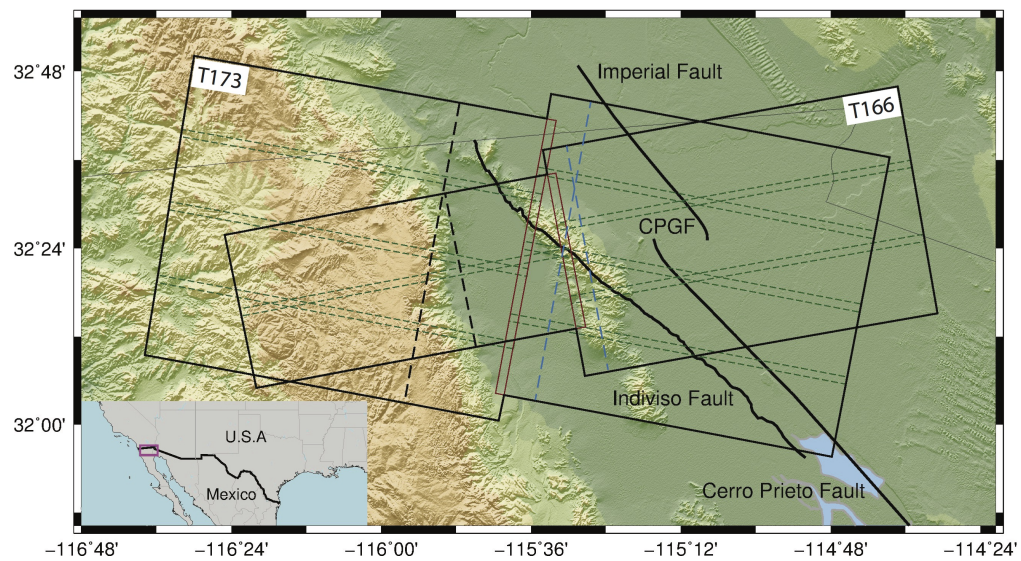
Figure S4.1: **Map showing the area of study and the nearby faults.** Thick black lines with labels are active faults mapped by USGS (http://earthquake.usgs.gov/hazards/qfaults/) and CICESE (http://www.cicese.edu.mx/). Black polygons show the footprint of Sentinel 1 InSAR data used by this study. The red rectangles denote the swath overlaps and the green dashed lines represent burst overlaps. The blue dashed lines are profiles used in Figure S4.6. The black dashed lines are the edges where we stop processing data in order to prevent atmospheric contamination from a different source. For both track 173 and track 166, subswath 1 and subswath 2 are used.
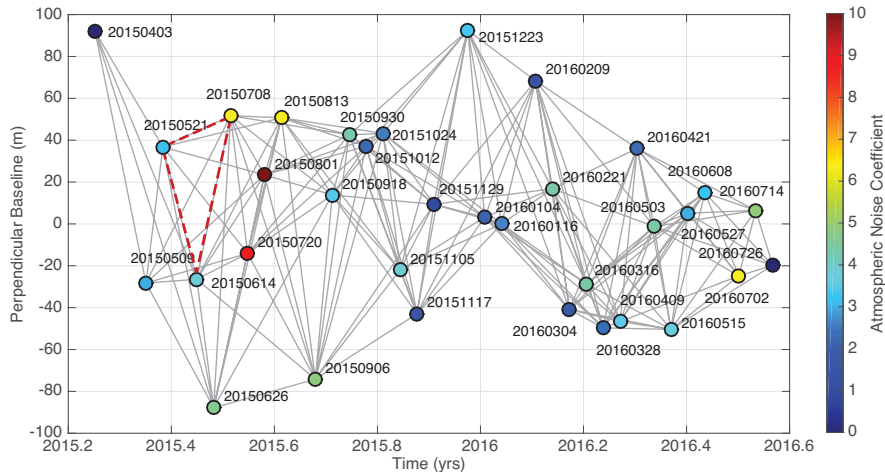
Figure S4.2: **Perpendicular baseline versus time for track 166 over CPGF**. The colored dots represent acquisition dates and the grey lines denote interferometric pairs selected with a 200-meter baseline threshold and 90-day temporal threshold. The colors of the dots indicate the atmospheric noise coefficient (ANC) [Tymofyeyeva and Fialko 2015], with a larger value representing a stronger atmospheric noise on that date. The first and the last acquisition are not estimated and are set to zero in the plots below. The red dashed line denotes the data used for shift parameter circuit closure test in Figure S4.1.
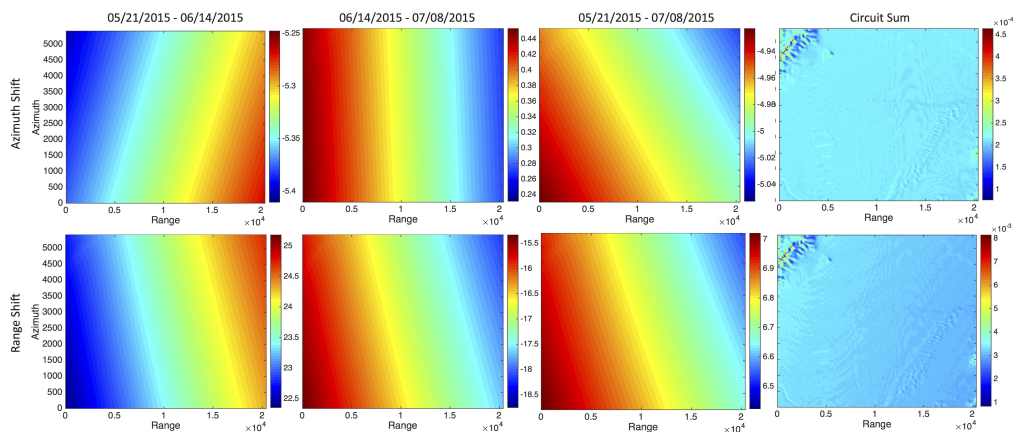
Figure S4.3: **Circuit closure test for point-by-point alignment**. The figures show the circuit tests for the azimuth grids (upper) and range grids (lower). The grids are very smooth and well approximated by a plane. The sum around the circuit is generally 2-3 orders of magnitude smaller than the original grids. This excellent closure implies that processing large stacks of interferograms will be very efficient because once all slave images are geometrically aligned with the master, well aligned interferograms can be formed between any two images.
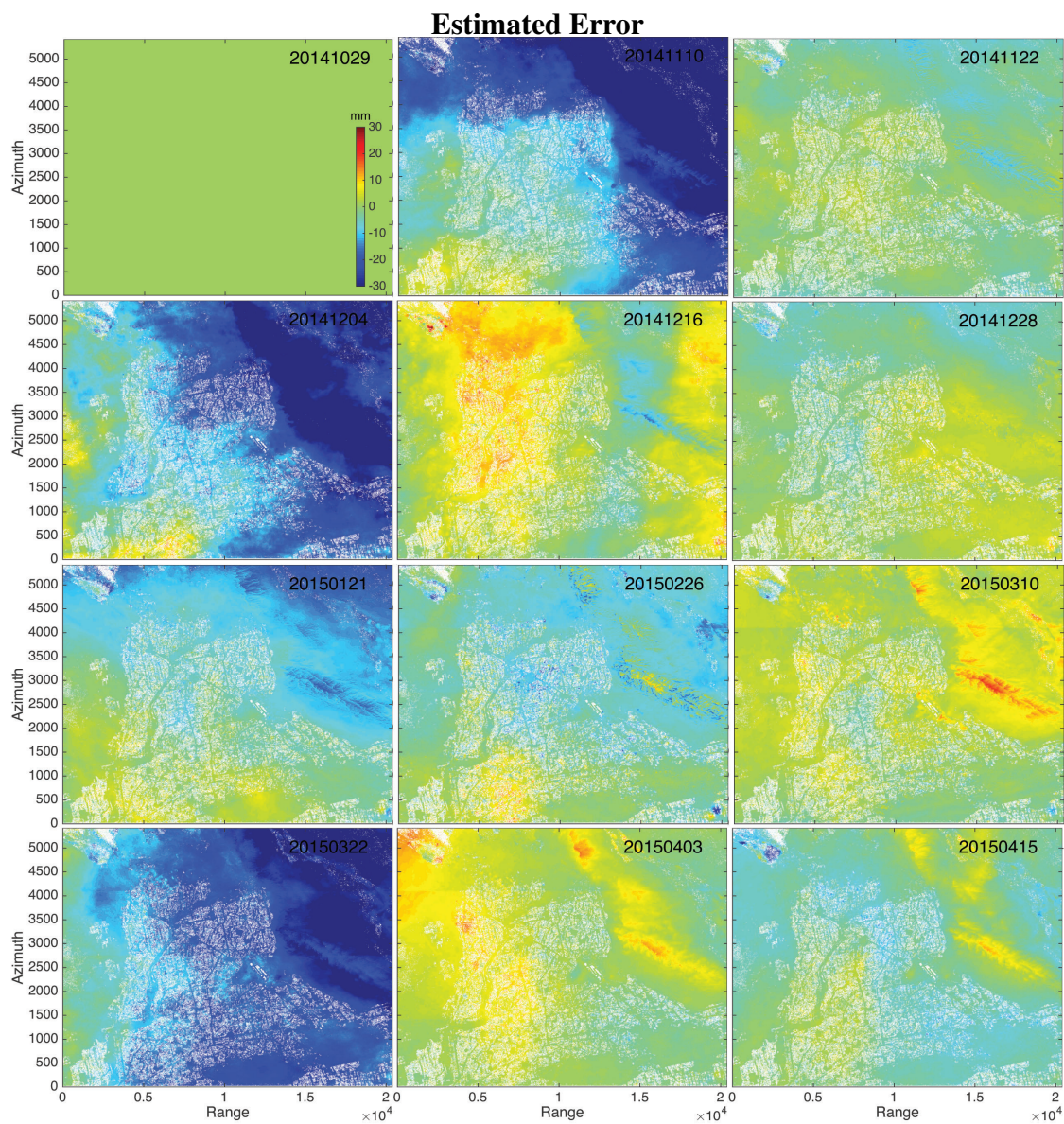
Figure S4.4: **Atmospheric phase screen and time series for track 173.** The plots are estimated atmosphere, ionospheric, orbit error, and clock error followed by cumulative LOS displacement from track 173 subswath 1 on each date. The images are plotted in radar coordinates.
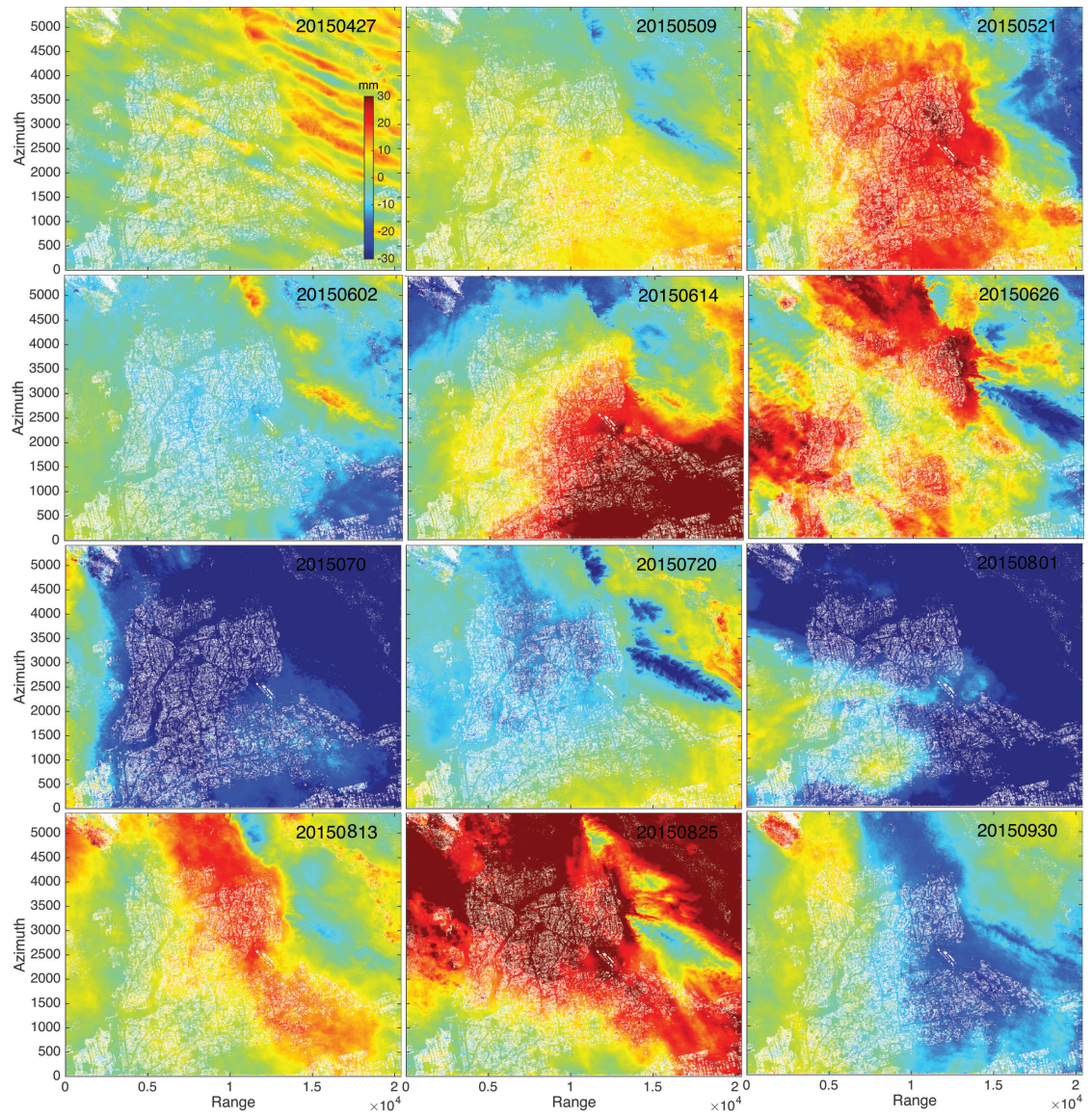
Figure S4.4: Atmospheric phase screen and time series for track 173, continued
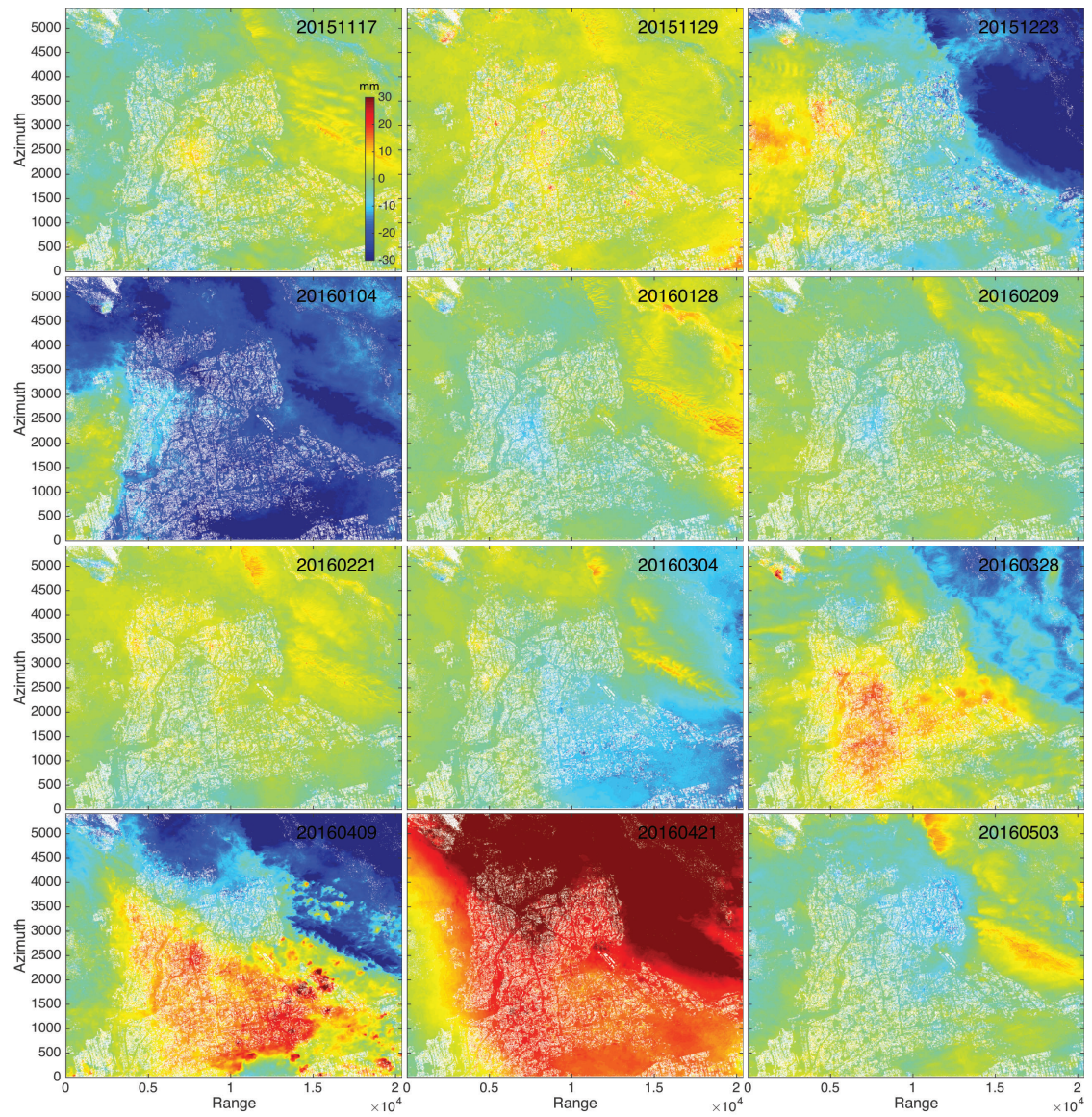
Figure S4.4: Atmospheric phase screen and time series for track 173, continued

Figure S4.4: Atmospheric phase screen and time series for track 173, continued

Figure S4.4: Atmospheric phase screen and time series for track 173, continued

Figure S4.4: Atmospheric phase screen and time series for track 173, continued

Figure S4.4: Atmospheric phase screen and time series for track 173, continued

Figure S4.4: Atmospheric phase screen and time series for track 173, continued
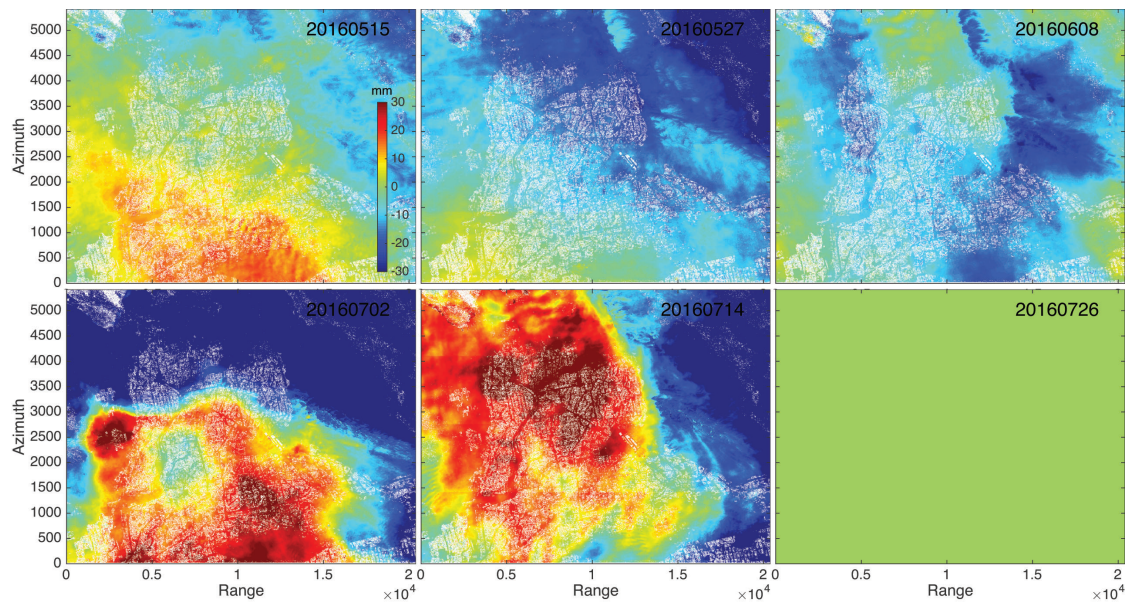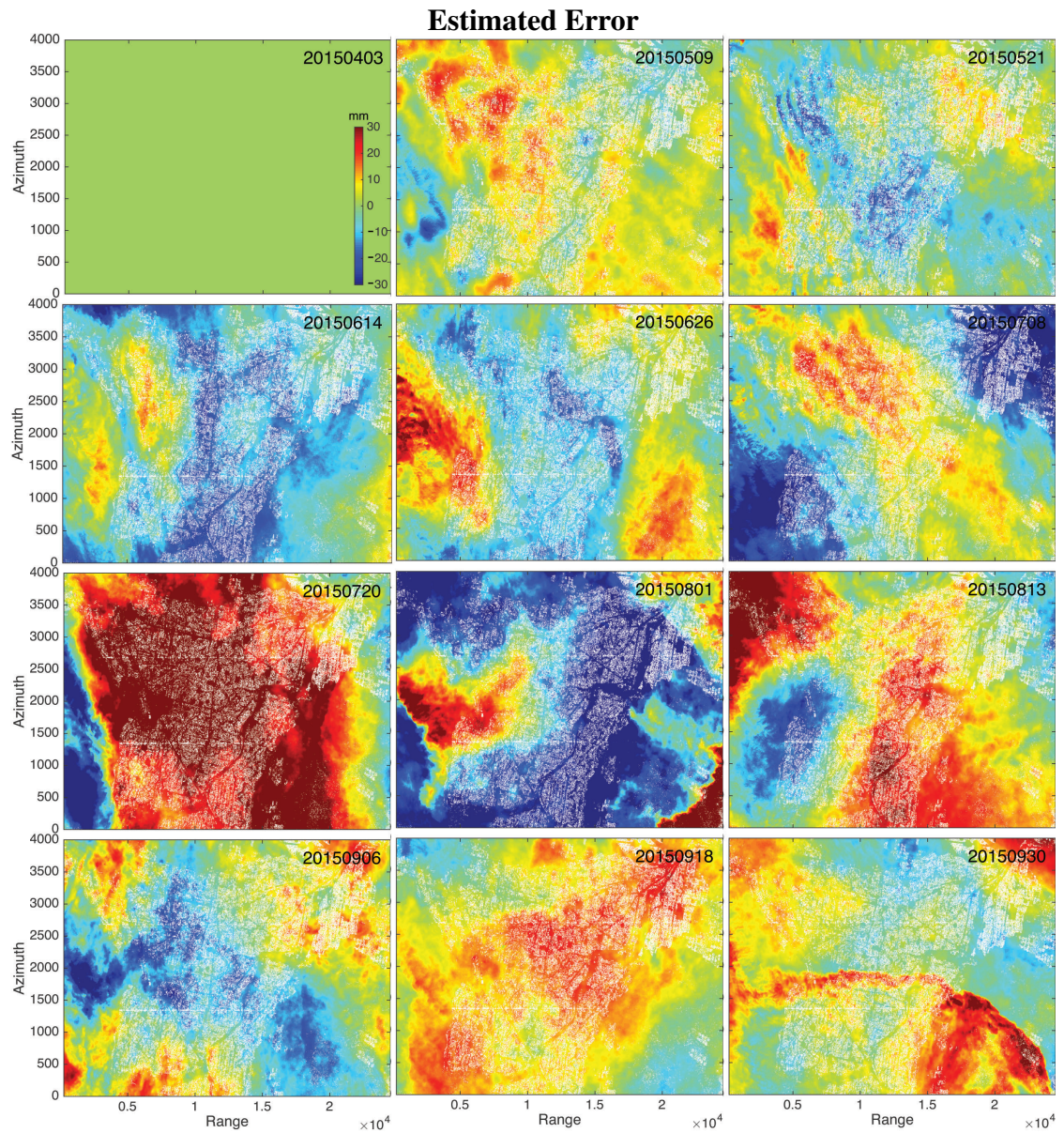
Figure S4.5: **Atmospheric phase screen and time series for track 166**. Plots are estimated atmosphere, ionospheric, orbit error, and clock error followed by cumulative LOS displacement from track 166 subswath 2 on each date. The images are plotted in radar coordinates.
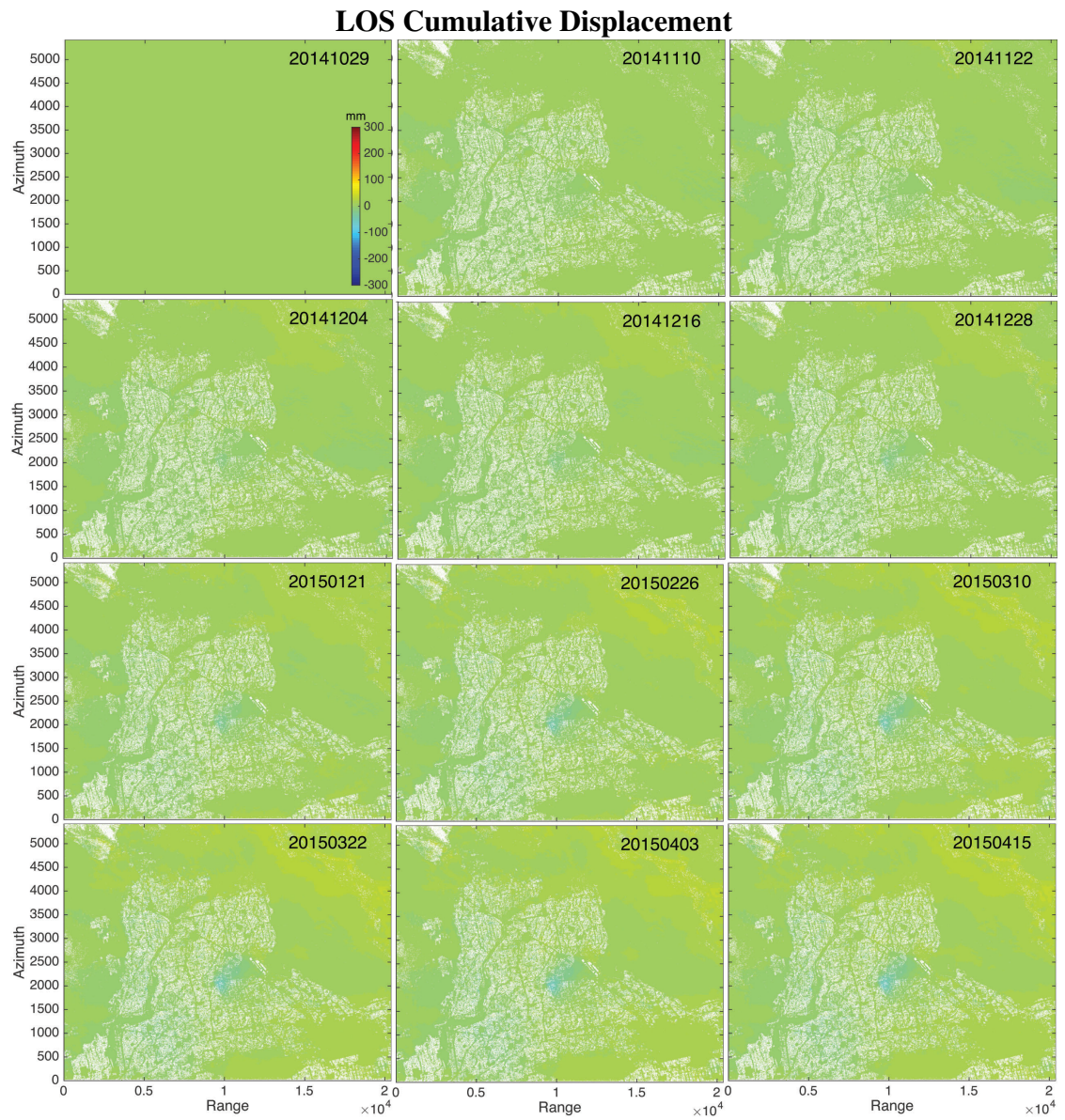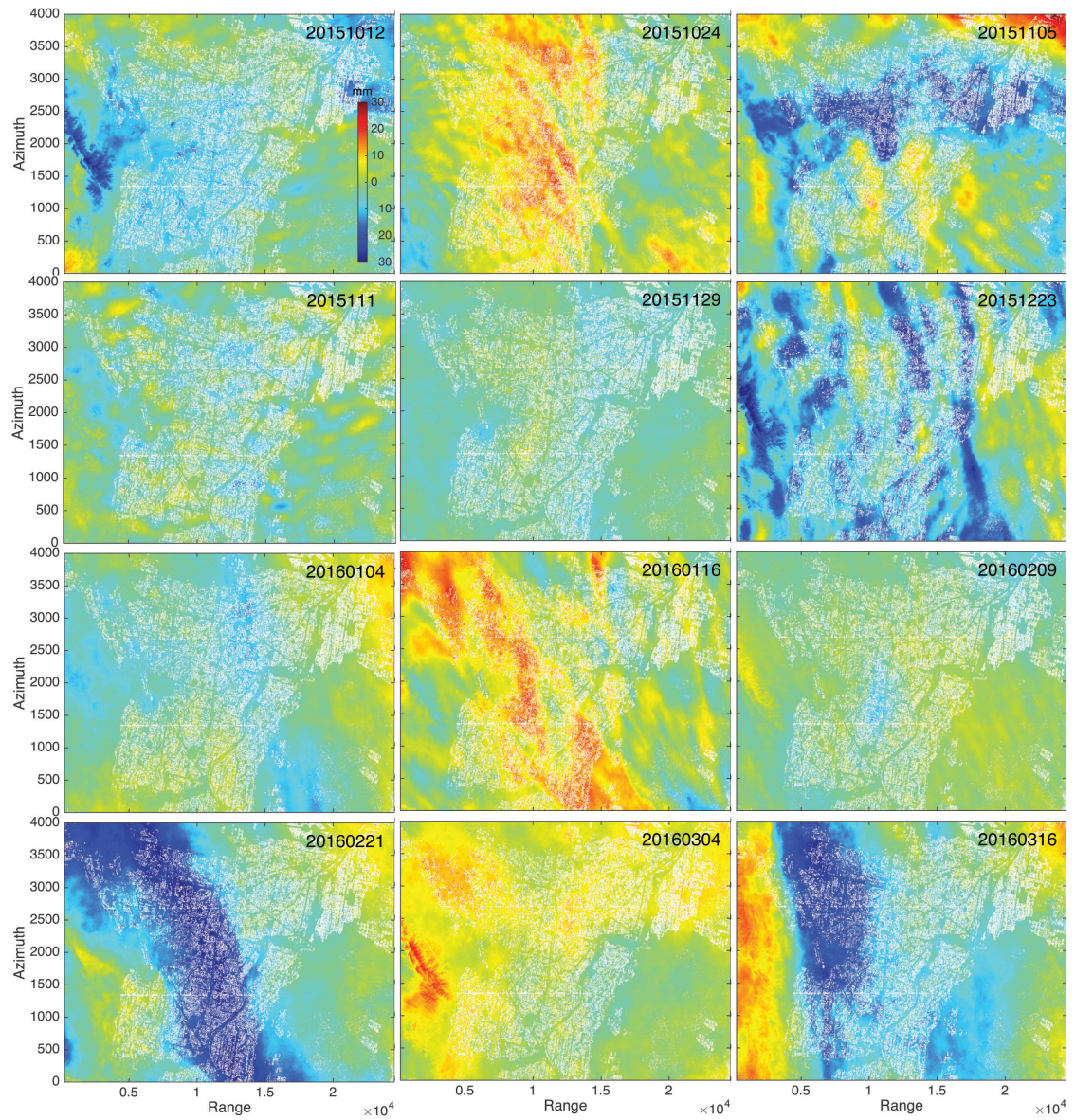
Figure S4.5: Atmospheric phase screen and time series for track 166, continued.
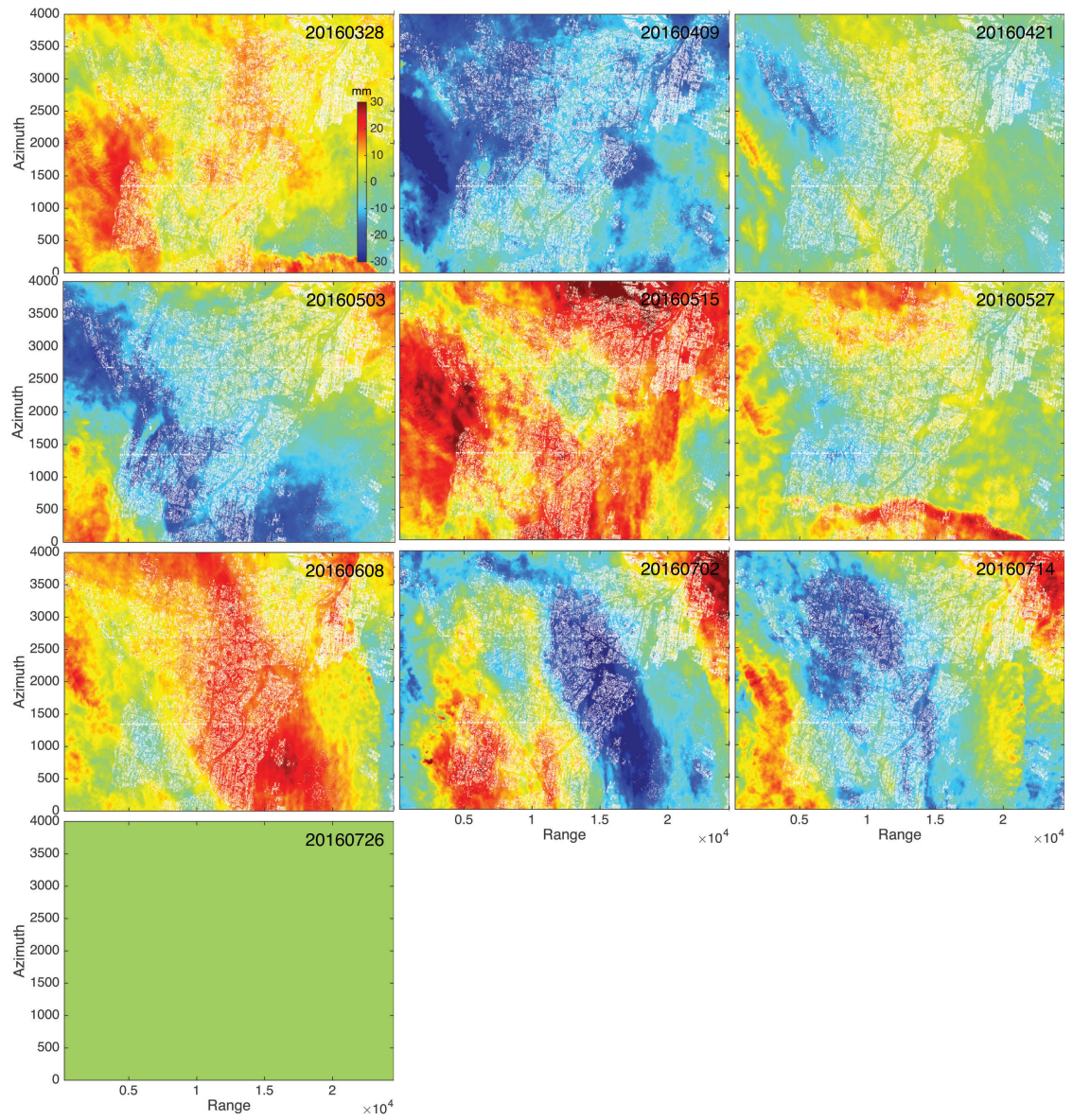
Figure S4.5: Atmospheric phase screen and time series for track 166, continued.

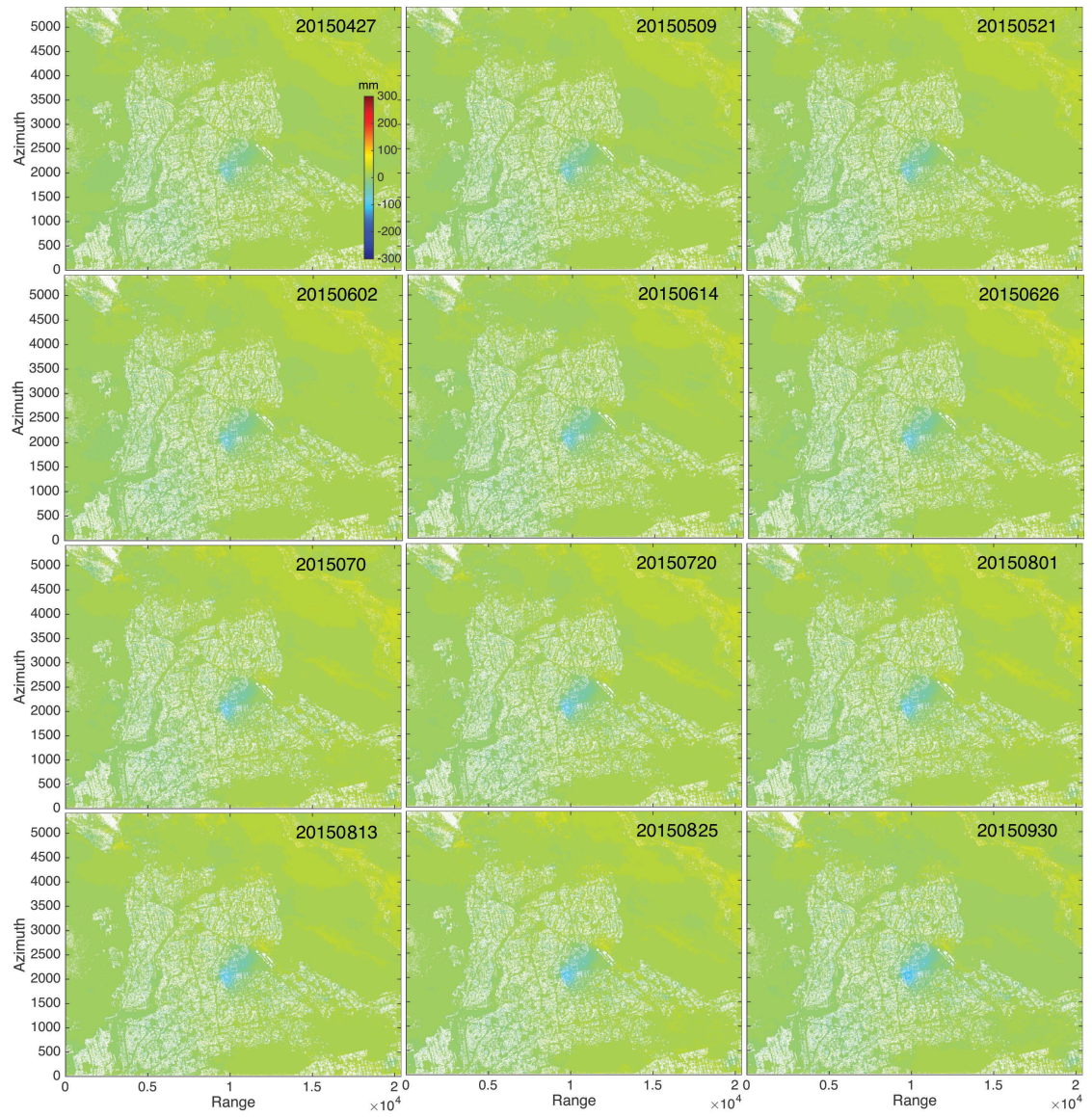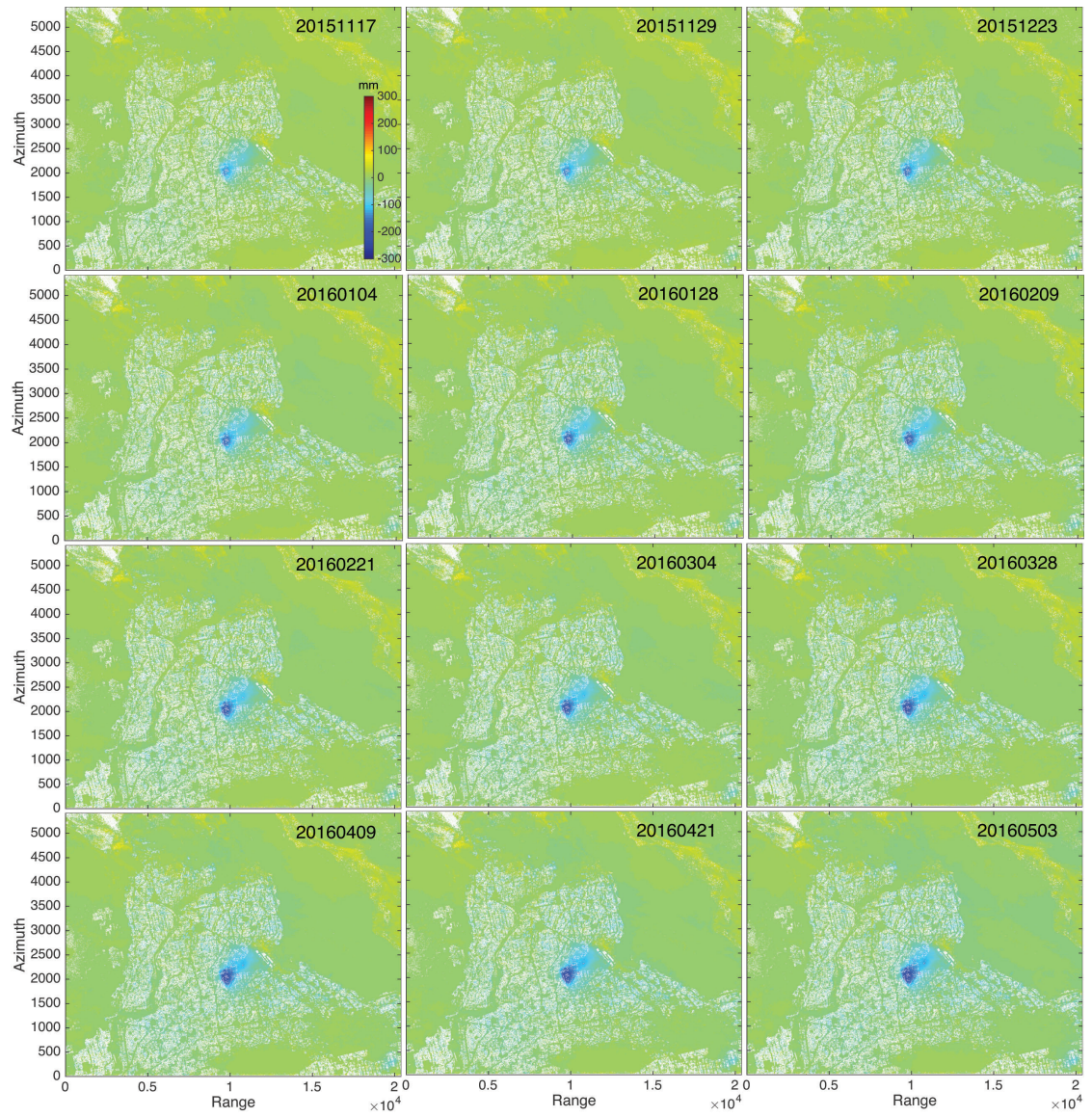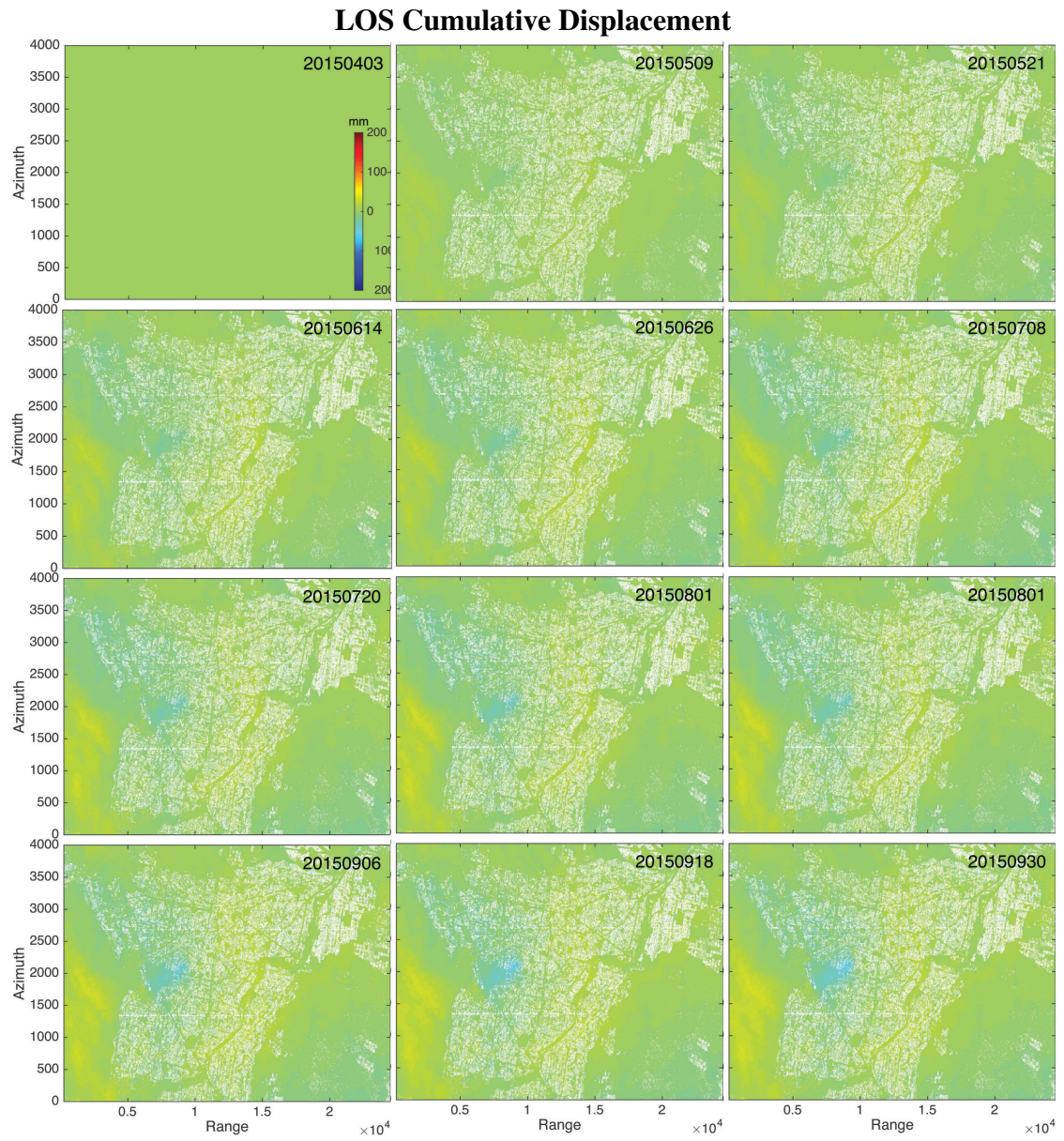**Figure S4.5: Atmospheric phase screen and time series for track 166**, continued.
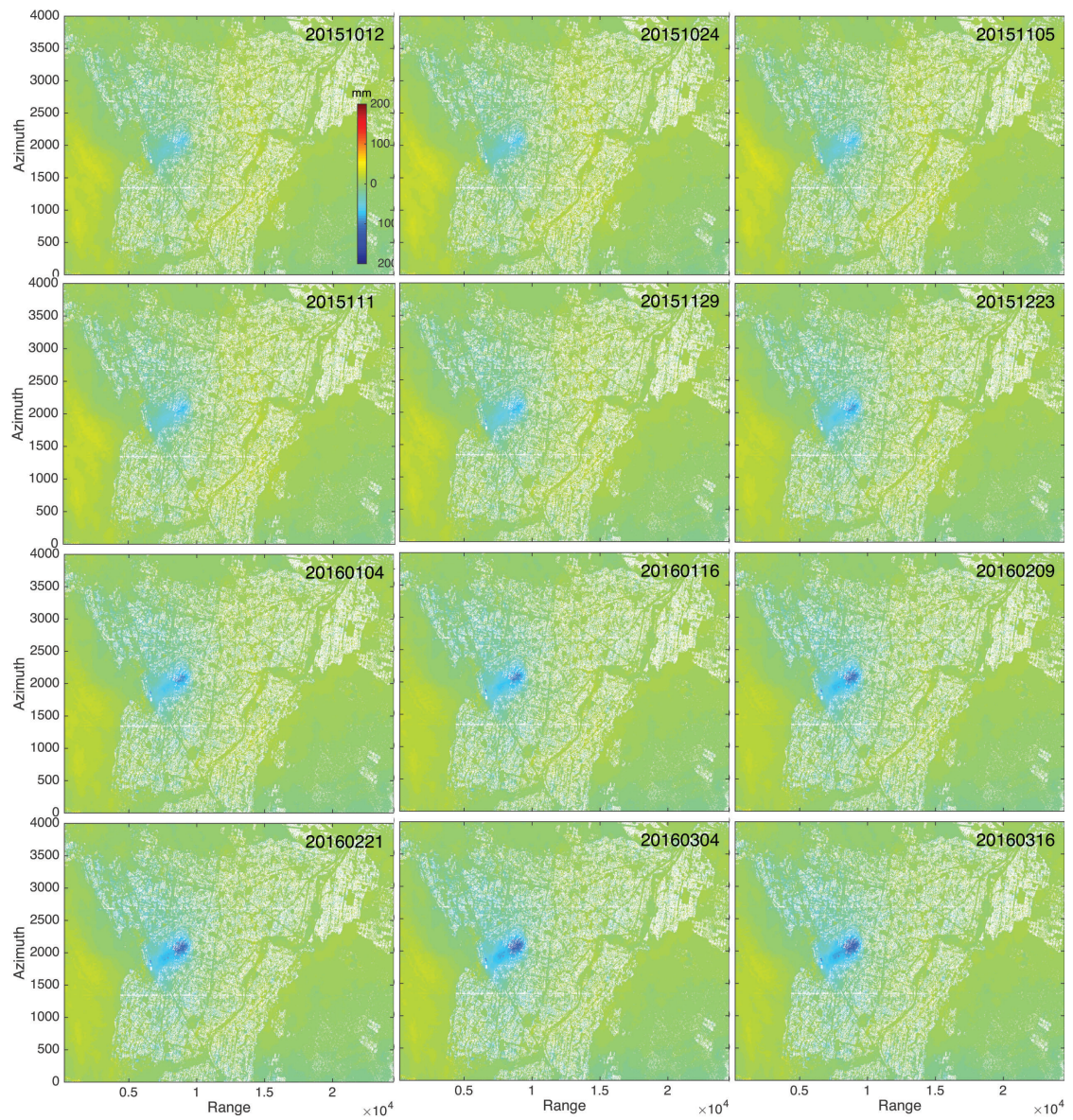
Figure S4.5: Atmospheric phase screen and time series for track 166, continued.
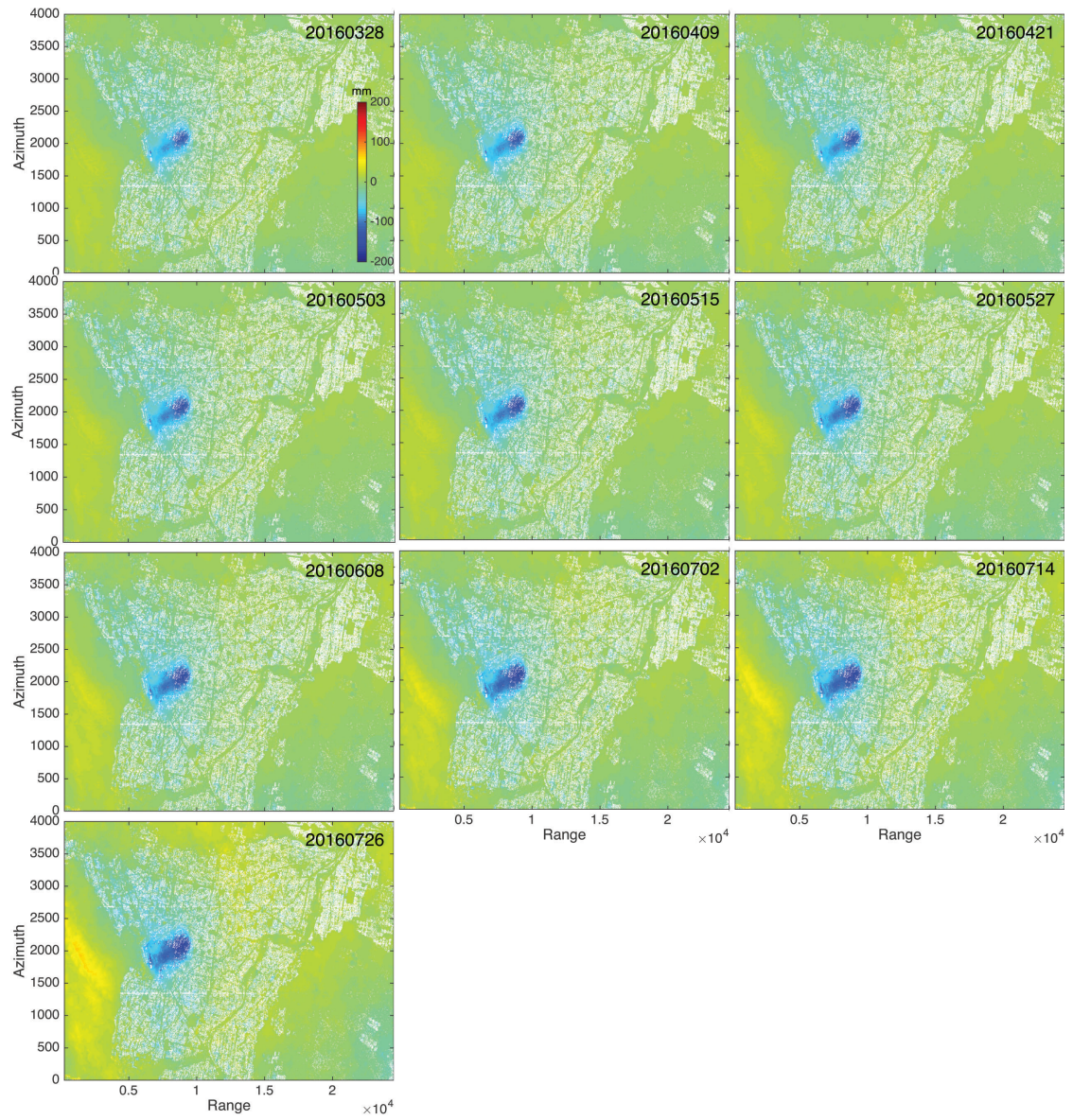
Figure S4.5: Atmospheric phase screen and time series for track 166, continued.
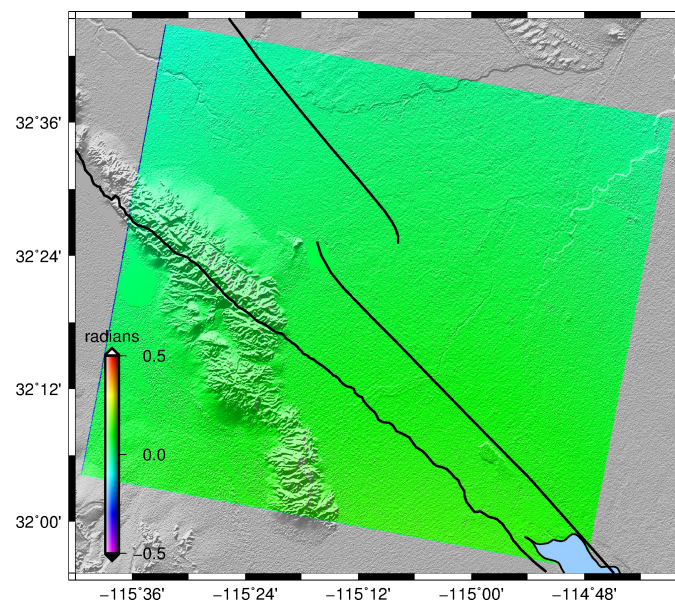
Figure S4.6: **Circuit test with topographic phase only for track 173 subswath 1**.
The residual phase has a median value of 0.23 mm and a median absolute deviation of
0.24 mm.
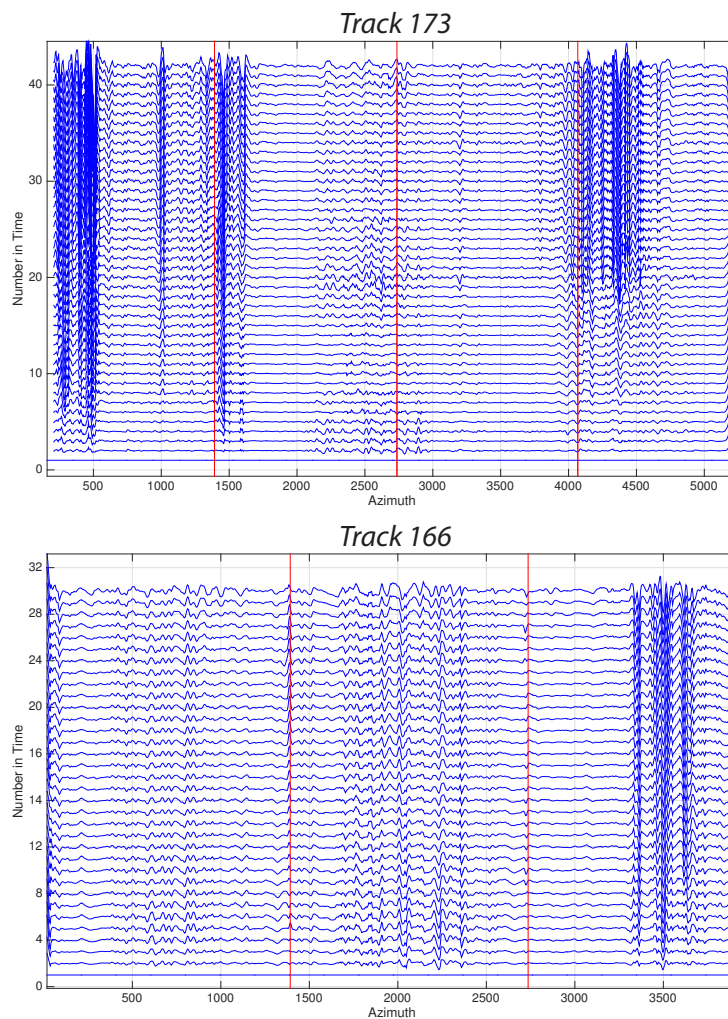
Figure S4.7: **High pass filtered profile time series for track 173 and track 166**. The blue lines represent the high pass filtered deformation field along the profiles shown in Figure S4.1. The red lines denote where the bursts boundaries are. No clear discontinuity is observed in this plot.
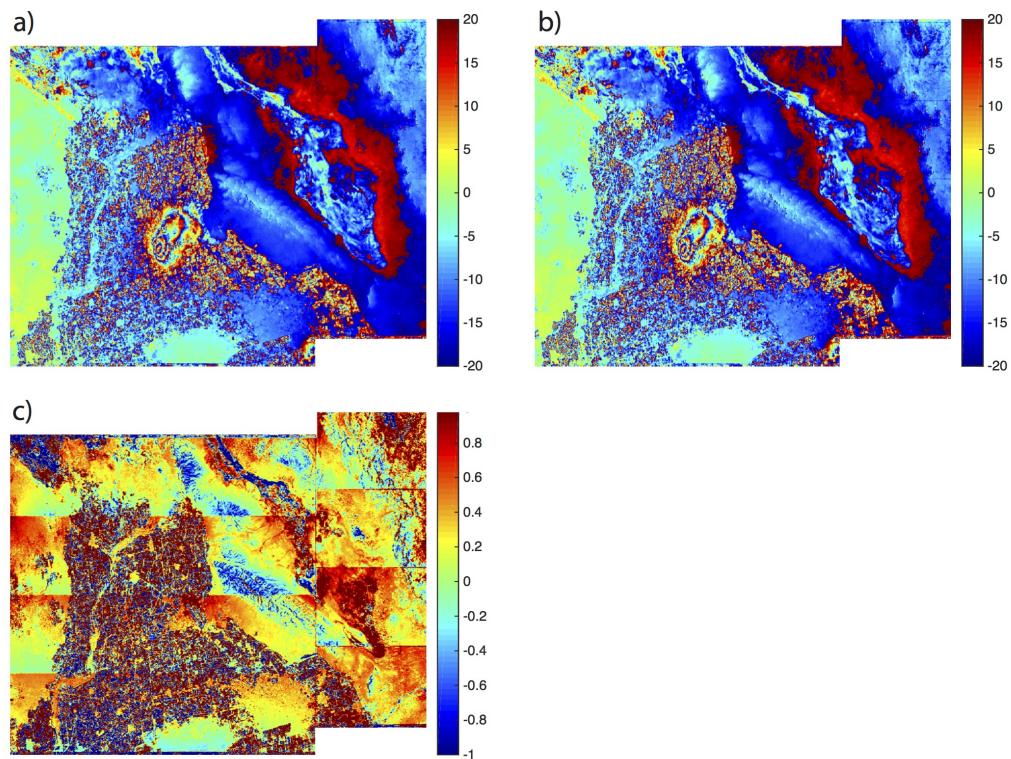
Figure S4.8: **Line-of-sight velocity maps from track 173, solved using atmospheric correction and coherence-based SBAS**. a) is the LOS velocity wrapped to -20 20 mm/yr, without performing ESD. b) is the LOS velocity wrapped to -20 20 mm/yr, with performing ESD. c) is the map of the difference between a) and b) in mm/yr.

Chapter 5

Tectonic and anthropogenic deformation along the San Andreas Fault revealed by GPS and the Sentinel-1 Satellites

The main objective of our research is to measure strain rate along the San Andreas Fault System to an accuracy of better than 100 nanostrain/yr at high spatial resolution (5-10 km) and moderate temporal resolution (2-3 months) using a combination of GPS and InSAR measurements. This information is critical for developing time dependent maps of earthquake forecast. Continuous GPS (cGPS) measurements offer high accuracy (1 mm/yr) vector displacement time series but we show here that the GPS-derived strain rate maps have poor resolution at lengths scales less than about 40 km because of the sparse spatial coverage. The regular SAR acquisitions and accurate baseline control being provided by the Sentinel-1 satellites will eventually improve the InSAR accuracy to the 1-2 mm/yr level. This study develops the methods for achieving that objective by

optimally combining the first three years of Sentinel-1 InSAR data with velocities from cGPS time series. The initial results show large amplitude vertical displacement in the Central Valley of California associated with the drought as well as the end of the drought. The largest errors are associated with propagation delays through the ionosphere and troposphere. Based on this analysis, we estimate three more years of acquisitions will be needed to reach a threshold accuracy of 100 nanostrain/yr at a 10 km spatial resolution. We note that the accuracy and resolution of these time-dependent strain rate maps will continue to improve as the Sentinel-1 satellite series continues for its planned 20 years of operation.

5.1 Introduction

The absence of a major earthquake along the San Andreas Fault System (SAFS) over the past 100 years, a region home to over 10 million people, provides ample motivation for studying the crustal deformation of this active plate boundary. While the timing of the next major earthquake is largely unpredictable, the earthquake potential along all of the faults can be forecast using geodetic measurements of crustal strain rate. A recent compilation [Kreemer, Blewitt, and Klein 2014] and analysis [Elliott, Walters, and Wright 2016] of global geodetic data shows that for Eastern Turkey and California, there is a clear relationship between geodetic strain-rate and both seismic moment release and earthquake rate. Areas where strain rate is less than about 100 nanostrain/yr have both low seismic moment release and low a-value for the Gutenberg-Richter scale. One of the largest uncertainties in the California earthquake hazard models (i.e., UCERF-3 [Field et al. 2013; Field et al. 2016]) is the amount of plate boundary deformation that is accommodated by off-fault strain and whether this strain is accumulating as elastic or as plastic deformation. Therefore improved strain rate measurements are needed to improve

earthquake forecasts.

In theory, continuous GPS (cGPS) and InSAR measurements can be combined to develop crustal velocity models, and ultimately strain rate maps, having both high accuracy and high spatial resolution [Lyons and Sandwell 2003; Johanson and Bürgmann 2005; Fialko 2006; Shirzaei et al. 2013; Tong, Sandwell, and Smith-Konter 2013]. To date these combinations have solved for average crustal velocity and not full displacement time series mainly because of the irregular cadence and poor interferometric baseline control of the older SAR acquisitions (e.g. ERS-1,2, ALOS, ENVISAT). In the case of the California-wide ALOS-1 analysis, the uncertainties are 2-4 mm/yr when averaged over 5 km cells [Tong, Sandwell, and Smith-Konter 2013]. This corresponds to a very high strain rate error of 400-800 nanostrain/yr. Most of the errors are associated with propagation delays through the troposphere [Emardson, Simons, and Webb 2003] and ionosphere [Rosen, Hensley, and Chen 2010; Fattahi, Simons, and Agram 2017] although some of the error is due to seasonal variations in vertical ground motion associated with hydrology signals [Hammond, Blewitt, and Kreemer 2016]. The LOS InSAR measurements are dominated by vertical signals because of the steep look angle of the radar so the vertical motions must be temporally resolved before they can be accurately modeled and removed. As described in Chapter 4 [Xu et al. 2017], the InSAR data being provided by the Sentinel-1A and 1B satellites has a regular cadence of 12 or 24 days in the California region and 6-day repeats are possible in case of a seismic event. This regular cadence combined with accurate orbits is providing the data needed to reach the 100 nanostrain/yr accuracy.

In this chapter, we refine the approach developed in Chapter 4 [Xu et al. 2017], to optimally combine InSAR and GPS data, and apply this algorithm to derive an LOS

time series deformation map for the entire SAFS using the first 3 years of Sentinel-1 data. We begin by estimating the accuracy and spatial resolution of the existing strain rate models derived from GPS data. This is accomplished through an analysis of 17 independent strain-rate models that were assembled for the SCEC Community Geodetic Model Version 1.0 (CGM V1) [Sandwell et al. 2016]. All pairs of strain rate models are cross-correlated in the wavenumber domain to establish their spatial resolution. This spatial resolution is used to select the optimal crossover wavelength for combining GPS and InSAR (e.g. [Wei, Sandwell, and Smith-Konter 2010; Tong, Sandwell, and Smith-Konter 2013]).

The Sentinel-1 InSAR data are analyzed as described in Xu et al. [2017] but with one significant improvement. Each phase unwrapped interferogram has an unknown $2N\pi$ integer phase ambiguity. We have developed a method for solving for these ambiguities by using the constraint that sums of interferograms around closed loops must be zero. After finding the set of ambiguities for all interferograms in the stack, one can accurately connect the phase of the first SAR image in the stack with all other images including the last image. This approach is also used to identify subareas having integer ambiguities that are inconsistent with the larger area; we mask these areas, usually associated with seasonal snow cover.

The time series is constructed using a coherence-based SBAS algorithm [Tong and Schmidt 2016] that includes an atmospheric-phase correction by common scene stacking [Tymofyeyeva and Fialko 2015] as well as an elevation-dependent atmospheric phase correction [Elliott et al. 2008]. Finally we have refined the SURF remove/restore method of combining the GPS and InSAR to utilize the vertical GPS data to form InSAR time series having 3 month temporal resolution. The initial results are consistent with the

large-scale horizontal crustal motions provided by the cGPS data. In addition, the new high spatial resolution LOS grids reveal numerous previously unmapped vertical crustal motions mostly due to seasonal and secular variations in groundwater recharge/extraction. We estimate that with an additional 3 years of Sentinel-1 and cGPS time series data, the 10-km resolution strain rate maps will reach an accuracy of 100 nanostrain/yr that is useful for earthquake forecasting.

5.2   Assessment of GPS strain rate models from Community Geodetic Model Version 1.0

As discussed in the introduction, we use the GPS data to constrain the longer wavelengths of the velocity and strain rate models and the InSAR data to provide the shorter wavelength. The approach is similar to the sum/remove/filter/restore (SURF) method developed by previous studies [Wei, Sandwell, and Smith-Konter 2010; Tong, Sandwell, and Smith-Konter 2013]. The main difference is that we construct an InSAR time series rather than just an average velocity. The optimal wavelength for the filter step depends somewhat on the application. The main objective of the [Tong, Sandwell, and Smith-Konter 2013] study was to recover the LOS velocity for the SAFS from ALOS-1 data. They established the optimal filter wavelength by performing a cross-spectral coherence analysis of 37 profiles crossing the SAF extracted from 4 block models. A standard Welch's modified periodogram method [Welch 1967] implemented in Matlab was used to calculate the cross-spectral coherence among the 4 models (i.e., 6 possible model combinations). To first order, the coherence among GPS models was high (>0.8) between wavelengths of 150 and 66km and then dropped to 0.5 at about 20 km wavelengths. This wavelength is expected because it corresponds to the characteristic spacing

of the GPS receivers.

Here we perform a similar cross-spectral coherence analysis on the second invariant of the strain rate for 17 models that were assembled for the SCEC Community Geodetic model (CGM-V1) (Figure 5.1 [Sandwell et al. 2016]. The models were taken from publications [Zeng and Shen 2014; Shen et al. 2015; Smith-Konter and Sandwell 2009; Tong, Sandwell, and Smith-Konter 2013; Tape et al. 2009; Petersen et al. 2008; Petersen et al. 2014; Platt and Becker 2010; McCaffrey 2005; Loveless and Meade 2011; Hackl, Malservisi, and Wdowinski 2009; Parsons 2006; Parsons et al. 2013; Kreemer, Blewitt, and Klein 2014; Flesch et al. 2000; Field et al. 2014; Sandwell and Wessel 2016]. We analyzed these models by computing the cross spectrum in their overlapping region in Southern California (longitude 118.3 west, 114.3 west and latitude 32.6 north, 36.3 north, about 400 km $\times$ 400 km). We first re-grid each model at 0.01 degree using splines with tension [Smith and Wessel 1990]. Then we de-trend each model and apply a 20km wavelength edge taper. Finally, we compute the radially-averaged, cross-spectral coherence between every pair of models using Generic Mapping Tools (GMT) [Wessel et al. 2013] (Figure 5.2). For most pairs, the coherence is high very long wavelength and decreases to zero coherence at tens of kilometers. The 0.25 coherence threshold is roughly located at 80 km wavelength.

As illustrated in Figure 5.2, there is a large variation in the coherence between these models. All but one agree at long wavelength, but generally disagree at short wavelength, except those having very similar modeling approaches like Shen [Shen et al. 2015] and Zeng [Zeng and Shen 2014] or Tong [Tong, Sandwell, and Smith-Konter 2013] and Smith-Konter [Smith-Konter and Sandwell 2009]. The disagreements are due to differing physical modeling approaches, differing fault geometries, and different GPS

velocity data sets. First, the physical models vary from elastic half space block models to layered deep dislocation models to models including time-dependent earthquake cycle effects. These differing approaches lead to different slip rates [Evans 2017] and thus strain rate. Interestingly, the isotropic interpolator gpsgridder, which we use in this paper, has an above-average coherence with most of the models. This approach used elasticity to couple the east and north velocities [Haines and Holt 1993] and is implemented as gpsgridder in GMT [Sandwell and Wessel 2016]. The SEISM model, which is converted from seismicity analysis, also agrees well with others at long wavelength. Second, the fault segments used by the various dislocation/block models have significant differences. This leads to a mismatch in the location of the strain rate peaks above the faults. Third, the models were based on slightly different GPS data sets with different station distributions.

The roll-off in the coherence plots (Figure 5.2) is similar to the findings in [Tong, Sandwell, and Smith-Konter 2013], but the threshold wavelength we found is quite different. This difference is not only because we are comparing strain rate instead of velocity, but also the way we compute the spectrum is different. In [Tong, Sandwell, and Smith-Konter 2013], they computed the cross-spectrum using an averaging technique similar as the Welch's method [Welch 1967] and it's done over 37 profiles crossing the SAFS using LOS projected GPS models, which only accounts for the largest fault-parallel velocity component. What we computed is a more general two dimensional radial cross-spectrum with the second invariant of the strain rate tensor which uses both horizontal velocity components. Based on this cross-spectrum analysis, we conclude that 80 km wavelength is an appropriate crossover wavelength for combining GPS and InSAR for the construction of strain rate.

5.3   Combining InSAR time-series and GPS models

The InSAR and GPS combination approach presented here is similar to the "SURF" (Sum/Remove/Filter/Restore) [Wei, Sandwell, and Smith-Konter 2010; Tong, Sandwell, and Smith-Konter 2013] where complementary filters are designed to combine the GPS and InSAR. Since our goal is to construct a LOS time-series instead of a velocity map, and we are investigating a much larger region, there are significant changes to the "SURF" approach. For velocity estimate, the stacking approach will enhance the signal-to-noise ratio, taking advantage of the spatially correlated atmospheric noise are uncorrelated in time (for longer than 1 day) [Williams, Bock, and Fang 1998; Emardson, Simons, and Webb 2003; Tymofyeyeva and Fialko 2015]. When we construct a long time-series with short time span interferograms, the signal-to-noise ratio (SNR) of each is quite small; an alternate method for noise reduction is achieved using a common-scene stacking technique [Tymofyeyeva and Fialko 2015]. This technique isolates and removes the noise in each SAR image using interferograms from the surrounding three months. This retains true vertical signals related to annual hydrologically driven ground motions. The second difference is related to the filter length scale. Our expanded study area covers the Central valley of California where a large region (150 km by 300 km) underwent subsidence (one area > 20 cm/yr) during the 2011-2017 drought. In this Central valley region, the GPS stations have a mean spacing of more than 60 km so the InSAR is needed to resolve the large scale vertical motions. The third difference is that the SURF method only used the horizontal velocity components to resolve the large scale deformation while for this new time series method, the noisier vertical GPS data are needed. Because of these differences we refined the method for combining InSAR time-seres and GPS data.

5.3.1 InSAR data processing

To construct the InSAR time-series along the SAFS, we gathered all together 5 tracks 229 acquisitions Sentinel-1 TOPS data, each of which covers roughly 250 km × 420 km (Figure 5.4, about 60 bursts); the time span is 2014.10 to 2017.09. Unlike previous InSAR satellites such as ALOS-1 where the temporally repeating frames were aligned spatially and had significant overlap with adjacent frames, the frames of Sentinel-1 data are not always aligned spatially and there is no overlap. After downloading all the data, we established new frame boundaries that would accommodate most of the repeating data and removed the data that had either non-consecutive sensing or not enough coverage. A special program was written to merge the imagery (geotiff) and metadata (xml) into continuous products and then cut them all to the same burst boundaries. We produced 1066 interferograms based on a maximum 120 day temporal baseline threshold and a maximum 150m perpendicular baseline threshold. The sum of the 1066 InSAR time spans is 58,597 days. Detailed information from each of the tracks can be found in Table 5.1. All the interferograms were processed using the GMTSAR software with open access at `http://gmt.soest.hawaii.edu/projects/gmt5sar`. The detailed algorithm of TOPS InSAR processing can be found in Section 4. Beyond that there are a few more points we want to address here.

The processing is slightly different than performed by other groups. We do not apply enhanced spectral diversity (ESD) to minimize possible azimuth mis-registration error at burst boundaries. There are two advantages to not making this ad-hoc correction. First every slave image can be geometrically aligned once with the master. This greatly simplifies the processing and ensures an absolute phase connection between the first image and last image in the sequence. In contrast, a near-neighbor alignment approach with ESD could introduce a systematic error to the phase and may bias the long-term ac-

curacy of measurement. Second, over decadal time scale there will be true plate motions with respect to the international terrestrial reference frame (ITRF) that can be eventually measured at burst overlaps [Hooper and Spaans 2016]. Indeed, this true azimuth shift will provide an additional along-track component to the InSAR measurement. Thus instead of correcting the usually small ($<$2 mm) mis-registration error using ESD, we can remove it as part of the atmospheric phase correction or keep it to use as an along-track displacement measurement. Note the mis-registration error shares the same spatially correlated and temporally uncorrelated characteristics as atmospheric noise.

A second difference is related to phase unwrapping and removal of an $2N\pi$ integer phase ambiguity. This allows an absolute phase connection between the first and last SAR image in the sequence similar to a GPS time series. Individual interferograms are unwrapped using a Statistical-Cost Network-Flow Algorithm for Phase Unwrapping (SNAPHU) [Chen and Zebker 2001]. Two types of phase unwrapping errors are possible. The first is the $2N\pi$ unwrapping ambiguity which is uniform over the entire interferogram. The second is small scale unwrapping errors manly associated with de-correlatted areas, such as farms, sand and snow; we cannot correct these errors and mask out this part of the stack. For the uniform $2N\pi$ ambiguity, our objective is ensure phase closure around InSAR loops. For example if there are three SAR images, 1, 2, and 3 and we form the three possible interferograms 12, 23, and 31, the sum of these interferograms should be zero except for a small amount of phase noise. However, the sum is commonly $2N\pi$ where N is an integer. To identify and correct these integer ambiguities, we construct triangular phase-loops from all the interferograms. The loop ambiguity is the nearest integer to the median of the loop residuals; they provide the data for an inverse problem

as is shown below.

$$\mathbf{Gm} = \mathbf{d}, \text{where } \mathbf{G} = \begin{bmatrix} 1 & 1 & -1 & 0 & \dots & 0 & 0 & 0 & 0 \\ 1 & 0 & 1 & -1 & \dots & 0 & 0 & 0 & 0 \\ \vdots & \vdots & \vdots & \vdots & \ddots & \vdots & \vdots & \vdots & \vdots \\ 0 & 0 & 0 & 0 & \dots & 1 & 1 & 0 & -1 \\ 0 & 0 & 0 & 0 & \dots & 0 & 1 & 1 & -1 \end{bmatrix} \text{ and } \mathbf{d} = \begin{bmatrix} 1 \\ 2 \\ \vdots \\ -1 \\ 0 \end{bmatrix} \quad (5.1)$$

where $\mathbf{G}$ is the Green's matrix with 1 and -1 representing the phase loops and $\mathbf{d}$ is just the list of N_i. Thus $\mathbf{m}$ is the just the list of C_j, representing $2C_j\pi$ ambiguity needed for each interferogram to create the non-closure loops. j is the index for interferograms. The Green's matrix $\mathbf{G}$ contains full constraints on circuit closure as any other loop can be acquired by summing triangular loops. Then we assume there are only a limited number of ambiguities created during automatic unwrapping and put this problem to a sparse solver where we

$$\min_{m} ||\mathbf{m}||_1 \qquad \text{subject to } ||\mathbf{Gm} - \mathbf{d}||_2 \leq \varepsilon \qquad (5.2)$$

After solving for $\mathbf{m}$, we round the solution to integers and update the phase of each interferogram, recompute the loop ambiguities, and perform another inversion. This is repeated until the loop ambiguities are zero which usually takes a few iterations. After achieving a stable solution, we recompute the loops to identify localized unwrapping errors caused by decorrelation. Areas having more than 25% misclosures are masked. We consider the remaining pixels stable enough for time-series analysis. An example of this correction can be found in Figure 5.3

5.3.2   Constructing InSAR time-series

The algorithm we used for constructing InSAR time-series has one significant difference from the approach in Chapter 4. For that analysis we selected a small area in the stack on the stable North American plate and forced its deformation to be zero as a function of time. There is a disadvantage with that approach because this also forces the atmospheric error to be zero over that patch. If it was not zero then forcing it to zero will corrupt the entire frame. In our new analysis we don't need to force any area to have zero deformation because we solved for the phase unwrapping ambiguity during InSAR data processing. Moreover, next we combine the InSAR time-series with a GPS model which further corrects the large spatial scale errors. During the time-series analysis, we use a combined algorithm [Xu et al. 2017] with both coherence-base SBAS [Tong and Schmidt 2016] and atmospheric phase correction by common-scene stacking [Tymofyeyeva and Fialko 2015]. As mentioned in Chapter 4, this algorithm will weigh the contributions from every interferogram to robustly compute a time-series, during which, it'll also absorb the turbulent component from the time-series and correct for any remaining discontinuities associated with mis-registration error. We adjusted the algorithm to decrease the temporal smoothness to let the algorithm find its balance between turbulent and stationary signals. One important unresolved problem with the algorithm is related to the fact that the atmospheric errors typically have a red spectrum. The iterative algorithm works to minimize these larger-amplitude, long-wavelength wavelength errors first and sometimes does a poor job of minimizing prominent smaller scale signals such as those due to gravity waves. As a final step in the atmospheric error mitigation we apply an elevation dependent atmospheric phase correction during the combination of InSAR and GPS in order to further remove the short wavelength atmospheric noise [Elliott et al. 2008; Doin et al. 2009].

5.3.3 Combining InSAR and GPS

There are many published approaches for combining GPS and InSAR velocities [Gourmelen, Amelung, and Lanari 2010; Johanson and Bürgmann 2005; Peltzer et al. 2001; Ryder and Bürgmann 2008; Wei, Sandwell, and Smith-Konter 2010; Tong, Sandwell, and Smith-Konter 2013]. The first step usually involves modeling or sometimes just a low-order polynomial fit, most of which does not consider the vertical component of GPS. The second step mainly uses the remove/restore technique during which different corrections are performed. Our objective is to develop a full time-dependent of InSAR time series with GPS time series to form time-dependent LOS displacement time series. As discussed above we have constructed phase ambiguity-corrected LOS InSAR time series with about 3 month temporal resolution but as described next we have not yet used GPS time series to correct the long wavelengths. That is work in progress. The current algorithm follows:

1. Construct the InSAR time series as described above. We then compute horizontal velocity GPS grids (east and north using gpsgridder) in the International Terrestrial Reference Frame (ITRF).

2. The horizontal velocity components are projected into the LOS direction for every point in each InSAR frame as shown in Figure 5.4a. The flight direction of the satellite is NE to SW and the radar is looking toward the right. The discontinuities at frame boundaries are due to the variation on the look angle from 30 degrees in the near range on the ESE of each frame to 46 degrees in the far range. This is converted to linear displacement time series and removed from the LOS time series. The remaining LOS displacements are due to residual atmospheric phase delays at each time epoch as well fas mostly secular ground variation.

3. The remaining atmospheric delay is modeled as $\phi_{xy}^{atm-topo} = ax + by + c + E_{xy}(p_0 +$

$p_1x + p_2y + p_3xy + p_4x^2 + p_5y^2...$), where a, b, c are coefficients for a plane, E_{xy} is the elevation and p_is are the elevation dependent coefficients to quantify the effect of layered water vapor content over mountainous region with allowing spatial variations [Elliott et al. 2008]. From our test, a planer variation ($i = 2$) is was adequate for most cases.

4. Correct the very long wavelength (>80 km) errors in the LOS displacement time series using the low-pass filtered vertical GPS.

5. Restore the horizontal GPS model to the InSAR time series displacement maps and also compute a long-term average LOS velocity model (Figure 5.4b).

There are several attributes of the Sentinel-1 InSAR data that are changing the InSAR time series methods. The first is that the pure geometric alignment enables one to add new SAR images to the time series without making any changes to the existing stack because each new image is aligned to the single master. This combined with the ability to resolve the integer ambiguities in each interferogram using circuit closure constraints enables an accurate absolute phase connection between the first and last image in the time series even when a direct interferogram between them would be completely decorrelated. The larger scenes 250 X 420 km enables a longer crossover wavelength for merging the GPS and InSAR which will be needed for resolving crustal strain rate.

Again we are still experimenting with methods of combining GPS and InSAR time series so we expect the method will be revised over the next few years especially as a longer and more regular time series of Sentinel-1 data become available. In particular removal of the ionospheric contribution to each interferogram may be critical in the refinement of the method and we plan to introduce the split-spectrum ionospheric estimation method that is being pioneered by other groups (e.g. [Fattahi, Simons, and

Agram 2017]).

5.4 Results and discussions

5.4.1 GPS model and InSAR velocity map

The time averaged LOS velocity model is shown in Figure 5.4b . It is clear that the Sentinel-1 data add significant signals, both at short and intermediate wavelength. Some prominent features include, from north to south, the subsidence signal at the Geysers geothermal field, the uplift over the Santa Clara Valley in the Bay area, the fault creep around the Hayward fault, a sharp LOS velocity step over the creeping section of the SAF, a large and rapid subsidence signal in the Central Valley region, subsidence at the San Jacinto fault step-over, the uplift at Laguna Salada, and the strong subsidence around the CPGF discussed in Chapter 4. Next we'll zoom in on four of the most prominent and distinctive features. Since we have less than 3 years of data, the average rates may not represent true rates because of atmospheric contamination. Thus we provide mostly qualitative interpretations instead of converting the velocity to more comprehensive analysis of creep rate or moment rate.

The first area is the Santa Clara valley where we found uplift at a maximum rate of 4 cm/yr (Figure 5.5a), which clearly did not show up in previous analysis [Shirzaei and Bürgmann 2013]. The recent uplift is potentially related to ground water recharge that started around 2014 (http://waterinthewest.stanford.edu/groundwater/recharge/). Another interesting feature is that uplift rate changes across the Silver Creek fault, a quaternary fault not currently slipping. The discontinuity in the uplift rate could be caused by the fault acting as a barrier that prevents the flow of water transfer from one side to the other.

East of this uplift signal we see about a 5 mm/yr creep signal (in LOS) at the Hayward fault. More interestingly, the creep on the central strand not as prominent as the strands to the north and the south.

The second area is the creeping section of the San Andreas fault, where there is about a 15 mm/yr LOS velocity step across the fault, with patterns similar to the ALOS-1 results [Tong, Sandwell, and Smith-Konter 2013]. We also see an anomalous ground motion to the west of the creeping section near its southern end. We believe this is either and uncorrected atmospheric error or is related to the vegetation difference on across the Cholame Hills. The cause of this anomaly will be better understood with accumulation of Sentinel-1 data and some further analysis on data from the ascending tracks. The on-fault subsidence just north of Parkfield reaches a maximum of around 3 cm/yr, which we think is related to ground water withdrawal.

The third area discussed here is the Central Valley of California. Due to the recent drought, which started around 2011, there has been extensive extraction of ground-water mainly for agricultural purposes. This has caused a large area of subsidence as seen in both InSAR and GPS (Figure 5.6). The maximum subsidence, at the southern end of the valley, is over 30 cm/yr along the LOS direction. The small discrepancy between the InSAR and GPS time-series projected into the LOS could be due to the different sensing depths. GPS stations are mostly deployed to the bedrock but InSAR is mainly measuring the most shallow surface layer. Another interesting feature is the recent pause in the subsidence beginning in 2017 (Figure 5.5). This might represent a recharge in the aquifer during the abundant rains in the winter of 2017. There are also some more isolated subsidence areas (blue dimples) around the southern edge of the Central Valley. These are due to more localized areas of oil extraction such as the Elk Hill

oil reserve and two oil fields to the north of Oildale [Fielding, Blom, and Goldstein 1998].

The fourth area discussed here is a broad area of deformation across the Elsinore, San Jacinto and San Andreas faults (Figure 5.5d). This deformation is observed in two Sentinel-1 tracks 71 and 173. Although track 173 has a larger atmospheric contamination due to fewer scenes. Despite these atmospheric artifacts, there is a clear subsidence signal at the San Jacinto Fault pull-apart basin. This is most likely also due to groundwater extraction although there could be tectonic subsidence at this releasing bend in the fault.

5.4.2 Errors in time-series and strain estimation

There are multiple error sources in InSAR measurements, including, orbital error, digital elevation model error, delay from ionosphere and troposphere, and phase error due to the radar and/or SAR processor. Since Sentinel-1 satellites have excellent baseline control and a very precise orbit (< 2 cm radian, < 5 cm along-track), the orbital error can be considered as minimal [Fernández et al. 2015]. Indeed the geometric alignment method developed in Chapter 4 demonstrates a rms along-track error or 4.1 cm. DEM error is small because the perpendicular baselines are generally less than 100 m. We believe the main error sources are related to the ionosphere and troposphere. The ionospheric error should have amplitudes of amout 1 cm over length scales greater than about 160 km [Fattahi, Simons, and Agram 2017]. Thus the main remaining error source is due to the troposphere. Some of this is removed during the common-scene stacking technique but some remains and this is perhaps the major remaining error source. Following [Emardson, Simons, and Webb 2003], the estimated velocity uncertainty σ_v

due to tropopsheric error can be written as

$$\sigma_v = \frac{\sigma_{ifg}}{t_r} \sqrt{\frac{12}{N^3 - N}} \tag{5.3}$$

where σ_{ifg} is the standard deviation (in millimeters) of atmospheric noise in interferograms and, for California, can be further expanded as $\sigma_{ifg} = 2.5 \times \sqrt{L_{ift}}$ where L_{ifg} is the length scale of the interferogram in kilometers, t_r is the time interval between InSAR scenes and N is the total number of interferograms. Based on this formula, the current uncertainty in the velocity measurement is 3-4 mm/yr, which matches the uncertainty estimates of the LOS velocity map (Figure 5.7). This model predicts it will take roughly another 3 years to beat the atmospheric noise to 1 mm/yr in the velocity estimate. This 1 mm/yr error over a 10 km distance corresponds to a strain rate error of 100 nanostrain. Since most large earthquakes occur in areas where strain rate exceeds this 100 mm/yr threshold [Elliott et al. 2008] we estimate it will take 6 full years of Sentinel-1 acquisitions before it will be useful for hazard analysis.

5.5   Conclusions

As discussed in Chapter 4, the Sentinel-1 InSAR satellites have sufficient orbital accuracy and regular 12 and 24-day cadence to use for InSAR time series analysis. The high accuracy of the Sentinel-1 radar and orbits enables one to sum 42 interferograms around a closed loop and achieve near zero residual phase once the 2Npi ambiguity is removed. Here we have developed a method to uniquely solve for the 2Npi ambiguity in every interferogram so that the phase of the first SAR image in a stack can be absolutely connected to the phase of the last SAR image. Moreover, continuation of time-series

construction can be easily achieved since we are using pure geometric alignment for Sentinel-1 TOPS data. This moves InSAR from a largely relative measurement system to an absolute measurement system within each InSAR frame which are now 250 km by 420 km. The remaining error sources are due to atmospheric phase delays so GPS data are needed to constrain the errors at longer wavelengths. To determine the appropriate crossover wavelength for merging the InSAR and GPS data we analyzed 17 current GPS strain rate models and found that they have good agreement at 80 km wavelengths and longer. We revised a merging approach to use both the horizontal and vertical GPS velocities to correct the long-wavelength error in InSAR time series. Velocities constructed from this InSAR time series show broad-scale tectonic signals that are mainly well resolved by the horizontal GPS measurements. In addition, the LOS velocity map is dominated by a large area of subsidence in the Central Valley of California having maximum subsidence rates of 30 cm/yr. The maps also show numerous hydrologic signals, which we relate to human activities. The current atmospheric noise in the InSAR measurement is 3-4 mm/yr we estimate another three years of Sentinel-1 data will be needed to reduce the noise to 1 mm/yr where it will be valuable for earthquake hazard analysis. Since the Sentinel-1 series is planned to last at least 20 years, it will become and increasingly valuable tool for monitoring interseismic deformation.

Acknowledgements

Chapter 5, in full, is currently being prepared for publication as Xu, X. Sandwell, D.T., "Line-of-Sight Deformation along the San Andreas Fault revealed by Sentinel-1 InSAR". The dissertation author was the primary investigator and author of the paper.

References

Chen, C. W. and Zebker, H. A. (2001). "Two-dimensional phase unwrapping with use of statistical models for cost functions in nonlinear optimization". In: *JOSA A* 18.2, pp. 338–351.

Doin, M.-P., Lasserre, C., Peltzer, G., Cavalié, O., and Doubre, C. (2009). "Corrections of stratified tropospheric delays in SAR interferometry: Validation with global atmospheric models". In: *Journal of Applied Geophysics* 69.1, pp. 35–50.

Elliott, J., Walters, R., and Wright, T. (2016). "The role of space-based observation in understanding and responding to active tectonics and earthquakes". In: *Nature communications* 7, p. 13844.

Elliott, J., Biggs, J, Parsons, B, and Wright, T. (2008). "InSAR slip rate determination on the Altyn Tagh Fault, northern Tibet, in the presence of topographically correlated atmospheric delays". In: *Geophysical Research Letters* 35.12.

Emardson, T., Simons, M, and Webb, F. (2003). "Neutral atmospheric delay in interferometric synthetic aperture radar applications: Statistical description and mitigation". In: *Journal of Geophysical Research: Solid Earth* 108.B5.

Evans, E. (2017). "Strategies for building community-based geodetic models of fault slip rates". In: *SCEC Annu. Meeting*.

Fattahi, H., Simons, M., and Agram, P. (2017). "InSAR Time-Series Estimation of the Ionospheric Phase Delay: An Extension of the Split Range-Spectrum Technique". In: *IEEE Transactions on Geoscience and Remote Sensing* 55.10, pp. 5984–5996.

Fernández, J., Escobar, D., Peter, H., and Féménias, P. (2015). "COPERNICUS POD SERVICE OPERATIONS–ORBITAL ACCURACY OF SENTINEL-1A AND SENTINEL-2A". In: *Proc. Int. Symp. Space Flight Dyn*.

Fialko, Y. (2006). "Interseismic strain accumulation and the earthquake potential on the southern San Andreas fault system". In: *Nature* 441.7096, p. 968.

Field, E. H., Arrowsmith, R, Biasi, G. P., Bird, P., Dawson, T. E., Felzer, K. R., Jackson, D. D., Johnson, K. M., Jordan, T. H., Madugo, C., Michael, A. J., Milner, K. R., Page, M. T., Parsons, T, Powers, P, Shaw, B. E., Thatcher, W. R., Weldon, R. J., and Zeng, Y (2013). "Overview of the Uniform California Earthquake Rupture Forecast Version 3 (UCERF3) Time-Independent Model". In: *AGU Fall Meeting Abstracts*.

Field, E. H., Arrowsmith, R. J., Biasi, G. P., Bird, P., Dawson, T. E., Felzer, K. R., Jackson, D. D., Johnson, K. M., Jordan, T. H., Madden, C., Michael, A. J., Milner, K. R., Page, M. T., Parsons, T., Powers, P. M., Shaw, B. E., Thatcher, W. R., Weldon, R. J., and Zeng, Y. (2014). "Uniform California earthquake rupture forecast, version 3 (UCERF3) - The time-independent model". In: *Bulletin of the Seismological Society of America* 104.3, pp. 1122–1180.

Field, E. H., Jordan, T. H., Jones, L. M., Michael, A. J., and Blanpied, M. L. (2016). "The potential uses of operational earthquake forecasting". In: *Seismological Research Letters* 87.2A, pp. 313–322.

Fielding, E. J., Blom, R. G., and Goldstein, R. M. (1998). "Rapid subsidence over oil fields measured by SAR interferometry". In: *Geophysical Research Letters* 25.17, pp. 3215–3218.

Flesch, L. M., Holt, W. E., Haines, A. J., and Shen-Tu, B. (2000). "Dynamics of the Pacific-North American plate boundary in the western United States". In: *Science* 287.5454, pp. 834–836.

Gourmelen, N., Amelung, F., and Lanari, R. (2010). "Interferometric synthetic aperture radar–GPS integration: Interseismic strain accumulation across the Hunter Mountain fault in the eastern California shear zone". In: *Journal of Geophysical Research: Solid Earth* 115.B9.

Hackl, M, Malservisi, R, and Wdowinski, S (2009). "Strain rate patterns from dense GPS networks". In: *Natural Hazards and Earth System Sciences* 9.4, pp. 1177–1187.

Haines, A. and Holt, W. (1993). "A procedure for obtaining the complete horizontal motions within zones of distributed deformation from the inversion of strain rate data". In: *Journal of Geophysical Research: Solid Earth* 98.B7, pp. 12057–12082.

Hammond, W. C., Blewitt, G., and Kreemer, C. (2016). "GPS Imaging of vertical land motion in California and Nevada: Implications for Sierra Nevada uplift". In: *Journal of Geophysical Research: Solid Earth* 121.10, pp. 7681–7703.

Hooper, A. and Spaans, K (2016). "Sentinel-1 burst overlap InSAR: north-south sensitivity at last?" In: *AGU Fall Meeting Abstracts*.

Johanson, I. and Bürgmann, R (2005). "Creep and quakes on the northern transition zone of the San Andreas fault from GPS and InSAR data". In: *Geophysical Research Letters* 32.14.

Kreemer, C., Blewitt, G., and Klein, E. C. (2014). "A geodetic plate motion and global strain rate model". In: *Geochemistry, Geophysics, Geosystems* 15.10, pp. 3849–3889.

Loveless, J. P. and Meade, B. J. (2011). "Stress modulation on the San Andreas fault by interseismic fault system interactions". In: *Geology* 39.11, pp. 1035–1038.

Lyons, S. and Sandwell, D. (2003). "Fault creep along the southern San Andreas from interferometric synthetic aperture radar, permanent scatterers, and stacking". In: *Journal of Geophysical Research: Solid Earth* 108.B1.

McCaffrey, R. (2005). "Block kinematics of the Pacific–North America plate boundary in the southwestern United States from inversion of GPS, seismological, and geologic data". In: *Journal of Geophysical Research: Solid Earth* 110.B7.

Parsons, T. (2006). "Tectonic stressing in California modeled from GPS observations". In: *Journal of Geophysical Research: Solid Earth* 111.B3.

Parsons, T., Johnson, K. M., Bird, P., Bormann, J., Dawson, T. E., Field, E. H., Hammond, W. C., Herring, T. A., McCaffrey, R., Shen, Z.-k., Thatcher, W. R., Weldon, I., Ray, J, and Zeng, Y. (2013). "Appendix C - Deformation models for UCERF3". In:

Peltzer, G., Crampé, F., Hensley, S., and Rosen, P. (2001). "Transient strain accumulation and fault interaction in the Eastern California shear zone". In: *Geology* 29.11, pp. 975–978.

Petersen, M. D., Mueller, C. S., Frankel, A. D., and Zeng, Y. (2008). *Spatial seismicity rates and maximum magnitudes for background earthquakes*. Tech. rep. Geological Survey (US).

Petersen, M. D., Zeng, Y., Haller, K. M., McCaffrey, R., Hammond, W. C., Bird, P., Moschetti, M., Shen, Z.-k., Bormann, J., and Thatcher, W. R. (2014). "Geodesy- and geology-based slip-rate models for the western United States (excluding California) national seismic hazard maps". In:

Platt, J. P. and Becker, T. W. (2010). "Where is the real transform boundary in California?" In: *Geochemistry, Geophysics, Geosystems* 11.6.

Rosen, P. A., Hensley, S., and Chen, C. (2010). "Measurement and mitigation of the ionosphere in L-band interferometric SAR data". In: *Radar Conference, 2010 IEEE*. IEEE, pp. 1459–1463.

Ryder, I. and Bürgmann, R. (2008). "Spatial variations in slip deficit on the central San Andreas fault from InSAR". In: *Geophysical Journal International* 175.3, pp. 837–852.

Sandwell, D. T. and Wessel, P. (2016). "Interpolation of 2-D vector data using constraints from elasticity". In: *Geophysical Research Letters* 43.20.

Sandwell, D. T., Zeng, Y., Shen, Z.-K., Crowell, B., Murray, J., McCaffrey, R., and Xu, X. (2016). "The SCEC Community Geodetic Model V1: Horizontal Velocity Grid". In: *SCEC Annu. Meeting*.

Shen, Z.-K., Wang, M., Zeng, Y., and Wang, F. (2015). "Optimal interpolation of spatially discretized geodetic data". In: *Bulletin of the Seismological Society of America*.

Shirzaei, M, Bürgmann, R, Foster, J, Walter, T., and Brooks, B. (2013). "Aseismic deformation across the Hilina fault system, Hawaii, revealed by wavelet analysis of InSAR and GPS time series". In: *Earth and Planetary Science Letters* 376, pp. 12–19.

Shirzaei, M. and Bürgmann, R. (2013). "Time-dependent model of creep on the Hayward fault from joint inversion of 18 years of InSAR and surface creep data". In: *Journal of Geophysical Research: Solid Earth* 118.4, pp. 1733–1746.

Smith, W. and Wessel, P (1990). "Gridding with continuous curvature splines in tension". In: *Geophysics* 55.3, pp. 293–305.

Smith-Konter, B. and Sandwell, D. (2009). "Stress evolution of the San Andreas fault system: Recurrence interval versus locking depth". In: *Geophysical Research Letters* 36.13.

Tape, C., Musé, P., Simons, M., Dong, D., and Webb, F. (2009). "Multiscale estimation of GPS velocity fields". In: *Geophysical Journal International* 179.2, pp. 945–971.

Tong, X, Sandwell, D., and Smith-Konter, B (2013). "High-resolution interseismic velocity data along the San Andreas fault from GPS and InSAR". In: *Journal of Geophysical Research: Solid Earth* 118.1, pp. 369–389.

Tong, X. and Schmidt, D. (2016). "Active movement of the Cascade landslide complex in Washington from a coherence-based InSAR time series method". In: *Remote Sensing of Environment* 186, pp. 405–415.

Tymofyeyeva, E. and Fialko, Y. (2015). "Mitigation of atmospheric phase delays in InSAR data, with application to the eastern California shear zone". In: *Journal of Geophysical Research: Solid Earth* 120.8, pp. 5952–5963.

Wei, M., Sandwell, D., and Smith-Konter, B. (2010). "Optimal combination of InSAR and GPS for measuring interseismic crustal deformation". In: *Advances in Space Research* 46.2, pp. 236–249.

Welch, P. (1967). "The use of fast Fourier transform for the estimation of power spectra: a method based on time averaging over short, modified periodograms". In: *IEEE Transactions on audio and electroacoustics* 15.2, pp. 70–73.

Wessel, P., Smith, W. H., Scharroo, R., Luis, J., and Wobbe, F. (2013). "Generic mapping tools: improved version released". In: *Eos, Transactions American Geophysical Union* 94.45, pp. 409–410.

Williams, S., Bock, Y., and Fang, P. (1998). "Integrated satellite interferometry: Tropospheric noise, GPS estimates and implications for interferometric synthetic aperture radar products". In: *Journal of Geophysical Research: Solid Earth* 103.B11, pp. 27051–27067.

Xu, X., Sandwell, D. T., Tymofyeyeva, E., González-Ortega, A., and Tong, X. (2017). "Tectonic and Anthropogenic Deformation at the Cerro Prieto Geothermal Step-Over Revealed by Sentinel-1A InSAR". In: *IEEE Transactions on Geoscience and Remote Sensing*.

Zeng, Y. and Shen, Z.-K. (2014). "Fault network modeling of crustal deformation in California constrained using GPS and geologic observations". In: *Tectonophysics* 612, pp. 1–17.

Tables and Figures

Table 5.1: **Information of Sentinel-1 data from descending tracks**.

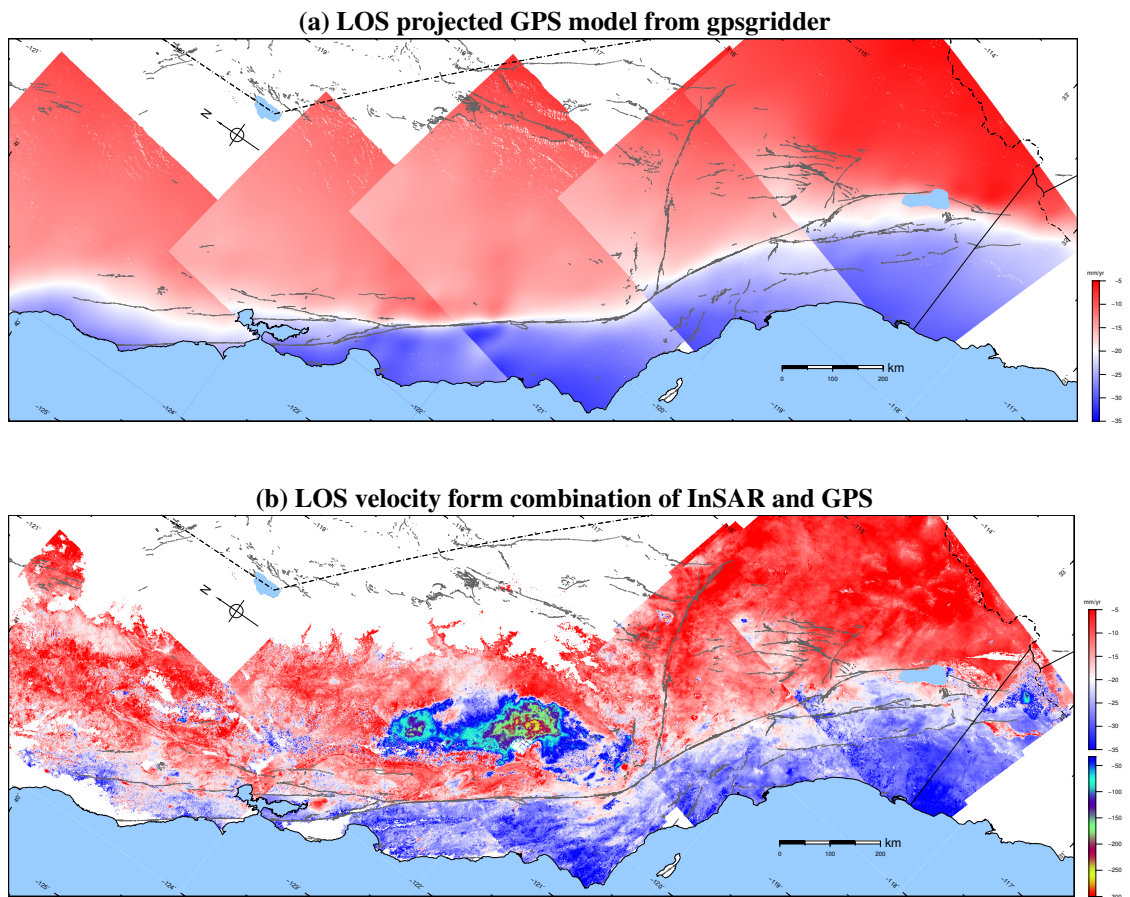| Track	Azimuth Anx Time Span (s)	Number of Scenes	Number of Interfero-grams	Total time span (days)
173	2383 - 2438	38	126	6914
071	2376 - 2431	37	140	8343
144	2349 - 2399	62	335	15684
042	2329 - 2384	44	211	12584
115	2288 - 2344	48	254	15072
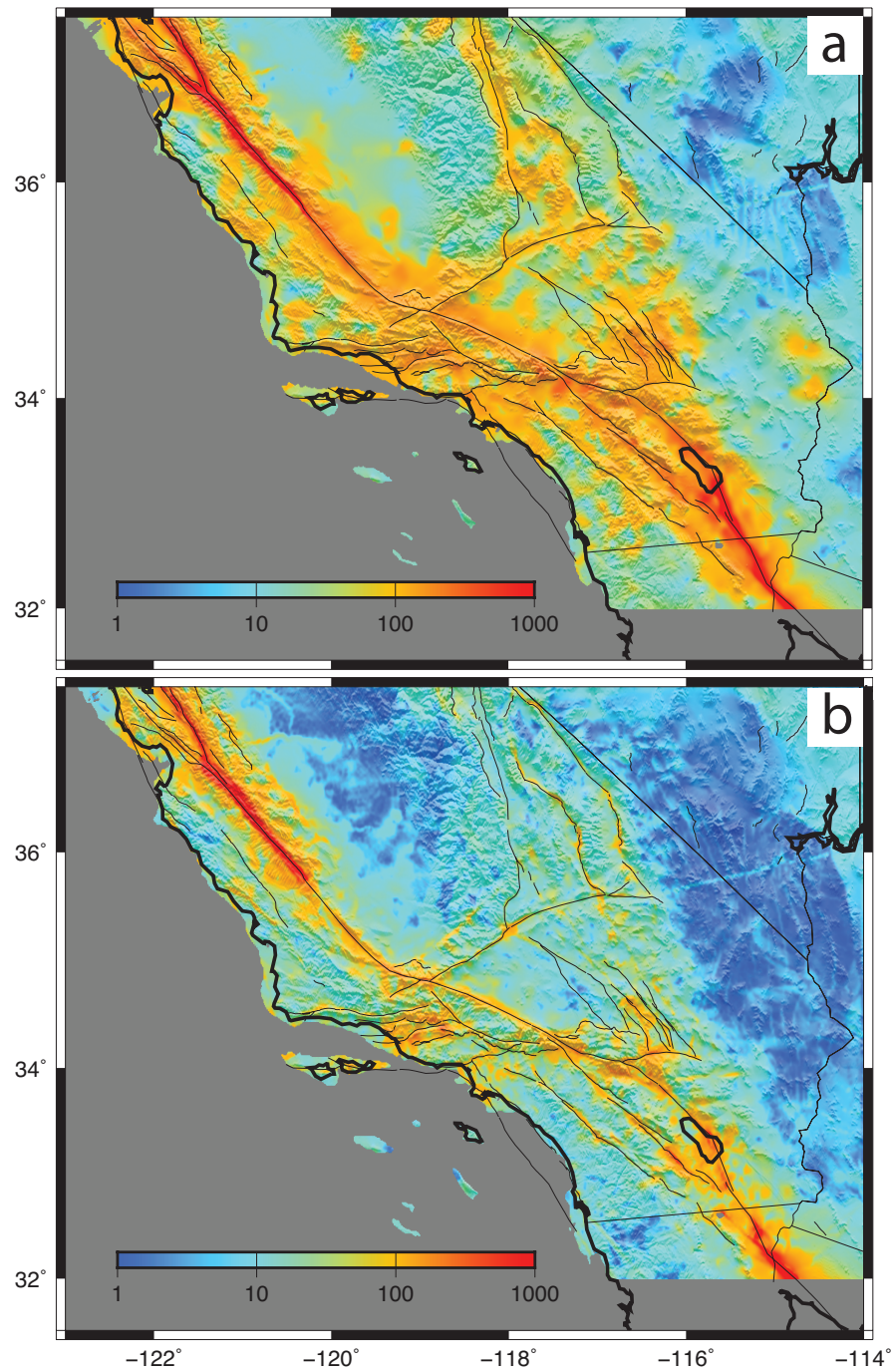
Figure 5.1: **Community Geodetic Model Version 1.0**. (a) is the GPS strain model from averaging 10 GPS strain models, with color denoting the second invariant of strain rate in log scale. (b) is the standard deviation of (a). The black lines are the fault traces and state or wet region boundaries.
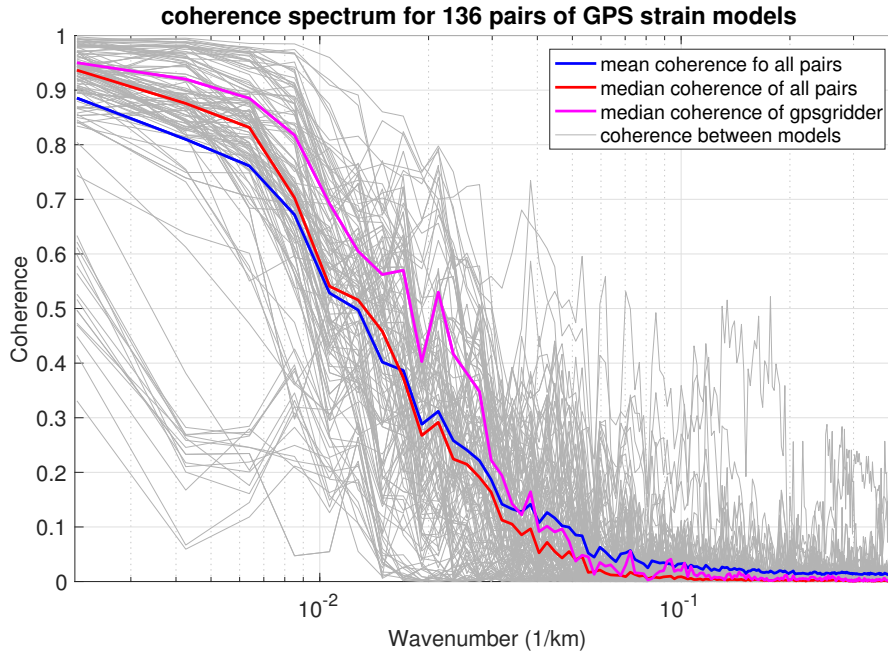
Figure 5.2: **Coherence spectrum between GPS strain models**. The blue line is the mean of the coherence spectrums and the red line is the median. Magenta line represent the median coherence spectrum between gpsgridder and all other models.
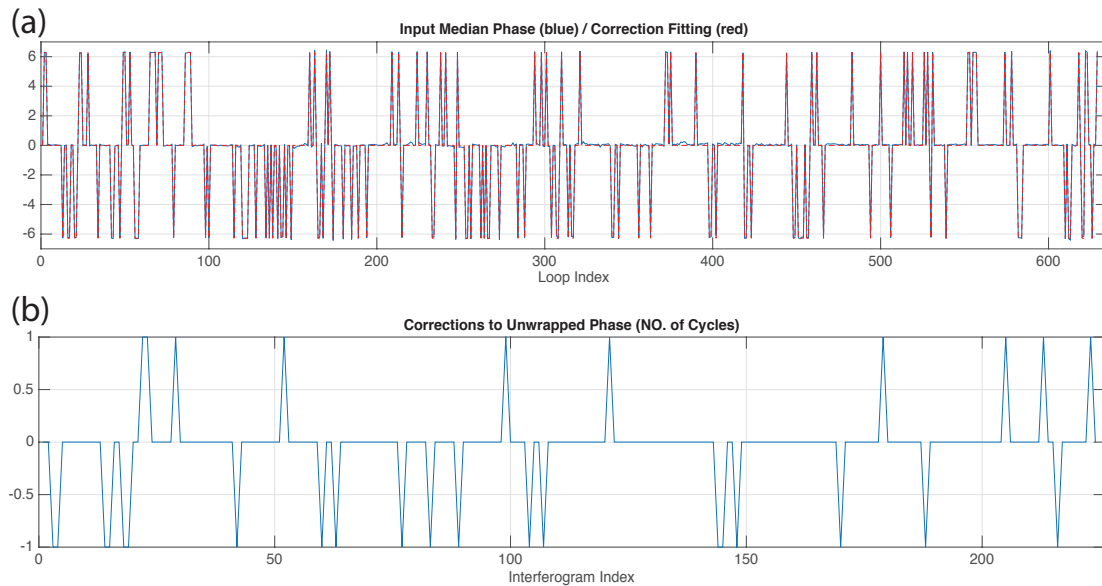
Figure 5.3: **Phase unwrapping ambiguity correction with a sparse recovery method**. (a) is the representing the data (loop) space and (b) is representing the model (correction) space. Blue lines in (a) is the data acquired by summing interferograms in each loop and taking the median (then divided by 2π). Red dashed lines in (a) is the model (correction) prediction. (b) is the correction (should be multiplied by 2π) that should be subtracted from each interferogram.

(a) LOS projected GPS model from gpsgridder

(b) LOS velocity form combination of InSAR and GPS

Figure 5.4: **GPS model and LOS deformation from combining Sentinel-1 InSAR and GPS data**. (a) is the GPS velocity model from applying gpsgridder to 1977 GPS velocity vectors (converted to ITRF). The model is projected to LOS of 5 Sentinle-1 satellite descending tracks, with the flight direction being north-east to south-west and satellite looking toward its right. (b) is the combined LOS velocity. Pixels that has more than 25% unwrapping errors is abandoned. In both maps, the grey lines are the fault traces.
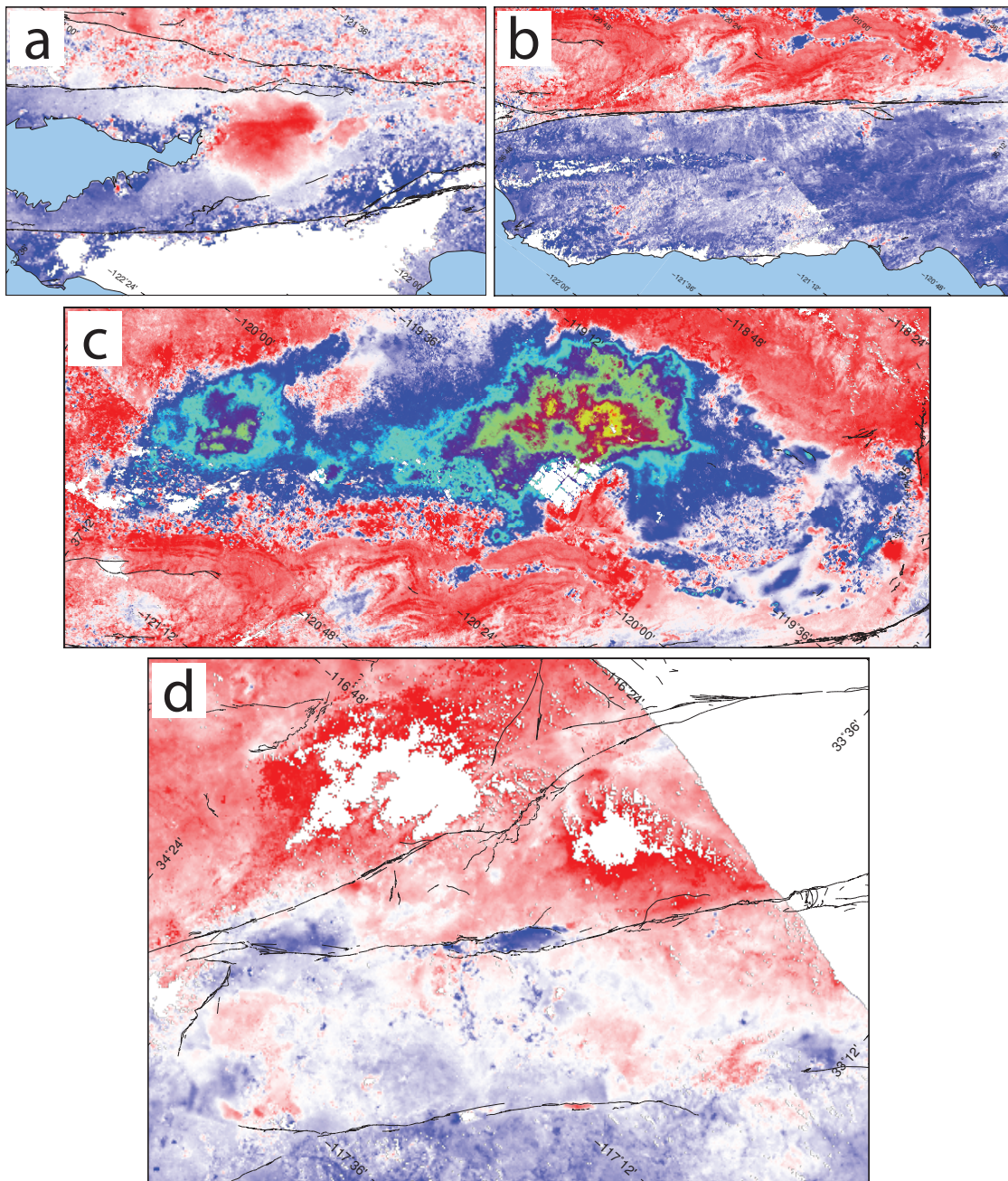
Figure 5.5: **Zoom-ins on some of the discoveries from InSAR and GPS combined velocity map**. a is the around the Bay Area, to the south of which is the Santa Clara valley uplift and to the east is the Hayward fault creep. b is the creeping section of the San Andreas fault. c is the revealed subsidence in central valley. d is the LOS deformation across Elsinore, San Jocinto and San Andreas faults, together with the subsidence at the San Jocinto fault step-over.
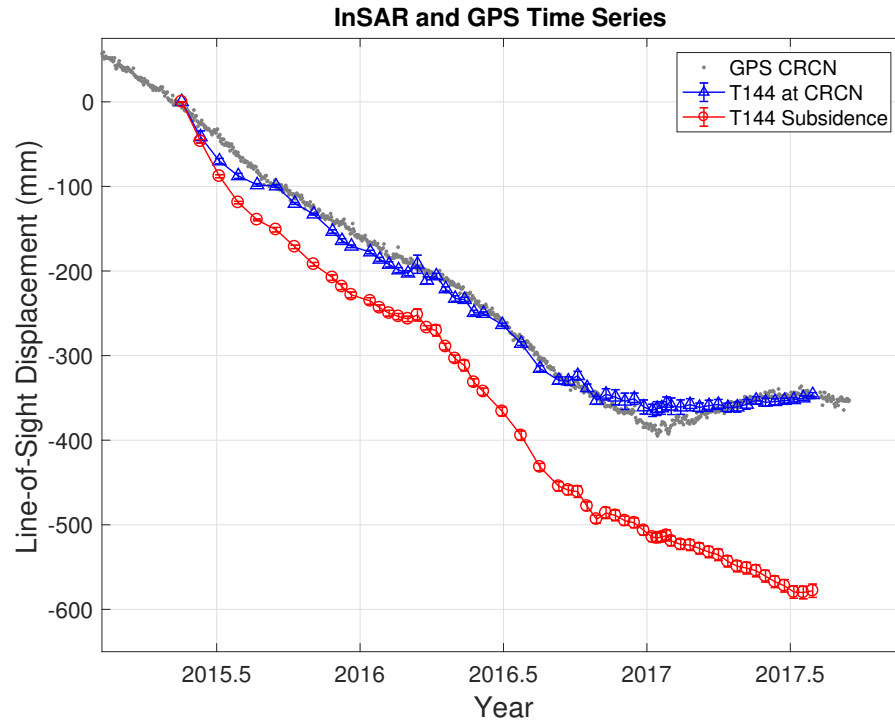
Figure 5.6: **Time Series of InSAR and GPS data**. The grey dots are the processed and filtered GPS data at CRCN with the blue triangles denoting the solution from InSAR and GPS combination. Red circles are the time-series at maximum subsidence in central valley.
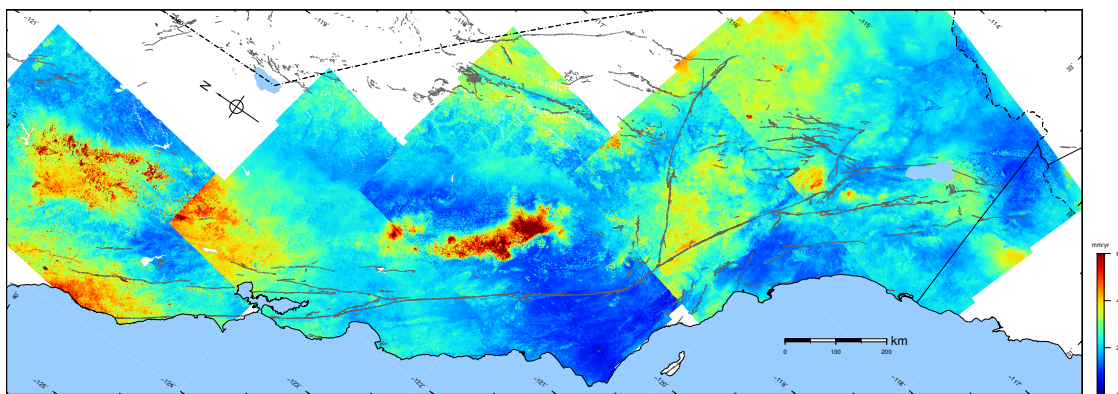
Figure 5.7: **Uncertainty from LOS velocity estimates**. The plot represents the uncertainty from linear regression of the time-series. The colors denotes uncertainty level, which is a composition of seasonal signals, atmospheric noise and other effects.